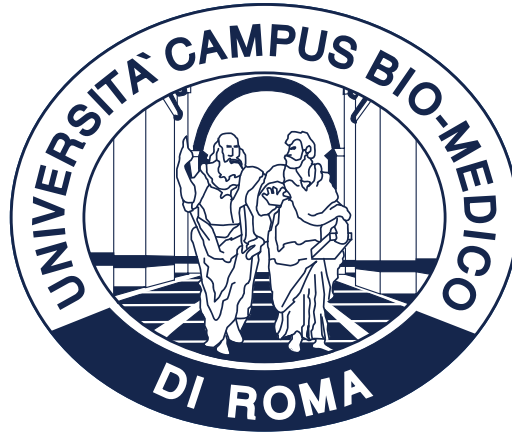


Tesi di dottorato in Bioingegneria e bioscienze, di Jacopo Tosi,
discussa presso l'Università Campus Bio-Medico di Roma in data 28/05/2019.
La disseminazione e la riproduzione di questo documento sono consentite per scopi di didattica e ricerca,
a condizione che ne venga citata la fonte.



UNIVERSITÀ CAMPUS BIO-MEDICO DI ROMA

FACOLTÀ DI INGEGNERIA

**CORSO DI DOTTORATO DI RICERCA IN BIOINGEGNERIA E BIOSCIENZE
XXXI CICLO**

PhD Thesis

**Motion sensor network based on low power wireless
technologies for the assessment of neurological diseases**

Supervisor

Domenico Formica, PhD

Co-Supervisor

Fabrizio Taffoni, PhD

PhD Candidate

Jacopo Tosi

Industrial Tutor

Roberto Sannino

May 2019

Tesi di dottorato in Bioingegneria e bioscienze, di Jacopo Tosi,
discussa presso l'Università Campus Bio-Medico di Roma in data 28/05/2019.
La disseminazione e la riproduzione di questo documento sono consentite per scopi di didattica e ricerca,
a condizione che ne venga citata la fonte.

Abstract

In the last years, the spread in the market of miniaturized magneto-inertial sensors, that are so small, low cost and power efficient to be attachable to any system (human body included), has expanded their potential in a myriad of applications. Since their introduction on the market, bioengineers have exploited their potential for the motion analysis in healthy subjects, but also in patients for the assessment of pathologies characterized by motor dysfunctions, such as neurological diseases.

One of the main challenges related to the use of those sensors in biomedical applications, is to develop a user friendly, low power, low cost and high throughput M-IMU systems which allows to monitor patients with motor impairments and acquire reliable data to support clinical decisions. In fact, despite the large number of commercial devices based on magneto-inertial sensors available on the market, their use for clinical assessment in unstructured environments (*e.g.* at-home) is still limited. On one side most of the portable systems coming from the consumer electronics market (smartbands or smartwatches) allow for pervasive, low-power communication with smart devices (thus usable at home), but do not permit a high throughput streaming and/or provide limited information coming from one single node. On the other side, most of the M-IMU systems used in biomedical or clinical research provide high throughput and multi-node information, but are quite expensive, usable only by trained staff, and often have limited battery life capabilities (since are not based on low energy wireless communication) or use non-standard and widespread communication technology, making them suitable only for use in structured or semi-structured environments (*i.e.* research laboratories, research hospitals).

To overcome these limitations, the overall aim of this PhD project is to design, test and validate a M-IMU based wireless sensor network, for motor assessment of neurological patients in unstructured environments.

To do this, our first goal is to select and test a suitable wireless technology, with reduced power consumption and wide compatibility with consumer electronics for out-of-the-lab and at-home applications. We found Bluetooth Low Energy (BLE) to be an excellent candidate for our requirements and we performed for the first time an extensive and systematic analysis of BLE, in order to demonstrate whether it is a suitable candidate for wireless

communication in high throughput and low energy sensor network applications. Defining a standard methodology to test wireless sensor networks, we tested BLE performance in a sensor network with a star topology, showing the possibility to use this communication technology in high data rate applications (~170 kbps), thus enabling the streaming of 5 nodes with 9-axes M-IMU data (16 bits of resolution per axis) at more than 200 Hz.

The second goal of our work is to assess the reliability of M-IMU sensors for motion analysis. In fact, despite their pervasive use in biomedical applications, the assessment of their accuracy and reliability for motion tracking has been only partially addressed. Our main contribution in this field is focused on the design of a standard methodology to tune and optimize filter parameters in M-IMU sensor fusion algorithms, able to measure the error with respect of a ground truth (represented by the optical motion tracking system), in order to evaluate the goodness of these filters. The results show how filters' performance may be different, depending on the application, and we propose a standard protocol to identify the filter's algorithm and the specific gain values which guarantee the best performance for the specific task, obtaining an orientation error of about 2° and lower than 5° , respectively in static and dynamic conditions.

Finally, our third goal is to use a reliable technology in terms of both wireless communication and sensor technology, to objectively assess motor conditions of patients with neurological deficits. Among several possible pathologies with relevant movement disorders, we focus on Parkinson's disease. In fact, PD may highly benefit from the use of magneto-inertial sensors for the diagnosis and assessment of its motor symptoms. As a matter of fact, motor symptoms in PD are not only highly relevant, but they are also very representative of the evolution of the pathology. For this reason they are strictly related to diagnosis, assessment and monitoring; indeed, a very important part of the widely used PD assessment clinical scale (*i.e.* the UPDRS scale), administered by the physician, is focused on the evaluation of motor disorders. The clinical analysis, which is occasionally administered by the doctor, presents some limits: PD has fluctuations during different days, but also in the same day, which do not guarantee the efficacy of the medical assessment in the hospital. Hence, we decide to continuously monitor PD patients using M-IMUs: in detail, we use these typology of sensors to evaluate PD's cardinal motor symptoms in different tasks of its clinical scale.

As result, our main contribution in this topic is to exploit a M-IMU sensor network to discriminate fluctuations in subjects with Parkinson's disease (*i.e.* ON and OFF status), and to detect statistically significant differences between PD and healthy subjects with a few number of sensor and performing easy tasks. After a deep analysis of some of the UPDRS tasks administered by the physician to the patients, we evidenced statistically significant results to

assess PD. The first analysis regards patients during the execution of arm prono-supination task and evaluating the total power as kinematic feature on only one sensor positioned on the index, thumb or wrist. These sensor locations and kinematic index can detect statistically significant differences between ON and OFF state (index: $p = 0.003$; thumb: $p = 0.001$; wrist: $p = 0.005$), and also between PD and healthy subjects (index, thumb, wrist: $p < 0.0001$). Moreover, we also found that using one M-IMU only on the trunk while performing a sit to stand task and evaluating trunk acceleration during trunk flexion it is possible to differentiate OFF and ON with respect to healthy subject ($p < 0.05$).

Tesi di dottorato in Bioingegneria e bioscienze, di Jacopo Tosi,
discussa presso l'Università Campus Bio-Medico di Roma in data 28/05/2019.
La disseminazione e la riproduzione di questo documento sono consentite per scopi di didattica e ricerca,
a condizione che ne venga citata la fonte.

List of Publications

- [J.I] **Jacopo Tosi**, Fabrizio Taffoni, Marco Santacatterina, Roberto Sannino, and Domenico Formica. Performance evaluation of Bluetooth Low Energy: A systematic review. *Sensors (Switzerland)*, 17(12):2898, 12 2017.
- [J.II] Lazzaro di Biase, Susanna Summa, **Jacopo Tosi**, Fabrizio Taffoni, Massimo Marano, Angelo Cascio Rizzo, Fabrizio Vecchio, Domenico Formica, Vincenzo Di Lazzaro, Giovanni Di Pino, and Mario Tombini. Quantitative analysis of bradykinesia and rigidity in Parkinson's disease. *Frontiers in Neurology*, 9(MAR):121, 3 2018.
- [J.III] **Jacopo Tosi**, Fabrizio Taffoni, Marco Santacatterina, Roberto Sannino, and Domenico Formica. Throughput Analysis of BLE Sensor Network for Motion Tracking of Human Movements. *IEEE Sensors Journal*, 19(1):370–377, 2019.
- [C.I] Susanna Summa, **Jacopo Tosi**, Fabrizio Taffoni, Lazzaro Di Biase, Massimo Marano, Angelo Cascio Rizzo, Mario Tombini, Giovanni Di Pino, and Domenico Formica. Assessing bradykinesia in Parkinson's disease using gyroscope signals. In *2017 International Conference on Rehabilitation Robotics (ICORR)*, pages 1556–1561, London, 7 2017. IEEE.
- [C.II] **Jacopo Tosi**, Susanna Summa, Fabrizio Taffoni, Lazzaro di Biase, Massimo Marano, Angelo Cascio Rizzo, Mario Tombini, Emiliano Schena, Domenico Formica and Giovanni Di Pino. Feature Extraction in Sit-to-Stand Task Using M-IMU Sensors and Evaluation in Parkinson's Disease. In *2018 IEEE International Symposium on Medical Measurements and Applications (MeMeA)*, pages 1–6. IEEE, 6 2018.
- [C.III] Micaela Del Fabbro Arcopinto, **Jacopo Tosi**, Domenico Formica, and Fabrizio Taffoni. Monitoring Sucking Abilities in Newborns: Design and Validation on Adult Of a Wearable System for Non-Invasive Deglutition Detection. In *2018 40th Annual International Conference of the IEEE Engineering in Medicine and Biology Society (EMBC)*, pages 4257–4260. IEEE, 7 2018.
- [C.IV] **Jacopo Tosi**, Fabrizio Taffoni, Asif Hussain, Domenico Campolo and Domenico Formica. Methodology for the Evaluation of Magneto-Inertial Orientation Filters in SO(3). In *2019 IEEE International Workshop on Metrology for Industry 4.0 and IoT*, in press. IEEE, 6 2019.
- [C.V] Assia Chericoni, **Jacopo Tosi**, Anna Maria Visco, Riccardo Lubrano, Fabrizio Taffoni. Assessment of feeding teats: an experimental study. In *2019 41th Annual International Conference of the IEEE Engineering in Medicine and Biology Society (EMBC)*, in press. IEEE, 7 2019.

Tesi di dottorato in Bioingegneria e bioscienze, di Jacopo Tosi,
discussa presso l'Università Campus Bio-Medico di Roma in data 28/05/2019.
La disseminazione e la riproduzione di questo documento sono consentite per scopi di didattica e ricerca,
a condizione che ne venga citata la fonte.

Table of contents

List of Publications	vii
List of figures	xi
List of tables	xiii
Nomenclature	xv
1 Introduction	1
1.1 Research challenges	1
1.2 Research goals	2
1.3 Contributions	4
1.4 Outline of the thesis	5
2 Motion sensor network with low energy wireless communication	7
2.1 Bluetooth Low Energy: definitions, main features and characteristics	9
2.1.1 BLE Communication	10
2.1.2 BLE Packet	13
2.1.3 BLE Network Topology	13
2.2 BLE performance analysis in a sensor network for M-IMU applications	14
2.2.1 Assessment of throughput and number of nodes	16
2.2.2 Evaluation of power consumption	30
3 Performance evaluation of magneto-inertial motion units and sensor fusion algorithms	35
3.1 Background on Magneto-Inertial Measurement Units: basic features and functioning	36
3.1.1 Gyroscope	37
3.1.2 Accelerometer	38

3.1.3	Magnetometer	40
3.1.4	Accelerometer and magnetometer calibration	41
3.2	Validation of sensor fusion algorithms for attitude estimation with M-IMUs	43
3.2.1	Sensor fusion filters: state of the art	44
3.2.2	Two-frame sensor calibration	55
3.2.3	Generation of synthetic M-IMU data	59
3.2.4	Filter tuning and performance evaluation of M-IMUs' sensor fusion algorithms	61
4	Use of M-IMUs for the assessment in neurological diseases	81
4.1	Parkinson's Disease: basic concepts	82
4.2	Assessment of Parkinson's disease by means of a wearable M-IMU network	84
4.2.1	Upper limb monitoring for quantitative analysis of bradykinesia and rigidity in Parkinson's disease	85
4.2.2	Feature extraction in Sit-to-Stand task using M-IMUs for the assessment of Parkinson's disease	105
5	Discussion and conclusions	117
5.1	Future works	119
	Appendix A Representation of orientation	121
A.1	Rotation Matrix	121
A.2	Euler Angles	122
A.3	Axis and angles	123
A.4	Quaternions	124
A.5	Metric on SO(3) space	125
	Appendix B Coordinate frames	127
	References	131

List of figures

2.1	BLEStack	10
2.2	SmartReady	11
2.3	connectionParam	12
2.4	BLEPacket	13
2.5	ConnPacket	14
2.6	BLETopology	15
2.7	Throughput Devices	17
2.8	MIMUPacket	19
2.9	Percentage 1 Node	21
2.10	Throughput 1 Node	22
2.11	Percentage 5 Nodes	23
2.12	Throughput 5 Nodes	24
2.13	Maximum bitrate	27
2.14	Current consumption	32
3.1	Hard Iron calibration	42
3.2	Complementary Filter	48
3.3	Complementary Filter in M-IMU	48
3.4	Mahony Filter	49
3.5	Mahony Direct Filter	50
3.6	Mahony Direct Filter	51
3.7	Campolo SO(3) Filter	52
3.8	Madgwick Filter	53
3.9	Tian Filter	54
3.10	Two-frame sensor calibration	56
3.11	Example of two-frame sensor calibration	57
3.12	Reference frame for M-IMU data generation	60
3.13	SensorTile	62

3.14	Motion tracker VZ4000v	64
3.15	Motion tracker VZ4000v	65
3.16	Assembly of SensorTile and LED targets	66
3.17	Assembly of SensorTile and LED targets, Top View	67
3.18	Trajectory	68
3.19	Tuning Synthetic Data	70
3.20	Synthetic data angle error	72
3.21	Trajectory of Two-frame Sensor Problem Calibration	73
3.22	Tuning Real Data for Two-Frame Calibration	74
3.23	Trajectory of Performance Evaluation	75
3.24	Tuning Real Data for performance evaluation	76
3.25	Real data angle error during two-frame calibration	78
3.26	Real data angle error during performance evaluation	79
4.1	Clinical symptoms associated with Parkinson's disease progression	83
4.2	Position of M-IMUs on upper limb	89
4.3	Movement speed profile and SPARC values	91
4.4	Results relative to total time index	95
4.5	Peak-to-peak velocity of all cycles	97
4.6	Fatigability index in finger-tapping task	97
4.7	Fatigability index in the arm prono-supination task	98
4.8	Power Spectral Density of gyroscopes	98
4.9	Total power index in the finger-tapping task	99
4.10	Total power index in the arm prono-supination task	99
4.11	Smoothness parameter evaluated in the index finger	101
4.12	Smoothness index assessed for the sensor on the wrist	102
4.13	Sensor used in the <i>SiSt</i> task	106
4.14	Value of $\sin(\theta)$ of the trunk during <i>SiSt</i> task	108
4.15	Features referred to the value of θ of the trunk during <i>SiSt</i> task	110
4.16	Features referred to the value of ω_y of the trunk during <i>SiSt</i> task	111
4.17	Features referred to the value of a_y of the trunk during <i>SiSt</i> task	112
4.18	Results relative to <i>SiSt</i> task	114
B.1	Coordinate frames involved in the inertial navigation framework	128
B.2	Coordinate frames involved in the system navigation framework	129

List of tables

2.1	Maximum reachable bitrate	26
2.2	Connection parameter for maximum reachable bitrate	26
2.3	SensorTile consumption	33
3.1	VZ4000v Technical Specifications	65
3.2	Filter gains for synthetic data	71
3.3	Filter gains for real data in two-frame calibration problem	77
3.4	Filter gains for real data in performance evaluation	77
3.5	Filter computational time	79
4.1	Parkinson's disease patients characteristics	88
4.2	Bradykinesia tasks clinical rating	93
4.3	Rigidity task clinical rating	94
4.4	Finger-tapping task kinematic results	95
4.5	Prono-supination task kinematic results	96

Tesi di dottorato in Bioingegneria e bioscienze, di Jacopo Tosi,
discussa presso l'Università Campus Bio-Medico di Roma in data 28/05/2019.
La disseminazione e la riproduzione di questo documento sono consentite per scopi di didattica e ricerca,
a condizione che ne venga citata la fonte.

Nomenclature

Acronyms / Abbreviations

AA	Access Address
ACK	Acknowledgment
AHRS	Attitude and Heading Reference Systems
AMR	Anisotropic MagnetoResistance
BAN	Body Area Network
BLE	Bluetooth Low Energy
CF	Complementary Filter
<i>connEvent</i>	Connection Event
<i>connInterval</i>	Connection Interval
<i>connSlaveLatency</i>	Connection Slave Latency
<i>connSupervisionTimeout</i>	Connection Supervision Timeout
CRC	Cycle Redundancy Check
DAC	Digital to Analog Converter
DOF	Degree Of Freedom
DWT	Discrete Wavelet Transform
EKF	Extended Kalman Filter
ENU	East North Up

EOF	End Of Frame
FW	Firmware
GAP	Generic Access Profile
GDA	Gradient Descendent Algorithm
GNA	Gauss-Newton Algorithm
HCI	Host Controller Interface
HS	Healthy Subject
HW	Hardware
ICA	Independent Component Analysis
IC	Integrated Circuit
IMU	Inertial Measurement Units
ISM	Industrial, Scientific and Medical (ISM)
KF	Kalman Filter
LED	Light Emitting Diode
LSB	Least Significant Bit
M-IMU	Magneto-Inertial Measurement Unit
MARG	Magnetic, Angular Rate and Gravity
MCU	MicroController Units
MDS-UPDRS	Movement Disorder Society - Unified Parkinson's Disease Rating Scale
MEMS	Mico-Electro-Mechanical Systems
MIC	Message Integrity Check
nATT	Number of Attempts
PCA	Principal Component Analysis
PD	Parkinson's Disease

PDU	Protocol Data Unit
PL	Packet Loss
PRE	Preamble
PSD	Power Spectral Density
PTI	Phoenix Technologies Inc.
QUEST	QUaternion ESTimator
RF	Radio Frequency
RPY	Roll Pitch Yaw
SAL	Spectral Arch Length
SE	Standard Error
SIG	Bluetooth Special Interest Group
<i>SiSt</i>	Sit-to-Stand
SPARC	Spectral Arch Length
STM	STMicroelectronics
SW	Software
TD	Transition Duration
tPT	Time of Postural Transition
<i>TS</i>	Time Stamp
UPDRS	Unified Parkinson's Disease Rating Scale
WSN	Wireless Sensor Network

Tesi di dottorato in Bioingegneria e bioscienze, di Jacopo Tosi,
discussa presso l'Università Campus Bio-Medico di Roma in data 28/05/2019.
La disseminazione e la riproduzione di questo documento sono consentite per scopi di didattica e ricerca,
a condizione che ne venga citata la fonte.

Chapter 1

Introduction

This chapter provides an introduction to the thesis by briefly explaining the context in which the present work has been carried out, exposing the current challenges and stating the goals of this research. Finally, the main innovative contributions of this work, with respect to the state of the art, are introduced and the organization of the following chapters is outlined.

1.1 Research challenges

In the last years, the spread in the market of miniaturized magneto-inertial sensors, that are so small, low cost and power efficient to be attachable to any system (human body included), has expanded their potential in a myriad of applications. Since their introduction on the market, bioengineers have exploited their potential for the motion analysis in healthy subjects, but also in patients for the assessment of pathologies characterized by motor dysfunctions, such as neurological diseases.

In the last decades, several studies showed that wearable sensors, used for assessing motor symptoms of neurological diseases (*e.g.* Parkinson's disease), could provide a quantitative and reliable tool for patient's motor performance monitoring.

Most of the studies presented in literature exploit commercial M-IMU systems that are usually quite expensive compared to the effective cost of the hardware included in these sensors, and they also use closed library, which does not allow to fully test the reliability of the proprietary sensor fusion algorithms.

One of the main challenges related to the use of those sensors in biomedical applications, is to develop a user friendly, low power, low cost and high throughput M-IMU systems which allows to monitor patients with motor impairments and acquire reliable data to support clinical decisions.

In fact, despite the large number of commercial devices based on magneto-inertial sensors available on the market, their use for clinical assessment in unstructured environments (*e.g.* at-home) is still limited. On one side most of the portable systems coming from the consumer electronics market (smartbands or smartwatches) allow for pervasive, low-power communication with smart devices (thus usable at home), but do not permit a high throughput streaming and/or provide limited information coming from one single node. On the other side, most of the M-IMU systems used in biomedical or clinical research provide high throughput and multi-node information, but are quite expensive and often have limited battery life capabilities (since are not based on low energy wireless communication) or use non-standard and widespread communication technology, making them suitable only for use in structured or semi-structured environments (*i.e.* research laboratories, research hospitals).

To overcome these limitations, the overall aim of this PhD project is to design, test and validate a M-IMU based wireless sensor network, for motor assessment of neurological patients in unstructured environments. To reach this purpose it has been necessary to develop the application from the very first steps: *i.e.* the study and implementation of the right wireless communication technology, able to connect the sensors in our system, and the validation of M-IMU sensor fusion algorithms for kinematic reconstruction. Finally we also assessed both wireless communication and sensor technology for the validation of motor condition of patients with neurological disorders.

1.2 Research goals

The main goal of this work is to design and test a low-cost, low energy and easy-to-use network of magneto-inertial sensors for biomedical applications, in particular for motor assessment of neurological patients, such as Parkinson's disease (PD) patients.

To do this, our first goal is to select and test a suitable wireless technology, with reduced power consumption and wide compatibility with consumer electronics for out-of-the-lab and at-home applications. We found Bluetooth Low Energy (BLE) to be an excellent candidate for our requirements and we performed; nevertheless, it has only been tested in low throughput networks [1] or high throughput applications with only one node, *e.g.* microphones [2]. For all these reasons we need to evaluate BLE performance in order to assess its possible use in high throughput applications with several nodes. In fact, we look for a low power, low cost and secure multinode solution, as already stated in the previous Section, and BLE seems to represent the right solution to our problem, but it has never been assessed in high throughput applications based on networks with several nodes.

The second goal of our work is to assess the reliability of M-IMU sensors for motion analysis. In fact, despite their pervasive use in biomedical applications, the assessment of their accuracy and reliability for motion tracking has been only partially addressed [3]. With the use of sensor fusion algorithms in combination with magneto-inertial sensor networks, it is possible to obtain orientation data to perform a kinematic reconstruction for motion tracking or feature extraction [4]. Those kind of data can be used for the assessment and the monitoring of patients with motor impairments [5] and the error in the output provided by these filter algorithms may represent an important issue to take into account. Our aim is to design a standard methodology to tune and optimize filter parameters in M-IMU sensor fusion algorithms, able to measure the error with respect of a ground truth (represented by the optical motion tracking system), in order to evaluate the goodness of these filters.

Finally, as already said before, the third goal is to use a reliable technology, in terms of both wireless communication and sensor technology, to objectively assess motor conditions of patients with neurological disorders. Among several possible pathologies with relevant movement deficits, we focus on Parkinson's disease. In fact, PD may highly benefit from the use of magneto-inertial sensors for the diagnosis and assessment of its motor symptoms: the exploit of these sensors could be fundamental to make a step forward in the capability of quantitatively describing patient's motor symptoms without the necessity of the presence of the physician. As a matter of fact, motor symptoms in PD are not only highly relevant, but they are also very representative of the evolution of the pathology; for this reason they are strictly related to diagnosis, assessment and monitoring [6]; indeed a very important part of the most widely used PD assessment clinical scale (*i.e.* the UPDRS scale) is focused on motor symptoms. This kind of evaluation is periodically done by the physician, who modifies the therapy in relation to the status of the disease. The clinical analysis, which is occasionally administered by the doctor, presents some limits: PD has fluctuations during different days, but also in the same day, which do not guarantee the efficacy of the medical assessment in the hospital. Another key point related to PD is the continuous necessity of the patient to take drugs (*e.g.* l-dopa) in order to reduce the symptoms given by the effect of the disease itself; that is evidenced by a switching from the OFF phase, when the symptoms are strongly present, to the ON phase. Our final goal is to use M-IMUs continuously monitor and assess PD to detect the fluctuations between these two phases in patients, so that it is possible to administer drugs in a targeted modality, specific to each patient, in order to improve effectiveness and reduce side effects [5].

1.3 Contributions

The main contributions of this thesis are related to the research goals above mentioned and are briefly stated in order of appearance:

- I performed for the first time an extensive and systematic analysis of Bluetooth Low Energy, in order to demonstrate whether BLE is a suitable candidate for wireless communication in high throughput and low energy sensor network applications. In particular, my main contributions are:
 - An extensive review of the state of the art about Bluetooth Low Energy (BLE), analyzing its performance and limits in order to have a clear state of this communication technology and the parameters which substantially influence its characteristics.
 - An investigation of BLE performance in a sensor network with a star topology. The aim is to understand how to push its characteristics over the limit already tested and reached in the state of the art, in order to obtain satisfactory results that can be used in the assessment of patients with motor impairments. In particular, we analyze the throughput in relation to the different number of nodes, in order to understand how to configure and use this communication technology in specific applications, such as motion analysis with magneto-inertial sensors. In addition to this, we also investigate the power consumption of BLE nodes in relation to set up parameters. Defining a standard methodology to test wireless sensor networks, we tested BLE performance in a sensor network with a star topology, showing the possibility to use this communication technology in high data rate applications (~170 kbps), thus enabling the streaming of 5 nodes with 9-axes M-IMU data (16 bits of resolution per axis) at more than 200 Hz. frequency.
- We propose a methodology for the evaluation and optimization of sensor fusion algorithms for the orientation estimation by means of M-IMUs. More specifically, we introduce:
 - A method to generate synthetic M-IMU data in $SO(3)$ from a known trajectory and a defined error model of each sensor. These data may be used to understand the behaviour of M-IMUs in a structured environment, avoiding random errors existing in real acquisitions.
 - A methodology used to tune the gain parameters of each filter in order to minimize the filter error for the specific dynamic characteristics of the analyzed motor task.

- The design of a protocol used to assess the orientation error obtained from M-IMU sensor fusion filters. The results show how filters' performance may be different depending on the application and we propose a standard way to identify the filter's algorithm and the specific gains which guarantee the best performance for the specific task.
- We assess Parkinson's Disease by means of M-IMUs. In particular, we use these typology of sensors to evaluate PD's cardinal motor symptoms in different tasks of its clinical scale, *i.e.* the UPDRS:
 - Assessment of bradykinesia and rigidity with a M-IMU network positioned on the upper limb most affected by PD, while performing finger tapping and arm pronosupination tasks. The main contributions of this protocol regard the identification of the most sensible places where to locate sensors to monitor bradykinesia and rigidity, and also the extraction of indexes able to discriminate PD patients during the different phases, but also patients to healthy subjects.
 - The evaluation of PD's status using one M-IMU sensor on the trunk, while performing a sit-to-stand task. The main contribution of this study is to propose a broad method for the detection of the most relevant features for the analysis of this particular task, that is strongly related to activities of daily living. We select a small pool of features which best represent pathology fluctuations in PD and differences between patients and healthy subjects.

1.4 Outline of the thesis

This dissertation includes three main topics organized in as many chapters.

Chapter 2 introduces the importance of the wireless communication technology implied in the sensor network used, and in particular it describes Bluetooth Low Energy (BLE), a low power standard technology widespread in a huge number of applications. The first Section of this chapter regards this protocol, its known characteristics and the tested performance in accordance with the state of the art. In the following part (Section 2.2) we investigate some characteristics of this communication technology, *e.g.* throughput and power consumption, trying to push it over the limits already known in the literature.

In Chapter 3 it has been introduced the magneto-inertial measurement unit (M-IMU) which is the main sensing element that has been used in the presented research and the principal source of information applied in the implemented algorithms. The aim of the

first section of this chapter is to provide a comprehensive overview of these devices, taking into account their main aspects, such as functioning, configuration, calibration and sensor modeling. Section 3.2 describes how to use sensor fusion algorithms which exploit M-IMUs to obtain orientation of a body in the space. In the last section of this chapter, we propose a standard methodology to tune sensor fusion filters and evaluate their performance in order to choose the solution which provides the lowest error for the specific application of interest.

Chapter 4 discusses the final main topic of this dissertation, *i.e.* the use of the M-IMU network in the assessment of motor impairments due to neurological diseases, focusing in particular on Parkinson's disease (PD). PD patients often need to go to an hospital to be monitored by a physician which uses a specific clinical scale, *i.e.* the UPDRS, to assess the level of the pathology. We try to evaluate the status of the disease by means of M-IMUs during the execution of particular tasks, with the idea to have more objective data, independent of the presence of the doctor and his analysis. In conclusion, with our data we want to confirm the reliability in using low cost, low energy system able to monitor and evaluate PD.

Finally, Chapter 5 concludes the dissertation and gives an overview of future works which may start from here.

Chapter 2

Motion sensor network with low energy wireless communication

Citations:

- [J.I] **Jacopo Tosi**, Fabrizio Taffoni, Marco Santacatterina, Roberto Sannino, and Domenico Formica. Performance evaluation of Bluetooth Low Energy: A systematic review. *Sensors (Switzerland)*, 17(12):2898, 12 2017.
- [J.III] **Jacopo Tosi**, Fabrizio Taffoni, Marco Santacatterina, Roberto Sannino, and Domenico Formica. Throughput Analysis of BLE Sensor Network for Motion Tracking of Human Movements. *IEEE Sensors Journal*, 19(1):370–377, 2019.

The first part of this PhD project is focused on the design and development of a sensor network based on low energy wireless communication. The aim is to build a general purpose network, in order to make it easily exploitable in several typologies of application in the biomedical field. In bioengineering and healthcare in general, most of the existing Wireless Sensor Networks (WSNs) are Body Area Networks (BAN), *i.e.* networks made of wearable sensor to monitor the subject, also applied in telemedicine contexts. From the BAN subsystem, to the end-user healthcare monitoring application, it is crucial to take into account some design considerations [7].

- modularity and scalability: the structure of the network has to freely vary in order to change the number and typology of sensors connected in it. It is very important also to strengthen its architecture so that it can be flexible and evolve over time, independently on the hardware used.

- power consumption: in biomedical field, there are several applications in telemedicine, which implies a constant monitoring of the patient's vital signs. It is important to build a system which lives for long times in order to acquire as much data as possible without changing the batteries, which represents a burdensome task in BAN. Exactly for this reason, one of the main issues about these typologies of networks is to use energy efficient protocols and sensors [8].
- mobility and unobtrusiveness: the patients have to wear the BAN devices all the time and mobility reduction is not acceptable. The sensor devices must be designed with the aim of providing the highest degree of mobility for the patients, that also implies a wireless communication protocol and a power supply provided by batteries [9].
- accessibility: in order to be achievable and accessible by the highest number of users, our systems should be low cost, user-friendly and compatible with other systems already present in the market.

Taking into account all the characteristics enumerated here above, the next step regards the decision-making process which drives through the design and development of the sensor network used.

The two main elements involved in the architecture of our network are the communication protocol and the typologies of sensors to be used.

For what it concerns the choice of the communication protocol to be implemented in the BAN, in the last five years Bluetooth Low Energy (BLE) represented an emerging and innovative technology which aimed to become the main character for BANs between the huge number of standard wireless technologies, already existing and widespread on the market (*i.e.* IEEE 802.11b (Wi-Fi), ZigBee, Ant+ and Bluetooth Classic) [10].

In addition to this, the synergy between good performance and ubiquitous diffusion (today BLE is available in all PCs, tablets and smartphones) makes BLE a optimum candidate for a great variety of applications; in the medical field for e-health [11] [12] [13] [14], *e.g.* in body area network [1] (using ECG [15] [16], heart rate sensor [17] [18], blood flowmeter [19], EMG for prosthetic hand control [20], an IMU sensor used for early diagnosis of Parkinson's disease [21]; it is also used to monitor respiration, activities and falls [18]), in automotive applications [22] [23], in voice communications [2], for kinematic tracking [24] [25], in domotics for healthcare environments and smart house [26] [27] [28] [29], for transmission of M-IMU data in game controlling [30], in security systems [31] [32], to understand crowd dynamic [33], and so on.

BLE may represent the perfect solution as communication technology in our BAN for movement analysis. In fact, all the M-IMU systems which may be used in biomedical field

nowadays have several issues which may limit our application's performance. For example, it is difficult to use a reliable BAN at home with a good bitrate for several nodes with M-IMU sensors. As a matter of fact, in research laboratories magneto-inertial sensors gave good results for the assessment in biomedical applications, but they usually do not use a widespread communication technology, that can be translated in a not portable system with an access point, *e.g.* Opal by APDM. In addition to this, these technologies are not low power, that means a short duration of the power supply (*e.g.* Xsens) or a bigger dimension of the batteries which make the device cumbersome.

As shown, until now BLE has usually been used for low throughput applications, and only in the last few years it has been started to be used for high throughput applications, but a multinode and high bitrate network has never been developed and tested.

Hence, we want to find a general purpose hardware (HW) as sensor module, with several magneto-inertial measurement units and a BLE integrated circuit (IC) to connect with. At the beginning of this work, STMicroelectronics (STM) put on the market the SensorTile¹, a module which matches with the characteristics we were looking for.

The remaining part of this chapter is developed as follows: in Section 2.1 BLE and its characteristics are described in detail, in Section 3.1 and the HW used is presented, in Section 2.2 it is shown how our BAN has been evaluated.

2.1 Bluetooth Low Energy: definitions, main features and characteristics

After a deep study of the state of the art, we found that Bluetooth Low Energy lacks a complete and systematic analysis of its real performance under different experimental conditions, which could help designers to develop optimized devices for specific applications. Thanks to these considerations, we decided to write a review paper on BLE, which presents an exhaustive description of its protocol, together with its limits and characteristics, and an overview of the literature [34]. In this Section we are going to show an overview of Bluetooth Low Energy and its characteristics, in order to let the reader understand how it works and its role in the applications.

Bluetooth Low Energy (BLE), also known as Bluetooth Smart or Bluetooth 4, is a wireless communication technology developed by the Bluetooth Special Interest Group (SIG). It is designed to operate in the Industrial, Scientific and Medical (ISM) band included in 2.4.2.5 GHz, that means that it is available to be used in biomedical applications.

¹STMicroelectronics, "STEVAL-STLKT01V1: SensorTile development kit," DB2956, 2017.

Bluetooth Low Energy protocol is structured in a stack composed of three main blocks [35] [36] [37] [38]: the *Application*, the *Host* and the *Controller*, as shown in Figure 2.1. Each layer in the protocol incorporates its lower layer. The raw data, acquired from the antenna, are consequently encapsulated in a standard BLE packet, shown by the arrow on the left. On the other side, a BLE packet that shall be sent by a transmitter is fragmented in raw data and then managed by the *Controller*, as shown by the arrow on the right.

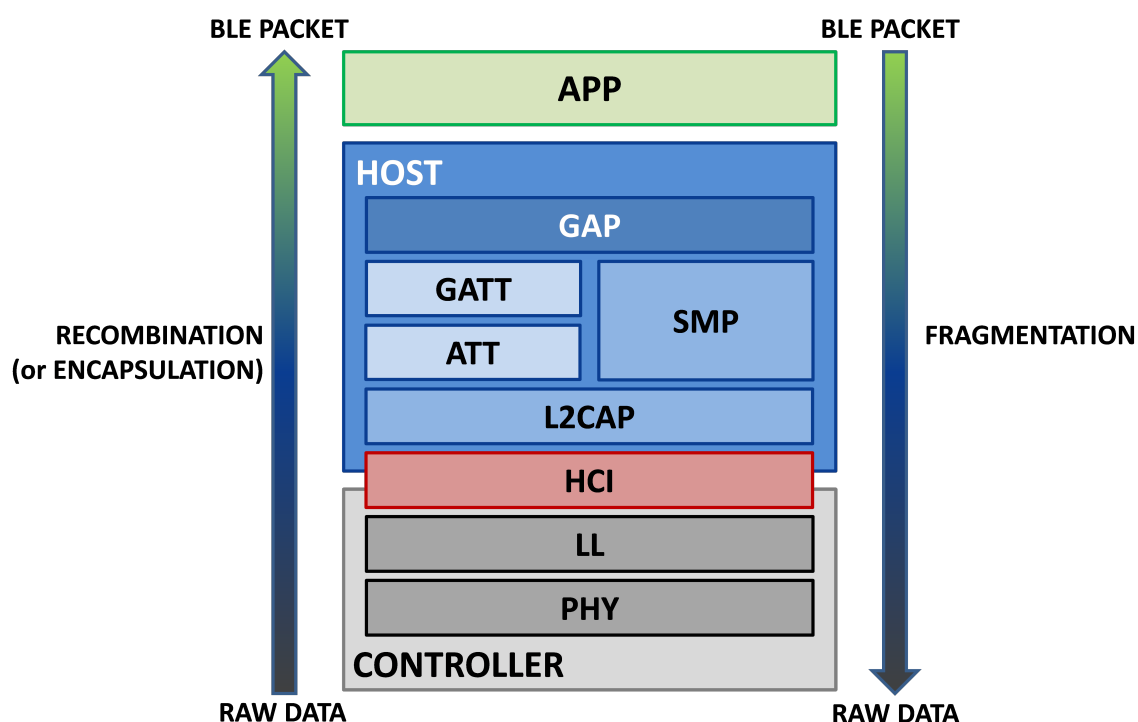


Fig. 2.1 BLE protocol stack. The three main blocks are the *Controller* (grey), the *Host* (blue) and the *App* (green). The *Host Controller Interface (HCI)* (red) is the interface which manages the communication between the two layers adjacent to it. The rectangular frames represent the different parts of the layers, described in detail in [34]. The two arrows represents the direction encapsulation and fragmentation of BLE packets.

The BLE architecture has maintained some common parts of previous Bluetooth versions (*i.e.* Classic Bluetooth), in order to have new devices compatible with both standards (*Smart Ready*). The protocol architectures of Classic Bluetooth, BKE and *Smart Ready* devices are shown in Figure 2.2, pointing out differences and equalities between the protocols.

2.1.1 BLE Communication

Investigating the structure and the functioning of a BLE network is important to understand how it communicates and the roles a device can play. BLE devices can communicate using

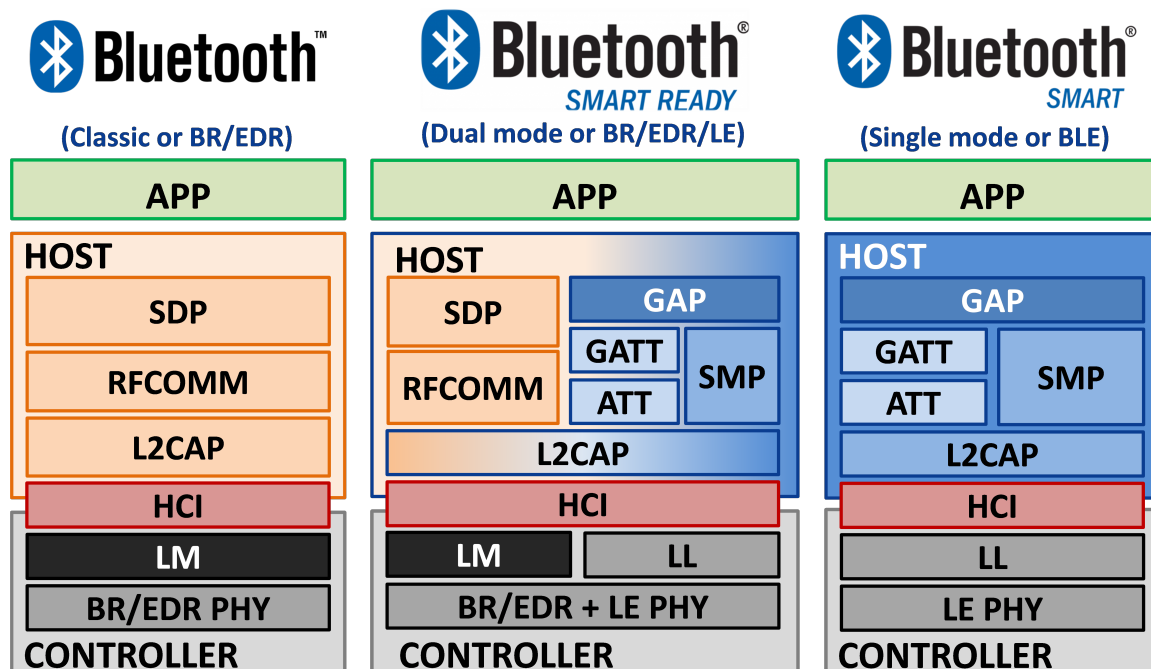


Fig. 2.2 Different standard versions of Bluetooth protocols. In the left there is the structure of Classic Bluetooth, on the right there is the BLE, while in the middle there is the protocol stack compatible with both Bluetooth versions, *i.e.* *Smart Ready*.

two main modalities: *broadcasting* and *connections* [39] [40]. In the following part of this section we are only going to describe *connection* modality, since we have only used it in all the experiments.

A *connection* is a permanent, periodical data exchange of packets between two devices [40]. The *connection* is private, and it may also be protected with security provisions. In *connections*, there are two different roles involved, defined in the Generic Access Profile (GAP) [40]:

- The *Central (master)* scans for connectable advertising packets and initiates the *connection*. When the *connection* is active, the *central* manages all the setting and starts a periodical packet exchange.
- The *Peripheral (slave)* periodically sends connectable advertising packets and accepts *connections* initiated by the *master*. When the *connection* is established, it follows the settings exposed by the *central* and exchanges data with it.

A *connection* between a *master* and a *slave*, shown in Figure 2.3, follows predefined times: the time in which the *master* exchanges data packets with the *slave* is called *Connection*

Event (*connEvent*), while the rest of the time, when the communication is off is the *Radio Idle*. The start of a *connEvent* is called the *anchor point*; at the *anchor point*, the *master* shall start to transmit packets to the *slave*. The sum of *connEvent* and *Radio Idle* is called *Connection Interval* (*connInterval*). The *connInterval* shall be a multiple of 1.25 ms in the range of 7.5 ms and 4.0 s.

As can be seen in Figure 2.3, a data packet exchange is usually followed by another packet called Acknowledgment (ACK), *i.e.* a packet without data which provides error recovery capabilities. If the communication is notifiable, the ACKs are not sent.

There are two main communication modalities the *master* may use to exchange data with the *slave*:

- In *one-way* communication, the *slave* sends a simple notification in response to a poll from the *master*. This is typical of the notifiable communications.
- In *round-trip* communication, the *master* firstly asks for data to the *slave*, then this one transmits a response. The difference is that both messages, the request and the response, generate an ACK. The interval of time between the beginning of two consecutive data packet, including the ACK, is called $T_{round-trip}$.

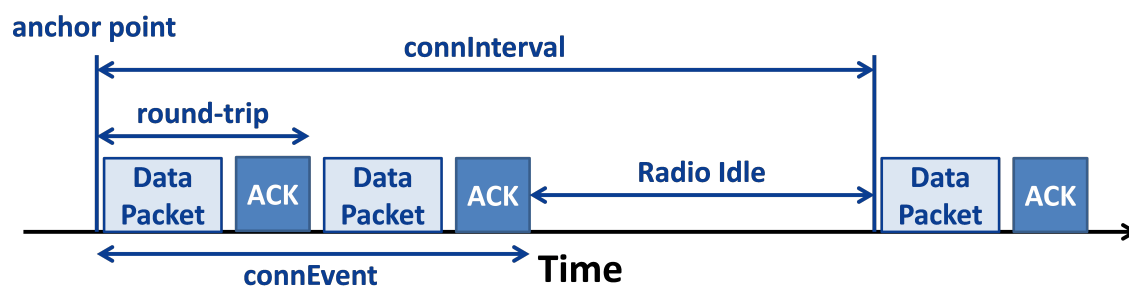


Fig. 2.3 Example of a *round-trip* data communication in a *connection* with the transmission of data packets and ACKs. In this Figure are described all the parameters referred to the *connection* communication.

Other parameters, used to set up BLE *connections* are the *Connection Supervision Timeout* (*connSupervisionTimeout*) and the *Connection Slave Latency* (*connSlaveLatency*). The *connSupervisionTimeout* is the maximum time that can flow without receiving two valid packets, before the connection is lost. It should be a multiple of 10 in the range between 10 ms and 32000 ms. The *connSlaveLatency* is the amount of *connEvents* that can be skipped without the risk of disconnection. Its value should not cause a *connSupervisionTimeout*, and it shall be an integer in the range of zero to $((connSupervisionTimeout / (connInterval \times 2))$

–1). Moreover, *connSlaveLatency* shall not be less than 500, and when it is set to zero the *slave* device shall listen to at every *anchor point*, without loosing the connection.

2.1.2 BLE Packet

As described in Section 2.1.1, BLE allows two types of communication (*i.e. broadcasting* and *connection*), which implies two different packet typologies, which share a common structure, as shown in Figure 2.4. This structure is divided into four mandatory subsections, defined in the BLE Specifications [39] [41], and described as follows:

- The *Preamble* (PRE) is a very simple sequence of bits used by the receiver to set its automatic gain control and determine the frequency corresponding to the radio data rate itself.
- The *Access Address* (AA) is used to exclude packets directed to different receivers.
- The *Protocol Data Unit* (PDU) range is from 2 to 257 bytes, and its length is strictly dependent on the communication used.
- The *Cyclic Redundancy Check* (CRC) checks the presence of errors, analyzing the PDU only, which could have been generated during packet transmission.



Fig. 2.4 BLE packet structure. The packet has one or two bytes of PRE, depending on the radio data rate, four bytes of AA, from 2 to 257 bytes of PDU and three bytes of CRC.

The PDU part of a *connection packet* (Figure 2.5) is composed of a two-byte header, which contains several parameters, described in detail in [41]. For what it concerns the maximum payload for data packets is 20 bytes, set by BLE specifications [42]. Moreover, there is an optional Message Integrity Check (MIC) value of four bytes, which is used to authenticate the data PDU in an encrypted connection.

2.1.3 BLE Network Topology

A BLE basic network, composed by a *master* and a *slave*, is called *piconet*. With the updating to Version 4.1 of the Bluetooth Specification, each device has the capability to perform

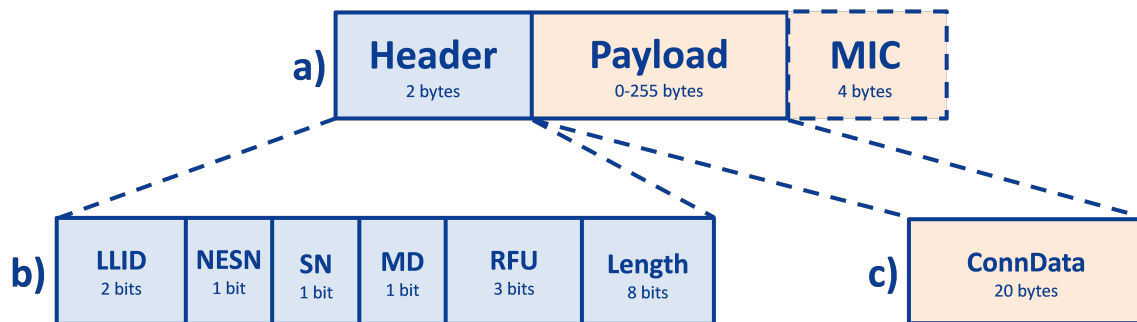


Fig. 2.5 PDU structure of a BLE connection packet.

simultaneously both roles, *master* and *slaves*, in different *piconets*. This type of network is called *scatternet*. In the Bluetooth Specifications [41], some types of BLE topology are shown in detail, as summarized in Figure 2.6.

Group (a) in Figure 2.6 is a simple *broadcasting* topology, where A is an *advertiser*, while B and C are *scanners*, which are using a BLE advertising physical channel.

Group (b) is a basic *piconet*, with only one physical channel, where D acts as *master* and E as *slave*.

In group (c), the *master* is F, and it is using two *piconet* physical channels with *slaves* G and H. Device F is also the *initiator* of the connection with device I, which is advertising with connectable advertising packets on the advertising physical channel; device F can start the connection and add *slave* I to its *piconet*. A network topology like this one, with only one *master* and several *slaves*, is called a star network.

In *scatternet* (d), device J is using one LE physical channel with K and one with L. J is the *master* in the *piconet* with L and the *slave* in the one with K.

In *scatternet* (e), device M is the *slave* of two physical channels, whose *masters* are N and O. Device P is advertising using a connectable advertising event on the advertising physical channel, and the device M is the *initiator*; when the connection is formed, M will result in being the *master* of this link.

2.2 BLE performance analysis in a sensor network for M-IMU applications

Although BLE has already been successfully used in a great variety of applications, it lacks of a systematic experimental validation of its main characteristics, as already exposed in [44].

To fill this lack in the literature related to throughput, and or the impossibility to model all the possible parameters of BLE, we decided to identify a method to systematically measure

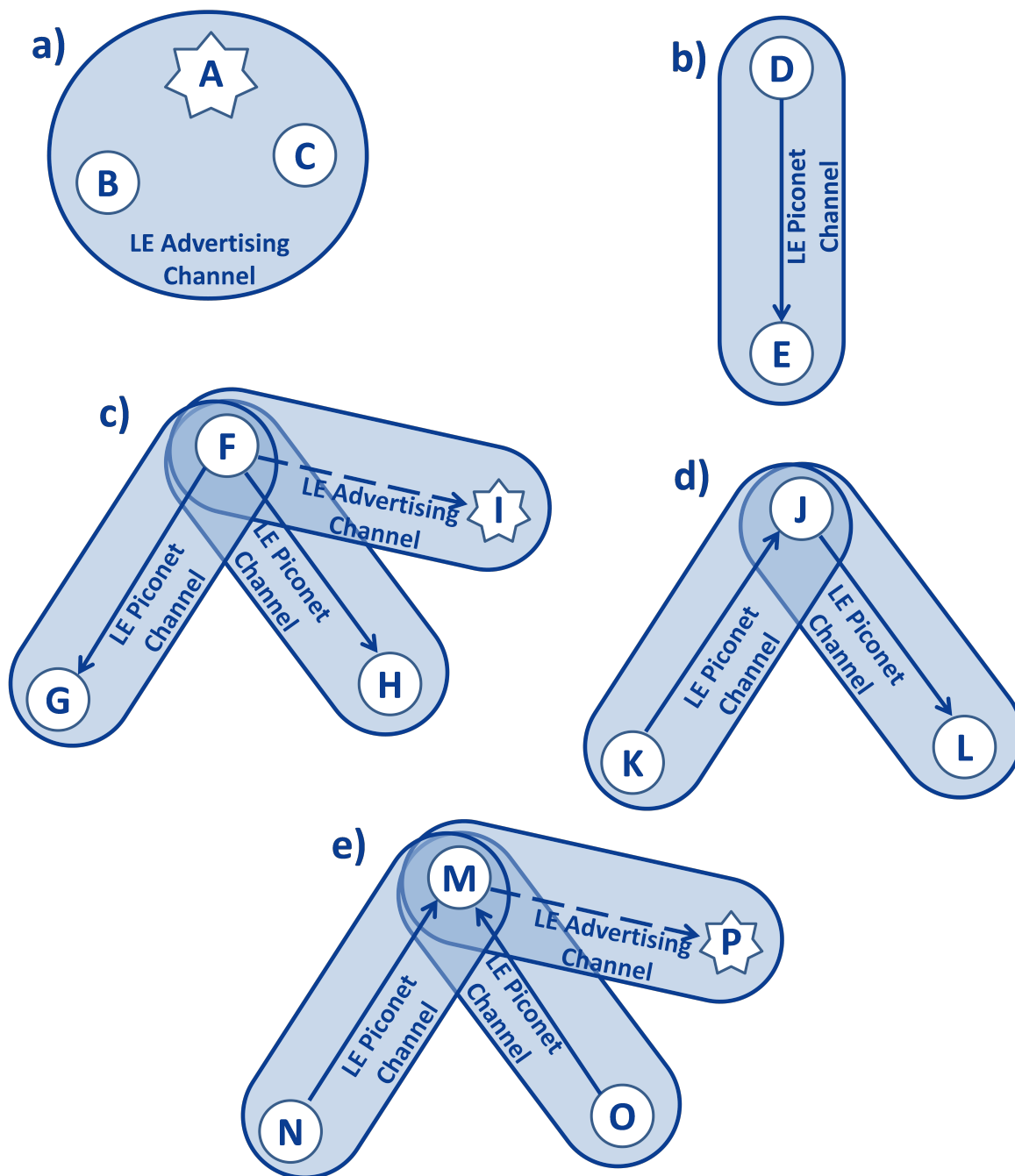


Fig. 2.6 Example of BLE topology [43]. In the Figure, solid arrows point from *master* to *slave*; dashed arrows, indicating a connection initiation and point from *initiator* to *responder*. Each device is represented with a capital letter; devices that are connected are represented with a circle, while devices that are advertising are indicated using stars.

the actual performance of the communication. In addition to this, we also evaluated the power consumption of the sensor unit used, in order to estimate the battery life.

As a matter of fact, our objective is to obtain a reliable, low energy, user friendly and easy-to-use sensor network for motion tracking, and we need to investigate if BLE performance are acceptable for these typology of applications.

2.2.1 Assessment of throughput and number of nodes

System Architecture

In order to evaluate BLE throughput we designed a star network architecture with a *central* node and several *peripheral* nodes. Different typologies of devices are used in our experiments, in order to understand the variability introduced by the software (SW), firmware (FW) or hardware (HW).

Central nodes used in this experiment are a LG Nexus 5 (**M1**), Figure 2.7a, with Android 6.0.1 and Broadcom BCM4339 WiFi Bluetooth IC; a Samsung Galaxy Tab S2 (**M2**), Figure 2.7b, with Android 7.0, mounting a Broadcom BCM4330 integrated circuit for WiFi and Bluetooth communication; and a stack of two STMicroelectronics boards (**M3**), Figure 2.7c, the microcontroller unit (MCU) NUCLEO-F401² and *BlueNRG* expansion X-NUCLEO-IDB05A1³.

Peripheral nodes are of two typologies: SensorTile⁴ (**S1**), Figure 2.7d, *i.e.* a module embedding a MCU, a BLE IC (*BlueNRG*), and several MEMS; a stack of three ST boards (**S2**), Figure 2.7e, the MCU (NUCLEO-F401⁵), a board with BLE radio and chip (X-NUCLEO-IDB05A1⁶), and the sensor expansion board (X-NUCLEO-IKS01A1⁷) with MEMS sensors.

Our specific scope is to design a BAN for kinematic reconstruction, and exactly for this reason, both the *peripheral* sensor boards include M-IMUs.

²STMicroelectronics, "STM32F401xD STM32F401xE: ARM cortex-m4 32B MCU+FPU, 105 DMIPS, 512kB flash/96kB RAM, 11 TIMs, 1 ADC, 11 comm. interfaces," DS10086, 2017.

³STMicroelectronics, "X-NUCLEO-IDB05A1: Bluetooth low energy expansion board based on the SPBTLERF module for STM32 nucleo," DB2592, 2015.

⁴STMicroelectronics, "STEVAL-STLKT01V1: SensorTile development kit," DB2956, 2017.

⁵STMicroelectronics, "STM32F401xD STM32F401xE: ARM cortex-m4 32B MCU+FPU, 105 DMIPS, 512kB flash/96kB RAM, 11 TIMs, 1 ADC, 11 comm. interfaces," DS10086, 2017.

⁶STMicroelectronics, "X-NUCLEO-IDB05A1: Bluetooth low energy expansion board based on the SPBTLERF module for STM32 nucleo," DB2592, 2015.

⁷STMicroelectronics, "X-NUCLEO-IKS01A1: Motion MEMS and environmental sensor expansion board for STM32 nucleo," DS10619, 2015.

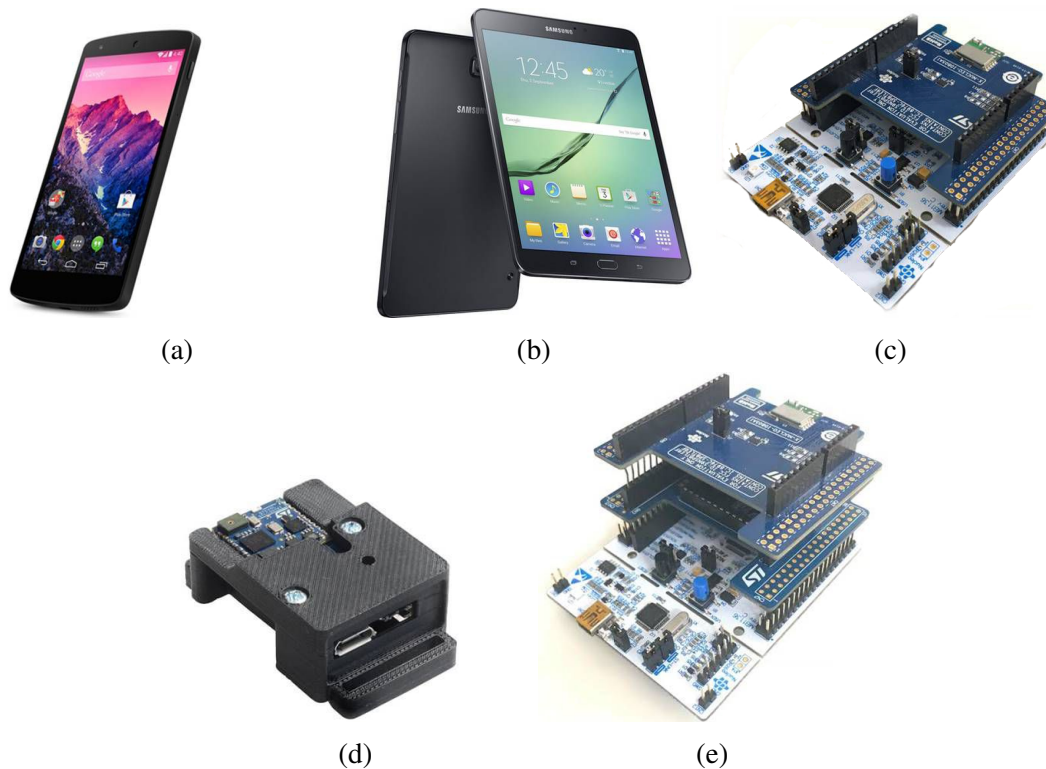


Fig. 2.7 All the different typologies of devices that have been used in the system architecture of this work, described in detail in Section 2.2.1. The first row (Fig 2.7a, 2.7b, 2.7c) contains *master* nodes, while the second (Fig 2.7d, 2.7e) the *slaves*. (a) **M1**. (b) **M2**. (c) **M3**. (d) **S1**. (e) **S2**.

The FW embedded in MCUs has been programmed in C code, using the development environment *System Workbench for STM32*⁸, and it has been adapted from official source codes available on ST website^{9,10}.

For what concerns *master* nodes based on Android operative system, we developed an App programmed in Java which uses official Android APIs and drivers, so that it is portable and supported on different mobile devices. In order to obtain the best performance, it is important to set **M1** and **M2** in flight mode, and in particular to turn off WiFi, because it usually shares the same integrated circuit (IC) of Bluetooth, so it may compromise the results. In addition to this, we also killed all the open Apps in the device, so that the workload of the other tasks of the operating system do not significantly influence our experiment.

⁸STMicroelectronics, System Workbench for STM32: free IDE on Windows, Linux and OS X.

⁹STMicroelectronics, X-CUBE-BLE1: Bluetooth Low Energy software expansion for STM32Cube, DB2461, 2017.

¹⁰STMicroelectronics, FP-SNS-ALLMEMS1: STM32 ODE function pack for IoT node with BLE connectivity, digital microphone, environmental and motion sensors, DB2915, 2018.

Protocol

The protocol designed for the experiment consists in sending M-IMU data packets from *slaves* to *master* using a BLE *notifiable characteristics*. The use of this type of *characteristic* has been chosen because it sends less protocol packets, as already described in Section 2.1.1, so it can reach a higher effective throughput.

All the possible combinations of *master* and *slave* have been set (**M1-S1**, **M1-S2**, **M2-S1**, **M2-S2**, **M3-S1**, **M3-S2**).

The number of *slaves* of the star network changes from 1 to 5, within a range of 20 cm, with the power level of the radio set to 4.7 dBm.

In each acquisition the value of *connInterval* and the number of packets sent per *connInterval* vary. For each couple of parameters (*i.e.* *connInterval* and number of packets per *connInterval*) we send data until the *master* receives 1000 packet from each *slave*. In our protocol, the possible values of *connInterval* expressed in ms are: 7.5, 11.25, 13.75, 16.25, 18.75, 21.25, 46.25, 71.25, 96.25. This choice has been done since 7.5 ms is the minimum value that can be set in accordance with BLE protocol (Section 2.1.1), and we decided to make it firstly vary with little steps, then higher, in order to investigate a quite wide interval. The value of 7.5 ms can be used only with **M3**, in fact we noticed with the BLE sniffer (Frontline ComProbe BPA 600¹¹) that Android imposes a minimum *connInterval* of 11.25 ms; of note that we tested only two Android versions (*i.e.* Android 6.0.1 and 7.0). On the other hand, regarding **M3**, there are some limits imposed by BLE protocol and vendor firmware that do not allow to acquire at specific low values, when the network has more than 2 nodes (11.25 ms with 3 nodes; 16.25 ms with 4 nodes; 18.75 with 5 nodes). All these cases, in which it has not been possible to acquire data with particular BLE connections parameters, are represented in Figures with white bars.

For what concerns the number of packets sent per each *connInterval*, we decided to make it vary from 1 to 6. In addition to this, a further limit on M-IMU data transmission depends on the maximum sampling rate of the sensor boards; for our setup, the minimum sampling period to have access to all 9-axes data of M-IMU sensor is 1.8 ms, thus the upper bound of bitrate for each *slave* node is around 89 kbps.

Other BLE connection parameters that have been set and maintained constant for the whole protocol duration are *connSupervisionTimeout*, equal to 32000 ms, and *connSlaveLatency*, equal to zero (Section 2.1.1).

¹¹I. Frontline Test Equipment, "ComProbe BPA 600 dual mode bluetooth protocol analyzer," frontline Test Equipment, Inc: Charlottesville, Virginia, United States.

Throughput Evaluation

As already said, BLE 4.1 protocol puts the limit of packet payload to 20 bytes. We use the whole payload to send M-IMU data packet, in fact, as shown in Figure 2.8, each sensor embeds tri-axial accelerometer, gyroscope and magnetometer and uses 2 bytes per axis, that means 18 bytes in total. In addition to this, we used 2 bytes to save timestamp (*TS*), *i.e.* the time saved when *slave* acquires data from the sensor¹².



Fig. 2.8 Structure of a protocol data packet. The first 18 bytes are reserved to M-IMU data, 6 for each sensor (*i.e.* accelerometer, gyroscope, magnetometer), in detail 2 bytes for each axis. In the last 2 bytes the timestamp (*TS*) is saved.

Since we know the *connInterval* measured in ms, the number of packets sent in each *connInterval* (*nPackets*) and the data packet payload, we can easily compute the theoretical data throughput sent by each *slave*, measured in kbps:

$$Throughput_{th} = \frac{nPackets}{connInterval} \cdot 20 \text{ byte} \cdot \frac{8 \text{ bit}}{1 \text{ byte}} \quad (2.1)$$

To test packet loss during transmission, we designed the protocol to successfully transmit 1000 packets of M-IMU data in order to estimate the correct value of throughput.

Hence, collecting the *TS* of the first and the last (*i.e.* the 1000th) packet received by the *master* expressed in ms, it is possible to evaluate the effective throughput of the transmission¹³. Thus:

$$Throughput_{eff} = \frac{1000 \text{ packets}}{TS_{last} - TS_{first}} \cdot 20 \text{ byte} \cdot \frac{8 \text{ bit}}{1 \text{ byte}} \quad (2.2)$$

Knowing the theoretical and the effective throughput, it is easy to compute the percentage of the packet loss (*PL*).

$$PL = \frac{Throughput_{th} - Throughput_{eff}}{Throughput_{th}} \cdot 100 \quad (2.3)$$

¹²It is the time that has passed since the beginning of the acquisition, expressed in ms.

¹³Note that *master* will wait to successfully receive 1000 packets before computing the effective throughput; *i.e.* 1000 is not the number of packets sent by the *slave*, but it is referred to the number of packets actually received by the *master*.

In data analysis we considered unacceptable all the configurations with a *PL* higher than 1%, since this error is too high for applications of M-IMUs to human motion tracking. Hence, we decided to consider a transmission as unsuccessful when the percentage of packet loss is higher than 1%. In addition to this, we computed the maximum value of throughput and the related configuration parameters (*connInterval* and number of packets per *connInterval*), in order to understand how to configure the sensor network to reach the best performance.

Results

Between **S1** and **S2** exists a very subtle difference for what concerns their throughput performance; on average, results of **S1** are slightly better than those obtained with **S2** (0.35 ± 0.10 kbps, mean value and standard error). In addition to this, in some specific BLE connection there are also peaks of 20 kbps of difference, always in favor of **S1**. For this reason, and also because **S1** is more suitable for BAN applications given its low weight and small dimension, we exposed extensively the results related to **S1** for different network configuration, while we reported only aggregate data for **S2**.

Figure 2.9, 2.10, 2.11 and 2.12 show main results about M-IMU data acquisition using a star network based on the three different *masters* (**M1**, **M2** and **M3**), with SensorTile (**S1**) as *slave* node. In particular Figure 2.9 and 2.10 show respectively packet lost and throughput for different sets of configuration parameters (*connInterval* and number of packets per *connInterval*) when the star network has only one *peripheral* node, *i.e.* a point-to-point connection; Figure 2.11 and 2.12 show the same results for the star network with five nodes. These two cases represent the limit cases of our study. The value of the throughput is referred to the average throughput of the *peripheral* node.

Examining Figure 2.10 and 2.12, it is clear that, between the two smart devices, **M2** has generally better performance than **M1**. In fact, the average difference between the value of throughput of the two *masters* (*i.e.* **M1** and **M2**) is 4.52 ± 0.37 kbps (mean value and standard error), with peaks of differences higher than 40 kbps.

As can be seen in Figure 2.9, the percentage of packet loss for the two smart devices **M1** and **M2** when 5 or 6 packets per *connInterval* are sent is relevant even when a single *slave* is connected; that means that for practical applications the maximum number of packets per *connInterval* with these two devices should not exceed 4. On the contrary, when the network is based on **M3** as *master* there is no packet loss when 1 single *slave* is sending data (Figure 2.9c), even when 5 and 6 packets per *connInterval* are sent. This limitation is probably due to Android libraries, even though it cannot be found in official manuals or documentation.

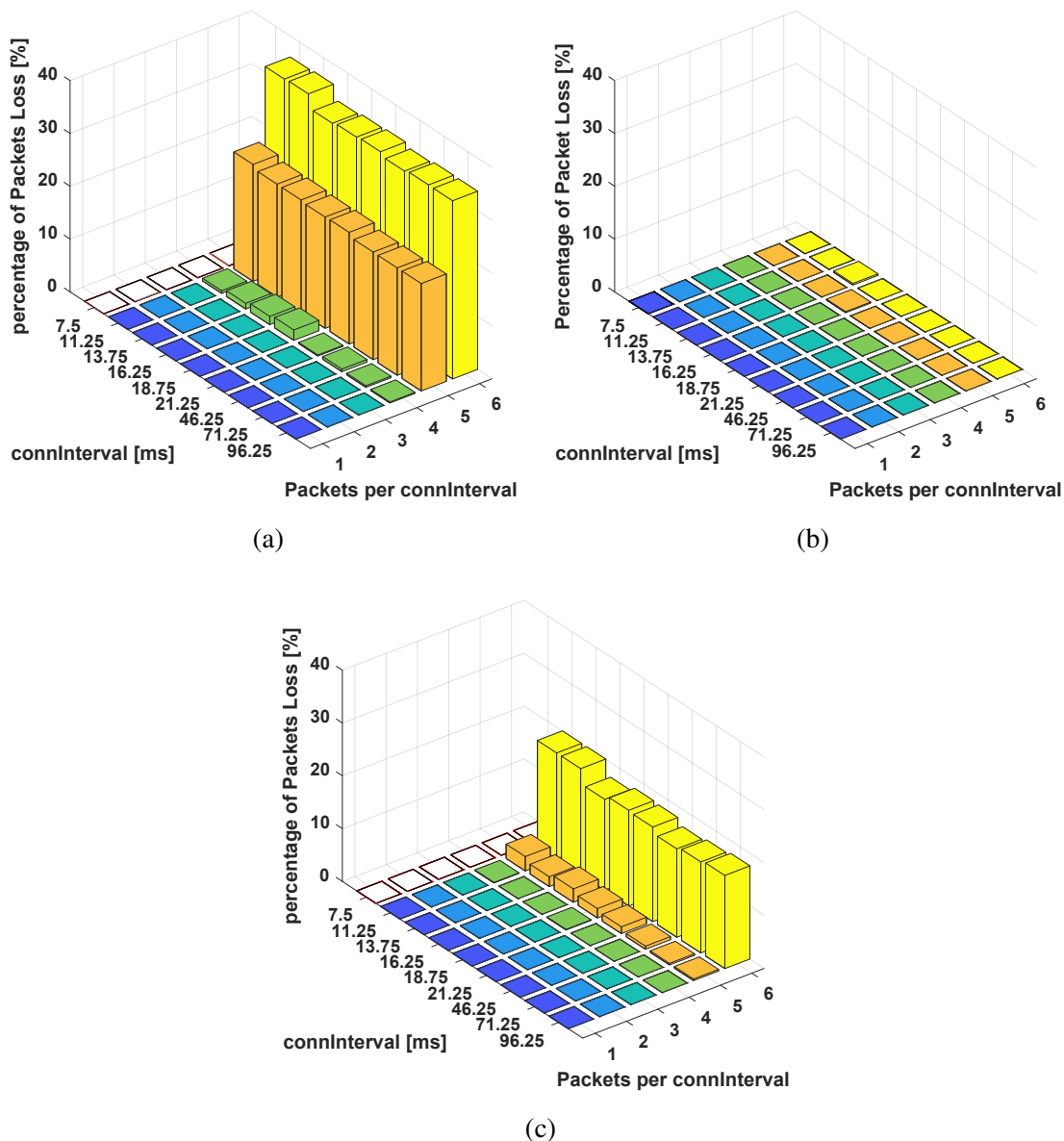


Fig. 2.9 This Figure shows the percentage of packet lost, computed using Equation 2.3. In all three cases, it has been used the **S1 peripheral** node. The network has 1 *slave* node. In Fig 2.9a the *master* is **M1**, in Fig 2.9b is **M2**, in Fig 2.9c is **M3**. On the x axis are represented the values of $connInterval$, measured in ms, while on the y axis is represented the number of packets sent per each $connInterval$. White bars indicate cases for what it has not been possible to execute the acquisition, due to protocol limits or its implementation in the specific device.

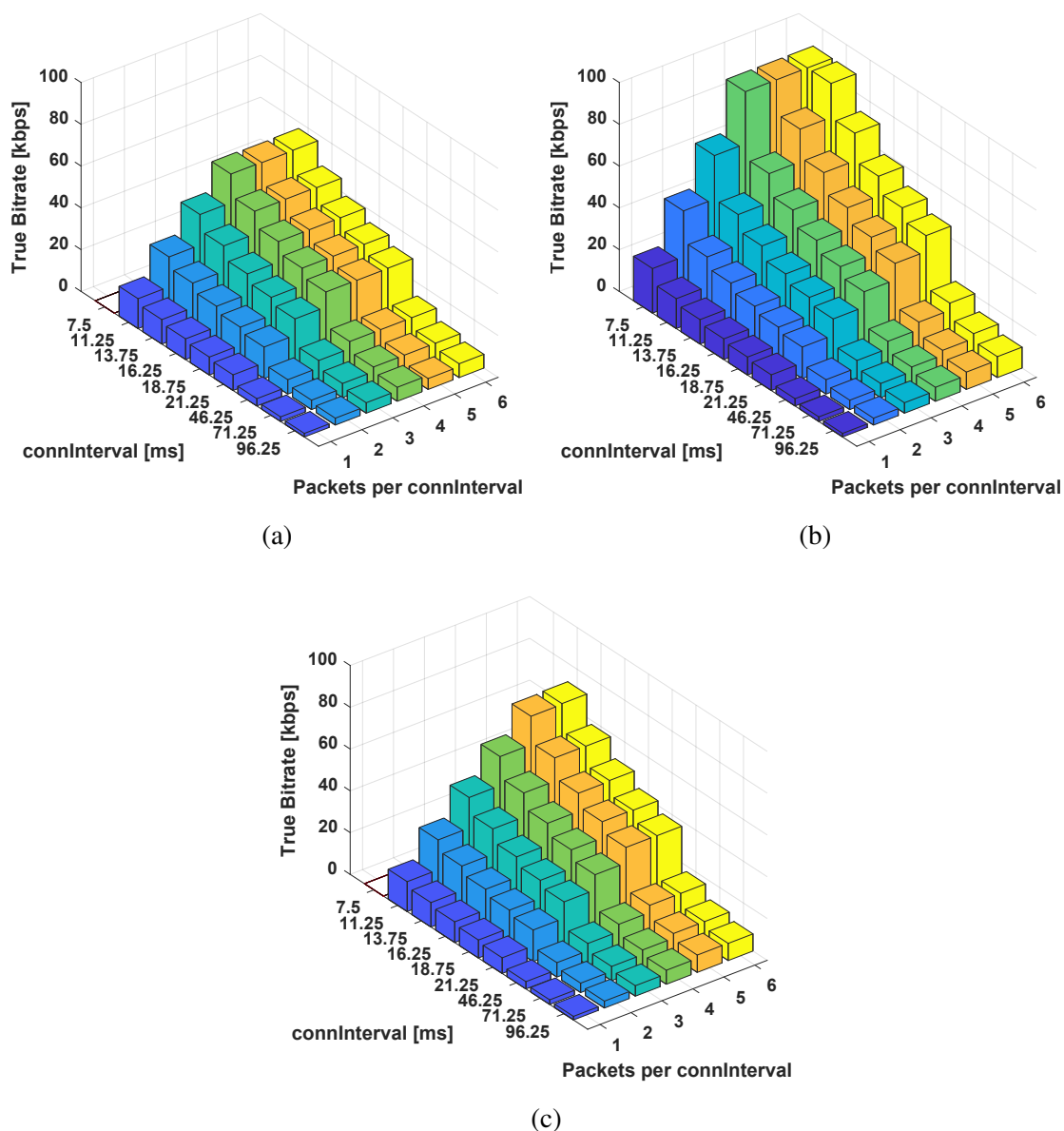


Fig. 2.10 This Figure shows the effective throughput, computed using Equation 2.2. In all three cases, it has been used the **S1 peripheral** node. The network has 1 *slave* node. In Fig 2.10a the *master* is **M1**, in Fig 2.10b is **M2**, in Fig 2.10c is **M3**. On the x axis are represented the values of *connInterval*, measured in ms, while on the y axis is represented the number of packets sent per each *connInterval*. White bars indicate cases for what it has not been possible to execute the acquisition, due to protocol limits or its implementation in the specific device.

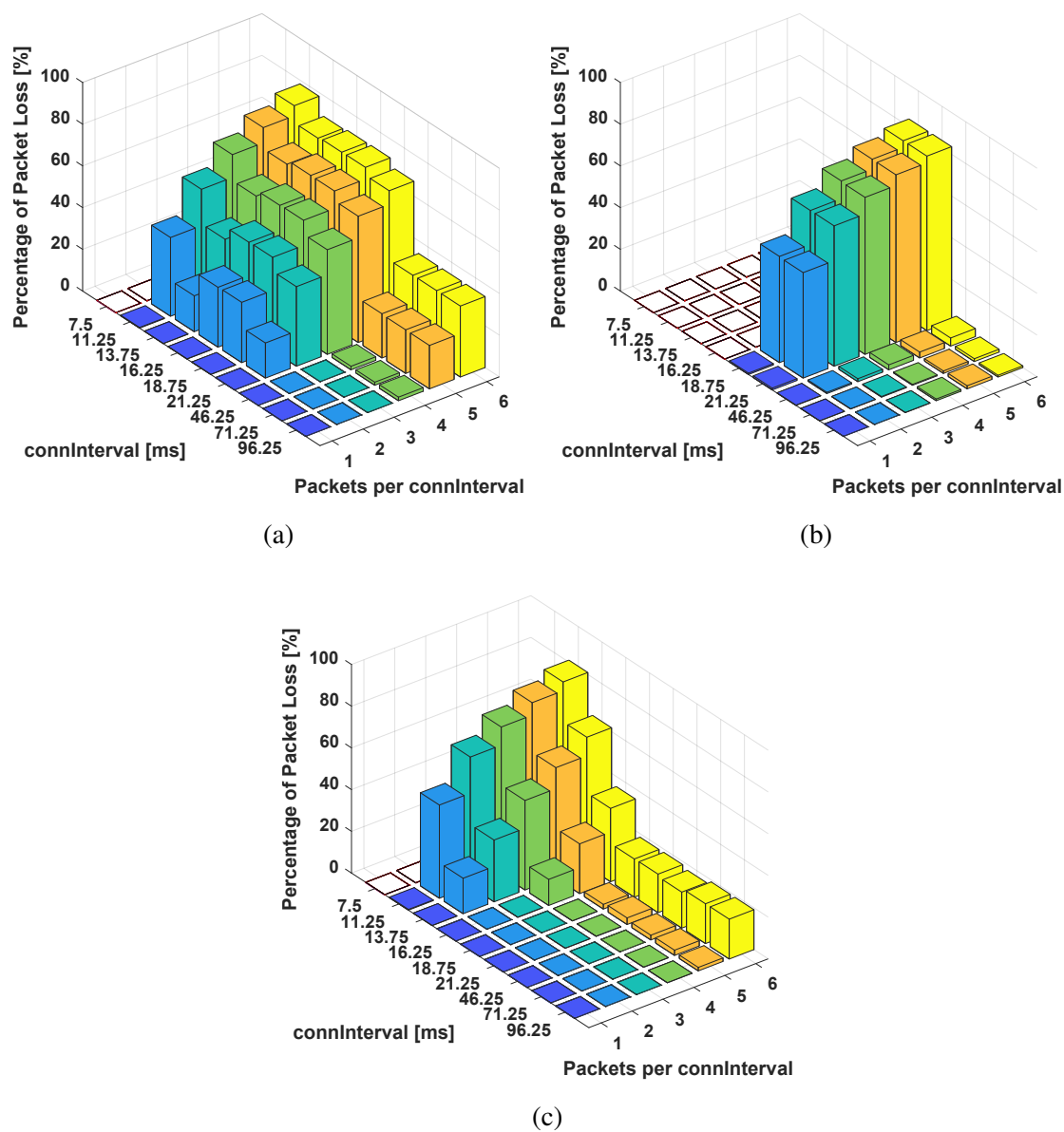


Fig. 2.11 This Figure shows the percentage of packet lost, computed using Equation 2.3. In all three cases, it has been used the **S1 peripheral** node. The star network has 5 *slave* nodes. The value of the percentage of packet loss is referred to the average throughput of the *peripheral* node. In Fig 2.11a the *master* is **M1**, in Fig 2.11b is **M2**, in Fig 2.11c is **M3**. On the x axis are represented the values of *connInterval*, measured in ms, while on the y axis is represented the number of packets sent per each *connInterval*. White bars indicate cases for what it has not been possible to execute the acquisition, due to protocol limits or its implementation in the specific device.

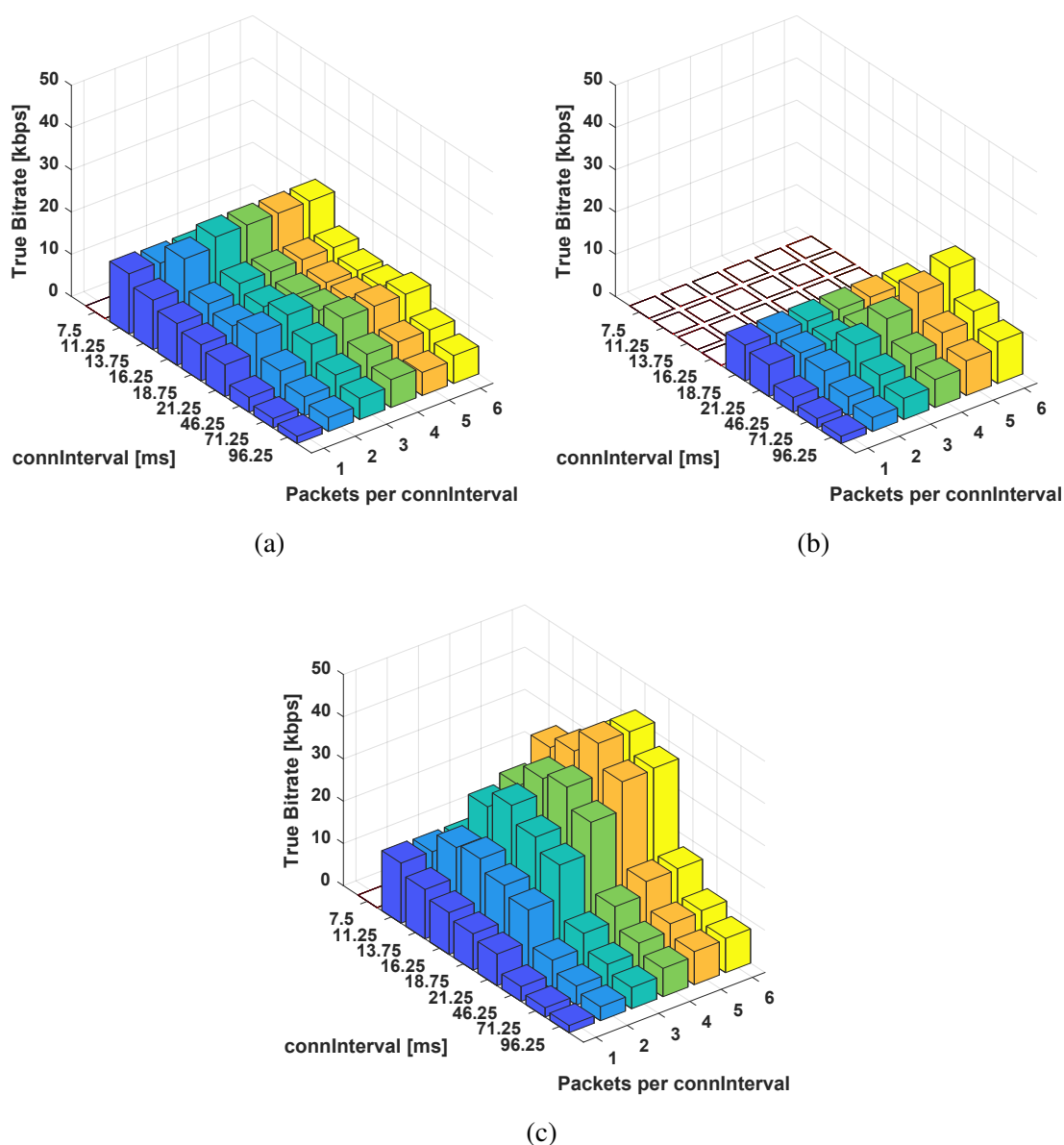


Fig. 2.12 This Figure shows the effective throughput, computed using Equation 2.2. In all three cases, the star network has 5 *slave* nodes of **S1** typology. The value of the throughput is referred to the average throughput of the *peripheral* node. In Fig 2.12a the *master* is **M1**, in Fig 2.12b is **M2**, in Fig 2.12c is **M3**. On the x axis are represented the values of *connInterval*, measured in ms, while on the y axis is represented the number of packets sent per each *connInterval*. White bars indicate cases for what it has not been possible to execute the acquisition, due to protocol limits or its implementation in the specific device.

Of note, in the configuration with a single node (Figure 2.10), **M3** reaches a higher peak of throughput in comparison with other *masters* (*i.e.* up to 88.9 kbps). This was possible both for the lower packet loss that exists in comparison with **M1** and **M2**, and for the possibility to use a *connInterval* of 7.5 ms, which cannot be set in Android devices (Android version 6.0.1 and 7.0). In other cases, when the network has more than 1 *peripheral* node, **M3** generally reaches a lower bitrate in comparison with other types of *masters*. In particular, as can be seen in Figure 2.11 and 2.12, **M2** reaches higher values of throughput with a lower value of packet loss.

Moreover, since for practical use in human motion tracking applications with M-IMU we consider unacceptable those configurations with a packet loss above 1%, we excluded from further throughput analysis those results which do not fulfill this condition.

Hence, we represented in Figure 2.13 and in Table 2.1 the maximum reachable values of bitrate with our setup, with a packet loss below 1%, with respect to different configurations of *master* and *slave*, and also different number of *peripheral* nodes which compose the star network. In Table 2.1 each row represents the number of *peripheral* nodes which compose the star network, while the columns are all the possible combination of *masters* and *slaves*; the values are measured in kbps. In this way, we can define which are the best BLE connection parameters to set up in order to push BLE performance to its limits and obtain the highest values of throughput. The values of bitrate, shown in Figure 2.13 and detailed reported in Table 2.1, are those seen by *master* side. As a matter of facts, they represent the total throughput of the communication. All the parameters related to the values of bitrate obtained are shown in Table 2.2; each row represents the number of *peripheral* nodes which compose the star network, while the columns are all the possible combinations of *masters* and *slaves*. In each cell there are two parameters, the first one is the *connInterval*, measured in ms, while the second is the number of packets sent per each *connInterval*.

Discussion and conclusions

In this part of the work we proposed a method to analyze and characterize throughput performance in general sensor network applications, based on BLE standard. In fact, low power consumption of BLE is well known in the literature [34], but the knowledge about its throughput has never been systematically assessed.

In particular, we analyzed the use of BLE technology for sensor application that requires high throughput, such as motion tracking of human movements. To this aim, we designed and tested BLE-based sensor network with the minimum requirements of connecting 5 M-IMUs (9-axes), acquiring data at 100 Hz (*i.e.* with an effective throughput of 80 kbps at *master* node).

Table 2.1 Values of maximum reachable bitrate, for each network configuration, measured in *kbps*, seen by the *master* side, respecting the condition of packet loss lower than 1%.

	M3	M3	M1	M1	M2	M2
						
	S1	S2	S1	S2	S1	S2
						
1	88.9	88.9	56.9	43.2	57.1	57.1
2	58.6	58.6	104.9	86.4	114.2	114.2
3	68.7	51.2	90.1	88.8	171.3	141.3
4	44.7	82.5	120.1	120.3	159.7	159.7
5	49.4	67.2	71.2	71.1	173.9	173.9

Table 2.2 Connection parameters related to Table 2.1. In each cell, the first number represents the *connInterval* (*ms*), while the second value represents the number of packets sent during each *connInterval*, corresponding to the maximum achievable throughput for that specific combination of *master* and *slave*. All these values respect the condition of percentage of packet loss lower than 1%.

	M3	M3	M1	M1	M2	M2
						
	S1	S2	S1	S2	S1	S2
						
1	$\frac{7.5}{4}$	$\frac{7.5}{4}$	$\frac{11.25}{4}$	$\frac{11.25}{3}$	$\frac{11.25}{4}$	$\frac{11.25}{4}$
2	$\frac{16.25}{3}$	$\frac{16.25}{3}$	$\frac{11.25}{4}$	$\frac{11.25}{3}$	$\frac{11.25}{4}$	$\frac{11.25}{4}$
3	$\frac{21.25}{3}$	$\frac{18.75}{2}$	$\frac{21.25}{4}$	$\frac{16.25}{3}$	$\frac{11.25}{4}$	$\frac{13.75}{4}$
4	$\frac{71.25}{5}$	$\frac{46.25}{6}$	$\frac{21.25}{4}$	$\frac{21.25}{4}$	$\frac{16.25}{4}$	$\frac{16.25}{4}$
5	$\frac{96.25}{6}$	$\frac{71.25}{6}$	$\frac{11.25}{1}$	$\frac{11.25}{1}$	$\frac{18.75}{4}$	$\frac{18.75}{4}$

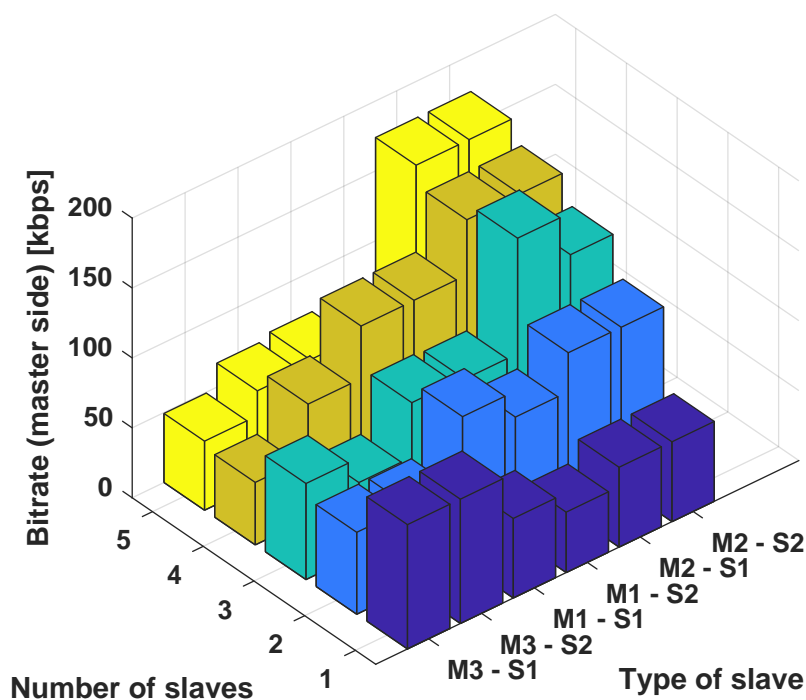


Fig. 2.13 This Figure shows the maximum reachable bitrate, measured in kbps, seen by the *master* side. On the x axis are represented the number of *slaves* which compose the designed star network architecture, while on the y axis there are the possible combinations of *masters* and *slaves* typologies which form the network. The precise corresponding numbers are reported in Table 2.1. All these values of bitrate respect the condition that the percentage of packet loss has to be lower than 1%. To each bar correspond a value of *connInterval* and a number of packets per *connInterval*, reported in Table 2.2.

The most important result obtained is that, with our setup, the BLE-based network can reach peaks of bitrate higher than 170 kbps with 5 peripheral nodes, having a packet loss lower than 1% (see Figure 2.13 and Table 2.1). This result guarantees to use BLE in a lot of sensor applications, including motion tracking, that is the focus of our work. As a matter of facts, a sensor network employing 5 M-IMUs with 9 axes (2 bytes for each axis), acquiring data at 100 Hz, needs an effective throughput of 80 kbps, which is well below the limits verified in our experiments. With the results showed in this work, we can affirm that in principle is possible to use 5 SensorTile (S1), a very small, compact and versatile sensors, in applications which use 5 M-IMUs at a sampling rate higher than 200 Hz, with a packet loss lower than 1%.

Best results in terms of maximum throughput for the network have been obtained with Android devices, in particular **M2** allows to reach the highest value of throughput. Nevertheless, performance of **M2** are very different from **M1**. This result indicates that using smart devices introduces a high variability in terms of results, depending on the hardware embedded, on the version of the operating system and also on the firmware implemented on the BLE IC; nevertheless, using a more efficient smart device permits to obtain higher performance. These differences in performance between **M1** and **M2** can be due to a newer hardware, a different BLE integrated circuit, a more performing firmware or a more recent version of the operating system, which uses new BLE libraries. Anyway, even with an obsolete hardware and Android version (**M1**) we were able to reach peaks of about 120 kbps for the configuration with 4 nodes, allowing to guarantee the minimum requirements for our target application, and about 70 kbps with 5 nodes, a bitrate that supports a sampling frequency of 87.5 Hz, instead of 100 Hz.

As regards the main limitations of the tested sensor networks, it can be seen in Figure 2.9 that Android introduces a limit in the number of M-IMU packets that can be sent per each connection interval. In fact, using **M1** and **M2** as *masters*, we obtain a significant packet loss (*i.e.* higher than 1%) when we try to send a number of packets per *connInterval* higher than 4, regardless of the *connInterval* value itself, also when only a single *slave* is connected to the network. We can assume from our results that Android imposes a *connEvent* that makes the connection unreliable (*i.e.* with a packet loss higher than 1%) with more than 4 packets per *connInterval*; hence, as already said, this limitation is probably due to Android libraries, even though references in official manuals or documentation cannot be found. On the other hand, using **M3** as *master* permits to freely set the *connEvent* parameter, meaning that the maximum number of packets which can be sent per *connInterval* is variable depending on *connEvent* value. Thus, **M3** may overcome the limitations imposed by Android devices (*i.e.* using a *connInterval* lower than 11.25 ms and a maximum number of packets higher than 4), in this way it is possible to push the limit of throughput values to $\simeq 90$ kbps, in a single node network.

If on one side Android, and in particular **M2**, allows to reach the highest value of throughput, on the other side **M3** grants the maximum optimization in term of performance and power consumption.

As a matter of fact, since **M3** can manage the *connEvent*, we have decided to equally divide the *connInterval* between all the devices; in this way, each *peripheral* node can send the same number of packets to the *central* node and, if some packets are lost, all the *slaves* approximately lose the same number of packets. On the other hand, since Android automatically assigns the *connEvent* to each connection, the packet loss is not equally divided

between *peripheral* nodes, and usually the last connected devices lose a higher number of packets.

An important consequence of freely impose *connEvent*, thus the *anchor point*, is the possibility to maximize the efficiency of communication; this allows to optimize BLE performance, especially the power consumption of the BLE IC. In fact, since **M3** has not an upper bound relative to the number of packets that can be sent in each *connInterval*, it allows to use higher time values per *connInterval* respect to **M1** and **M2**; *i.e.* it can maintain a constant throughput using a higher *connInterval*. This characteristic may reduce the current consumption of BLE IC; *e.g.* it can be seen in Figure 2.12 that a throughput of $\simeq 10$ kbps can be obtained both sending 3 packets with a *connInterval* of 46.25 ms and sending 6 packets with a *connInterval* of 96.25 ms. We have estimated the current consumption using a tool provided by STMicroelectronics¹⁴ and we observed that in the first case average absorbed current is 351.9 μA , while in the second case it is 313.3 μA , providing a power saving of $\simeq 11\%$.

Moreover, **M3** *master* typology allows to design a hub, which may also embed more **M3** *central* nodes together, in order to obtain the best performance possible in terms of throughput. In addition to this, even if **M3** does not reach the best performance, it is not dependent on vendors specification, as described here above for **M1** and **M2**, hence, it guarantees more stable results.

With this work we support that Bluetooth Low Energy is strongly competitive with the other technologies existing in the market; as a matter of fact, thanks to its pervasive diffusion between smart devices and its good performance, in particular in term of power consumption and bitrate, it can be used in a wide range of sensor applications that require high throughput.

Moreover, in this work we also present a new methodology of analysis and validation of wireless technology for sensor networks. This is an easy way to understand if a wireless communication technology has satisfying performance, in particular throughput, in order to be applied in a specific sensor network application. As future investigations, it would be interesting to apply the same methodology to others BLE ICs and radios from different producers, in order to point out what are the advantages and disadvantages of each one of them. In addition to this it will be also interesting to evaluate the effect on BLE performance of different parameters and features, such as the rearrangement of the BLE GATT server *characteristics*.

¹⁴STMicroelectronics, "STSW-BNRG001: BlueNRG current consumption estimation tool," DB2288, 2017.

2.2.2 Evaluation of power consumption

System Architecture

Immediately after the evaluation of throughput, our need is to find the exact consumption given by BLE, in order to understand how much low power it is. In fact, it is well known that the main innovative characteristic of BLE, in comparison with Bluetooth Classic and other wireless technologies, is the low power consumption. Indeed, as described in Section 2.1.1, in both *broadcasting* and *connection* mode the Radio Frequency (RF) module turns on to send or receive data and then turns off in order to save energy consumption.

To evaluate the power consumption of a BLE IC it is necessary to measure the average current absorbed during the active phase in each modality of communication. In fact, on the other side, when the radio is in sleep phase, the current consumption is approximately $1 \mu\text{A}$ (with 3 V of reference voltage level)[45].

During the *connection* mode, it is difficult to examine the power consumption because it is strongly variable, depending on several parameters, such as the packet payload, the *connInterval*, the number of *slaves* per *master*, the type of communication (*i.e.* *one-way* or *round-trip*), and so on.

Although some evaluations of power consumption have already been done in other studies [34], or also some companies like STM provide simulators¹⁵ to evaluate and measure the power consumption during all possible states of the BLE IC RF module, we decided to make our own validation on BLE power consumption.

To do this we just designed an experiment with a point-to-point network, *i.e.* a network with only two nodes, a *master* and a *slave*. Usually the *master* node has a battery with a bigger capacity, while the *slave* needs to better manage its power consumption, since its capacity is limited by its physical dimensions. Starting from this observation we just measured the current consumption of the *peripheral* nodes.

In the first experiment we just focused on BLE IC, in particular we used a node composed of a stack of two ST boards, Figure 2.7e, the MCU (NUCLEO-F401¹⁶) and a board with BLE radio and chip (X-NUCLEO-IDB05A1¹⁷), and the sensor expansion board (X-NUCLEO-IKS01A1¹⁸) with MEMS sensors.

¹⁵STMicroelectronics, "BlueNRG Current Consumption Estimation Tool", *STSW-BNRG001*, 2016.

¹⁶STMicroelectronics, "STM32F401xD STM32F401xE: ARM cortex-m4 32B MCU+FPU, 105 DMIPS, 512kB flash/96kB RAM, 11 TIMs, 1 ADC, 11 comm. interfaces," DS10086, 2017.

¹⁷STMicroelectronics, "X-NUCLEO-IDB05A1: Bluetooth low energy expansion board based on the SPBTLERF module for STM32 nucleo," DB2592, 2015.

¹⁸STMicroelectronics, "X-NUCLEO-IKS01A1: Motion MEMS and environmental sensor expansion board for STM32 nucleo," DS10619, 2015.

In the second experiment we used the SensorTile as *slave* node (Figure 2.7d), in order to investigate the total power consumption during a concrete application, *i.e.* the stream of M-IMU data.

In both the experiments we used the multimeter Agilent 34401A¹⁹ to measure the current consumed by the HW implied in the experiment.

Protocol

The protocol designed for the experiment is similar to that one used for throughput measurements in Section 2.2.1. It consists in sending M-IMU data packets from *slaves* to *master* using a BLE *notifiable characteristics*.

The power level of the radio is set to 4.7 dBm.

In each acquisition the value of *connInterval* and the number of packets sent per *connInterval* vary. In our protocol, the possible values of *connInterval* expressed in ms are: 7.5, 11.25, 13.75, 16.25, 18.75, 21.25, 46.25, 71.25, 96.25. This choice has been done since 7.5 ms is the minimum value that can be set in accordance with BLE protocol (Section 2.1.1), and we decided to make it firstly vary with little steps, then higher, in order to investigate a quite wide interval.

For what concerns the number of packets sent per each *connInterval*, we decided to make it vary from 1 to 6. In addition to this, a further limit on M-IMU data transmission depends on the maximum sampling rate of the sensor boards; for our setup, the minimum sampling period to have access to all 9-axes data of M-IMU sensor is 1.8 ms, thus the upper bound of bitrate for each *slave* node is around 89 kbps.

For what concerns the second experiment we just set up a communication with the SensorTile and a *master* node. With a view to a practical application, such as the kinematic reconstruction of human movements, we keep the *connection* parameters fixed and we send M-IMU or quaternion data from the *slave* node. The idea behind this choice is to evaluate both the possibility to implement orientation filters in the MCU or sending raw M-IMU data and implement the filter on the *master* device. The internal filter is a closed library developed by STM²⁰. The sampling frequency of M-IMU sensors is set to 100 Hz.

Consumption Evaluation

Both X-NUCLEO-IDB05A1 and SensorTile cradle expansion board have a jumper on the source voltage line, that means it is possible to remove the jumper and connect the multimeter

¹⁹Agilent, 34401A Digital Multimeter, 2016.

²⁰STMicroelectronics, Getting started with MotionFX sensor fusion library in X-CUBE-MEMS1 expansion for STM32Cube, UM2220, 2018.

to measure the current they consume. In this configuration both devices are powered with a supply of 5 V.

Results and discussion

In Figure 2.14 the results of the experiment are shown. Similarly to the results shown in Section 2.2.1 it is possible to see on the x and y axes the packets per *connInterval* and the *connInterval* itself, while on the z axis it is shown the current consumption measured using the multimeter. It is easy to note how the trend of the values goes proportionally to the throughput value.

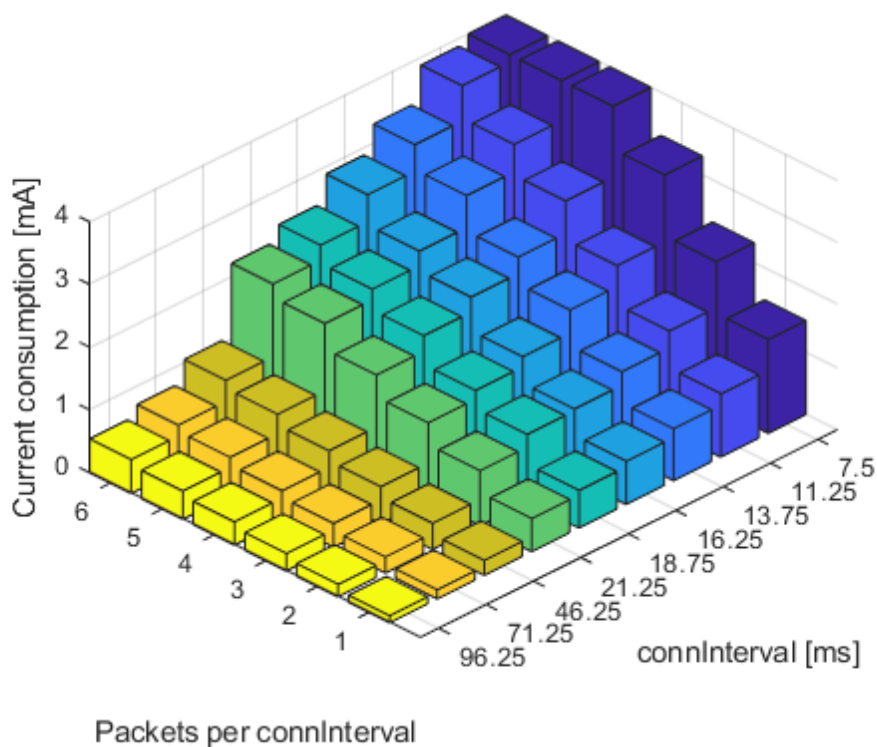


Fig. 2.14 This Figure shows the current consumption of *slave* node, measured in mA. On the x axis are represented the number of packets per *connInterval*, while on the y axis there are all the possible values of *connInterval*.

For what it concerns the second acquisition, we measured the current consumption of SensorTile at 5 V, then we estimated the life of its battery.

For what it concerns this evaluation, the current measured in this experiment is 13.5 mA when the internal filter for sensor fusion is used, and 12.0 mA when we only acquire and stream raw data. Using a very small battery with a capacity of 100 mAh, the life time could

2.2 BLE performance analysis in a sensor network for M-IMU applications

33

be around 7.4 h when the internal filters to get quaternion is used, otherwise the battery life may be higher than 8.3 h (Table 2.3).

Table 2.3 Current consumption of SensorTile and battery life. The first column represents the consumption when the internal STM filter is used to obtain quaternions, the second column is referred to the acquisition of raw M-IMU data only.

	Internal Filter	Raw M-IMU data
Current consumption	13.5 mA	12.0 mA
Battery life (100 mAh)	7.4 h	8.3 h

Of note that the FW used by the SensorTile may be optimized most, we just wrote a code appropriate and effective for the application.

Reading these results it is clear that BLE gives the possibility to let an high throughput application last for a long time. This is very important thinking to a use case of telemedicine or continuous monitoring of a subject.

In particular, the possibility of carefully modify its connection parameters gives the opportunity to set it up in an optimal way, depending on the specific application.

This two studies we proposed, the one related to throughput and the other to power consumption, pave the way for the designing of standard protocols which may help to set up networks parameters in order to obtain the lower power consumption with given specifications, such as the minimum throughput needed.

Tesi di dottorato in Bioingegneria e bioscienze, di Jacopo Tosi,
discussa presso l'Università Campus Bio-Medico di Roma in data 28/05/2019.
La disseminazione e la riproduzione di questo documento sono consentite per scopi di didattica e ricerca,
a condizione che ne venga citata la fonte.

Chapter 3

Performance evaluation of magneto-inertial motion units and sensor fusion algorithms

Citations:

- [C.IV] **Jacopo Tosi**, Fabrizio Taffoni, Asif Hussain, Domenico Campolo and Domenico Formica. Methodology for the Evaluation of Magneto-Inertial Orientation Filters in SO(3). In *2019 IEEE International Workshop on Metrology for Industry 4.0 and IoT*, in press. IEEE, 6 2019.

This section of the PhD project aims to describe and assess the sensing part of our system. In fact, as the first chapter analyzes the wireless communication technology, *i.e.* Bluetooth Low Energy, this chapter is focused on magneto-inertial measurement units (M-IMUs) which represent main sensing elements that has been used in the presented research and the principal source of information applied in the implemented algorithms.

The purpose of this chapter is first of all to provide a comprehensive overview of these devices, taking into account their main aspects, such as functioning, configuration, calibration and sensor modeling. Secondly, it describes how to use sensor fusion algorithms which exploit M-IMUs to obtain orientation of a body in the space. Finally, in the last section of this chapter, we propose a standard methodology to tune sensor fusion filters and evaluate their performance, in order to choose the solution which provides the lowest error, for the specific application of interest.

3.1 Background on Magneto-Inertial Measurement Units: basic features and functioning

In the last years, a new generation of inertial measurement units (IMUs) based on micro-electro-mechanical systems (MEMS) technology has given a new surge to motion tracking research. These devices are cost-effective and can be successfully used for accurate, non-invasive and portable motion tracking. The big interest in these devices is mainly motivated by the fact that they overcome many issues raised by optical systems and mechanical trackers. IMUs indeed do not suffer from occlusions and have theoretically unlimited workspace compared to optical motion tracking systems; moreover, despite the lower accuracy of IMUs with respect to mechanical trackers, they are much more affordable and far less intrusive.

In recent years, IMUs are often used to track human motion, thus becoming a new enabling technology for several applications which include localization, human-robot interaction, rehabilitation and ergonomics [46], becoming an important alternative to stereophotogrammetry based systems (ranked as the gold standard). This spread is also witnessed by the high number of companies that are developing IMUs sensors and putting them in the market: *e.g.* Xsens (Xsens Technologies B.V., Enschede, The Netherlands), Opal (APDM Inc., Portland, USA), Trigno (Delsys Inc., Salford, Greater Manchester, UK), Consensys IMU (Shimmer, Dublin, Ireland) and 3-Space (Yost Labs, Portsmouth, Ohio).

Surprisingly, less attention has been dedicated to rigorously assessing the accuracy in estimating orientation attainable with a wearable M-IMU during typical motion conditions [3]. Technical specification of commercial systems reported by vendors are presented with caveats and are poorly documented, *e.g.* the dynamic accuracy is reported without detailing the testing setup, the amplitude and the bandwidth of testing movements. The main contribution of this part of the work is in providing a systematic characterization of the accuracy in orientation measuring under controlled and repeatable conditions and using state of the art sensor fusion algorithms.

IMUs are typically composed of accelerometers and gyroscopes. Since the use of IMUs to reconstruct the orientation is based on integration of sensors' signals over time, but also both gyroscopes and accelerometers suffer from time varying biases and noises, the measurements often contain drift. To reduce this drift in the estimation of the pose, especially to correct the drift relative to rotations around gravity direction (*heading*), they are often equipped with magnetometers: in this case the sensor units are called Magneto-Inertial Measurement Units (M-IMUs), or MARG (*i.e.* Magnetic, Angular Rate and Gravity), or also AHRS (Attitude and Heading Reference Systems). When a sensor unit has tri-axial gyroscopes and accelerometers, since they have 6 degree of freedom (DOF), they are also called 6-axis IMUs.

3.1 Background on Magneto-Inertial Measurement Units: basic features and functioning **37**

When the unit embeds also a tri-axial magnetometer, it is typically called 9-axes sensor unit (*i.e.* a unit with 9 DOF), and it can be used to estimate the 3D orientation of a body in the space (see in Appendix A).

In the next sections we are going to briefly describe the functioning of these three typologies of sensors. In addition to this, in the next sections we are also going to present some procedures to calibrate M-IMU sensors. In fact, the availability of low cost MEMS M-IMU and the contrast with expensive traditional calibration methodologies requiring access to sophisticated tests and calibration equipment, have pushed the research towards more convenient procedures [47].

The mathematical framework used for dealing with inertial tracking systems are described in Appendix B.

3.1.1 Gyroscope

The gyroscopes measure angular velocity with respect to the sensor moving reference frame \mathcal{S} , by taking advantage of physical laws that produce predictable effects under rotation. A rotating frame is not an inertial frame, and thus many physical systems will appear to behave in an apparently *non-Newtonian* manner. By measuring these deviations from what would be expected in a Newtonian frame the underlying self-rotation can be extracted.

Almost all MEMS gyroscopes are based on vibrating mechanical elements to sense rotation. Vibratory gyroscopes rely on the transfer of energy between vibratory modes based on Coriolis acceleration \mathbf{a} of an object moving in a straight line with linear velocity \mathbf{v} , in a frame rotating at rate $\mathbf{\Omega}$, described by the equation

$$\mathbf{a} = 2\mathbf{v} \times \mathbf{\Omega} \quad (3.1)$$

Early MEMS gyroscopes utilize vibrating quartz crystals to generate the necessary linear motion. More recent designs have replaced the vibrating quartz crystal with silicon-based vibrators [48]. Vibrating mass gyroscopes are small in dimension, but have a higher noise level and consume more than the other sensors of an M-IMU.

A measured gyroscope signal ${}^s\boldsymbol{\omega}_t^m$ represented in the sensor frame \mathcal{S} at time t can be expressed as

$${}^s\boldsymbol{\omega}_t^m = {}^s\boldsymbol{\omega}_t + \mathbf{b}_{\omega,t} + \mathbf{e}_{\omega,t} \quad (3.2)$$

where ${}^s\boldsymbol{\omega}_t$ is the true angular velocity after compensation, $\mathbf{b}_{\omega,t}$ is the bias caused by low-frequency offset fluctuations and the remaining error $\mathbf{e}_{\omega,t}$ is assumed to be the zero-mean white noise [49] [50] [51].

38 Performance evaluation of magneto-inertial motion units and sensor fusion algorithms

The bias $\mathbf{b}_{\omega,t}$ determines the drift when integrating the gyroscope signal and can be calibrated and compensated with a *zero attitude update*. It results from the contribution of different terms:

$$\mathbf{b}_{\omega,t} = \mathbf{b}_{FB} + \mathbf{b}_{BS} + \mathbf{b}_{BR} \quad (3.3)$$

The fixed bias term (\mathbf{b}_{FB}) represents the displacement from zero of the output when the input is null and it is often modelled as a function of temperature. The *bias repeatability* parameter (\mathbf{b}_{BR}) is a random constant that varies for each powerup of the IMU. This is due to a number of effects, including a change in the physical properties of the IMU and initial conditions of the signal processing. Further, the bias of a MEMS gyroscopes has a stability component, termed *bias stability* (\mathbf{b}_{BS}), which will vary during in-run usage due to flicker noise in the electronics, temperature, time and/or mechanical stress on the system. This behaviour is usually modeled as random walk noise. Gyroscope datasheets usually reports how stable the bias is over a certain specified period of time. This value is typically expressed in units of deg/s or deg/hr.

To perform the gyroscope calibration the sensor must be stationary in order to acquire the gyro bias as the mean of the signal and it should be removed from the sensor's signal [52] [53].

Ambient temperature affects gyro signal with a significant bias drift. It comes especially when gyros are powered up, as a result of device self-heating; after few minutes of warm-up they reach a thermal stabilization, hence it is usually preferred to start calibrating and using the gyroscope when the stabilization has been reached.

3.1.2 Accelerometer

Accelerometers can be used to measure external inertial forces acting on the body, which are directly related to the acceleration of the body itself. There are several typologies of these sensors: mechanical accelerometers are essentially a spring-mass-damper, which estimate the force by measuring the displacement. Knowing the values of the mass, damping and spring coefficients; another example is given by piezoelectric accelerometers where a small mass is positioned so that it is only supported by the crystal; and as an inertial force acts on the mass, this induces a movement of the crystal which can be measured by a change of voltage. As a result, the mass moves relatively to the sensor housing in the opposite direction with respect to the direction of the movement. To estimate the orientation of the body, as will be explained in Section 3.2.1, the accelerometers are used to measure the gravity in the

3.1 Background on Magneto-Inertial Measurement Units: basic features and functioning **39**

sensor frame \mathcal{S} [48]. Accelerometer calibration is not necessary for sensor fusion except for applications demanding very high orientation precision.

A measured accelerometer signal ${}^s\mathbf{a}_t^m$ can be presented, similarly to gyroscopes, as

$${}^s\mathbf{a}_t^m = {}^s\mathbf{a}_t + \mathbf{b}_{a,t} + \mathbf{e}_{a,t} \quad (3.4)$$

$${}^s\mathbf{a}_t = {}^s\mathbf{a}_{b,t} + {}^s\mathbf{g}_t \quad (3.5)$$

where ${}^s\mathbf{a}_t$ is the linear acceleration after error compensation. ${}^s\mathbf{a}_{b,t}$ is the measured acceleration of the body after gravity compensation, that in M-IMU systems for attitude estimation is usually supposed to be negligible compared to the gravity acceleration; that is true only if linear movements are *quasi-static* [54]. $\mathbf{b}_{a,t}$ is the bias caused by low-frequency offset. Actually, the bias represents the displacement from zero on the accelerometer output when the sensed specific force is null; the magnitude of the bias term is independent of any motion to which the accelerometer may be subjected and it is commonly expressed as a fraction of the full scale of the accelerometer itself. Actually, it may be determined by the drift obtained from the double integrating the accelerometer signal and also from a non proper gravity compensation. The remaining error $\mathbf{e}_{a,t}$ is assumed to be the zero-mean white noise. Knowing that, it also is important to perform an accelerometer calibration to remove this bias.

In the inertial frame \mathcal{I} , gravity is a constant vector represented in the vertical direction, while if expressed in sensor frame \mathcal{S} , it depends on the orientation of the M-IMU with respect to gravity direction. That means the inclination can be estimated when the free acceleration is known (or when the sensor unit is still), or alternatively, the free acceleration can be calculated from the accelerometer signal, when the orientation is known (and the gravity removed) [49] [50] [51].

When the accelerometers are used to estimate the attitude of the body, the linear accelerations due to the movements of the body are considered as a disturbance in the accelerometer signals. Most of the methods for attitude estimation assume the body acceleration being negligible, thus modeling the accelerometer signal as a noisy measurement of acceleration due to gravity; other methods compute body acceleration and then remove it from the accelerometer signal.

Sensors are just transducers and provide an output voltage v that, in the best case scenario, is proportional to variation of the measurand m . In practical terms: $v = km + v_o$, where k and v_o respectively represent the linear gain and the offset value. Parameters v_o and k are easily determined when measurand assumes at least two known values. In the case of

40 Performance evaluation of magneto-inertial motion units and sensor fusion algorithms

accelerometers, the measurand can easily assume values such as 0 , $+g$ and $-g$ by simply aligning the sensor's axes respectively orthogonally, parallel and anti-parallel with the vertical direction [55].

Another procedure that can be used to calibrate accelerometers is the same proposed for magnetometers, and it is detailed in the Section 3.1.4.

3.1.3 Magnetometer

Magnetometers measure the geomagnetic flux (\mathbf{B}), and in typical M-IMU applications are used to detect the geomagnetic field (\mathbf{b}) when no other magnetic source is present. Micro-machined magnetometers included in a M-IMU are based on the physical principle of anisotropic magnetoresistance (AMR) and make use of a common material, the permalloy, to act as magnetometer. The electrical resistance of this specific alloy depends on the angle between the metallization and the direction of current flow which, in turn, depends on the external magnetic field's magnitude and direction. In MEMS magnetometers, multiple arrays of sensing elements are organized in a Wheatstone bridge configuration.

A measured magnetometer signal ${}^s\mathbf{m}_t^m$ is modeled as

$${}^s\mathbf{m}_t^m = {}^s\mathbf{m}_t + \mathbf{d}_{m,t} + \mathbf{b}_{m,t} + \mathbf{e}_{m,t} \quad (3.6)$$

where ${}^s\mathbf{m}_t$ is the earth's magnetic field expressed in sensor frame, $\mathbf{d}_{m,t}$ is due to another magnetic source (usually treated as disturbance), $\mathbf{b}_{m,t}$ is the magnetic bias and $\mathbf{e}_{m,t}$ is the zero-mean noise.

In the inertial frame \mathbf{I} (Appendix B) and in a specific point of the globe, the magnetic field is constant and composed of two main components: an horizontal one b_{\parallel} which points toward the magnetic North and a vertical component b_{\perp} which depends on the latitude [49] [56].

Nevertheless, magnetometers also measure a distortion of the magnetic field from the environment which can influence the acquisition. These disturbances are often divided in two types and called *hard iron* and *soft iron* effects.

Hard iron distortions (*i.e.* $\mathbf{b}_{m,t}$) arise from permanent magnets and magnetized substances in a fixed location relative to the magnetic sensors. Those disturbances can be compensated by calibration methods associated with specified rotation of the magnetometers in order to estimate the magnetic surrounding space [57] [58] [59]. The methodology able to compensate this type of distortions is described in Section 3.1.4.

3.1 Background on Magneto-Inertial Measurement Units: basic features and functioning **41**

Soft iron distortions arise from the interaction of the earth's magnetic field with any magnetically soft material not permanent in the environment, which deviates its magnetic field lines: in this case compensation is more difficult.

3.1.4 Accelerometer and magnetometer calibration

For what concerns accelerometer and magnetometer calibration, it is possible to compensate the constant distortions existing in the measured fields. For what it concerns accelerometers, it is possible to compensate the gravity field, while for the magnetometer it is possible to avoid hard iron distortions.

Campolo et al. [56], but also Merayo et al. [60], proposed a novel procedure for calibration, which can be used for both accelerometers and magnetometers. We already explained in Section 3.1.2 that accelerometer calibration is only necessary for high orientation precision, hence we are going to calibrate only for magnetic signals with this algorithm.

The following definitions are referred to magnetometer calibrations, but it is possible to transpose to accelerometers without any change.

In terms of sensor output voltages (v_x, v_y, v_z), considering different offset voltages (v_{ox}, v_{oy}, v_{oz}) and different linear gains (k_x, k_y, k_z) for each axis, the shape of several acquisitions of magnetic field \mathbf{b} described in the Earth frame \mathbf{E} as a sphere centered in the origin and of radius

$$b = \sqrt{b_{\parallel}^2 + b_{\perp}^2} \quad (3.7)$$

becomes in the sensor frame \mathbf{S} an off-centered ellipsoid

$$\left(\frac{v_x - v_{ox}}{k_x}\right)^2 + \left(\frac{v_y - v_{oy}}{k_y}\right)^2 + \left(\frac{v_z - v_{oz}}{k_z}\right)^2 = 1 \quad (3.8)$$

Such an ellipsoid is uniquely identified by the six parameters ($v_{ox}, v_{oy}, v_{oz}, bk_x, bk_y, bk_z$), the first three identify the center of the ellipsoid, while the remaining three identify the semi-axis length.

At least six independent equations are needed in order to determine the unknown parameters. Because of the errors (*i.e.* measurement noise) affecting the sensor read outputs, fitting methods with a larger number of measurements can be deployed to obtain an estimate of the six unknown parameters which is less sensitive to measurement noise. As discussed by [61], the fitting problem can be robustly solved either via linear [56], [62] or non-linear optimization [63], [64]. Maximum Likelihood (ML) formulation are also found in the literature [58], [65].

42 Performance evaluation of magneto-inertial motion units and sensor fusion algorithms

To acquire this large number of measurements, the calibration routine of magnetometers consists in rotating the sensor in order to point it through all possible directions so that we can operate on a set of data which spans as large as possible the 3D space. While performing this movement, it is important to keep the device clear of other magnetic objects (*e.g.* cell phones, computers and other steel objects). In addition to this, keeping into account all the possible variations of the magnetic field due to possible artifact, is strongly recommended to perform the calibration in the whole measurement volume of the targeted application.

An example of accelerometer acquisition and calibration is showed in Figure 3.1, where the shape on the left is the ellipsoid made by raw data, while the sphere on the right is the one obtained by data computed after calibration.

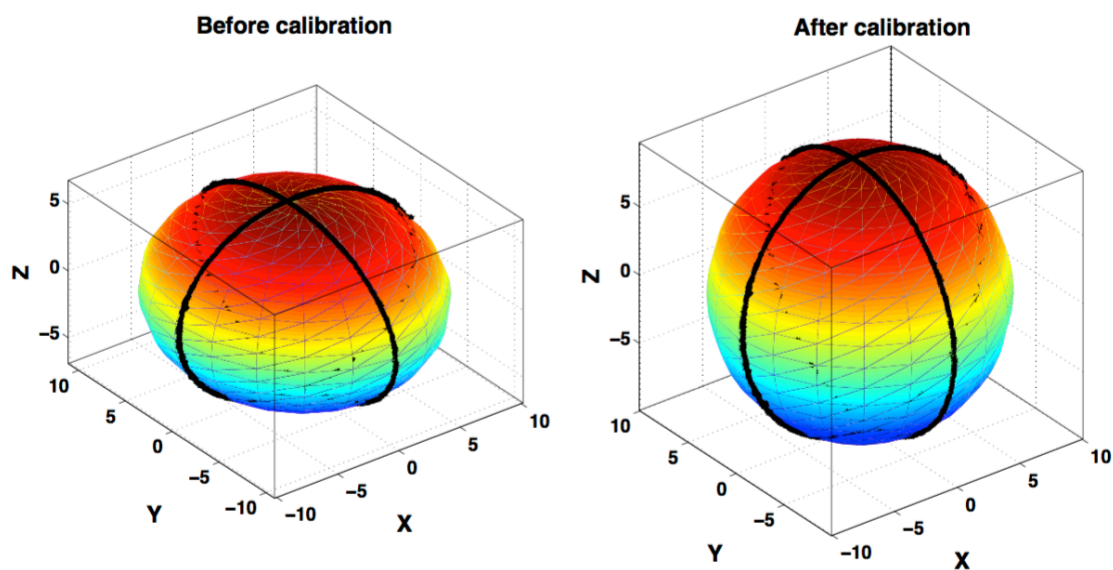


Fig. 3.1 The Figure reports the typical outcome of a sensor calibration procedure (specifically the least-squares method described in [56]): uncalibrated accelerometer measurement (left) are mapped on an ellipsoid manifold. Through the estimation of the parameters describing this ellipsoid, measurements can be corrected and calibrated. After the calibration process, measurements are mapped on a sphere (right).

To calibrate accelerometers it is important to slowly rotate the sensor in order to avoid additional accelerations due to the movement itself, while for what it may concern magnetometers, there are not specifically constraints in the execution.

3.2 Validation of sensor fusion algorithms for attitude estimation with M-IMUs

Signals gathered from accelerometers, gyroscopes, magnetometers and other sensors need suitable sensor fusion techniques to derive useful information about the orientation of the body.

Combining together this three different kind of sensors described above, it is possible to get the orientation of the rigid body attached to the M-IMU. In fact, integrating gyroscopes it can be obtained the relative rotation, while accelerometers and magnetometers give information of how the sensor is oriented with respect to a fixed frame, that is composed of the geomagnetic field and gravity vector, described in Appendix B.

In this thesis work we analyzed some filters for sensor fusion which return as output the orientation of the rigid body whom the sensor is attached to. In this Section we are going to describe all these filters that we used in order to understand pros and cons of each one. In fact, our scope is to determine which of those give the best result depending on the application they are used.

All these filters fuse data from several sensors and compensate for limitations of single sensors. For instance, gyroscope data can drift and this impacts the orientation estimation; this issue can be fixed by using the magnetometer and accelerometers to provide absolute orientation information. Similarly, the magnetometer does not have a very high bandwidth and suffers from magnetic disturbance, while accelerometers record also linear acceleration during dynamic phases, but these weaknesses can be compensated with a gyroscope.

IMU 6-axes sensor fusion uses the accelerometer and gyroscope data only. It has lower computational requirements, but does not provide information about the device absolute orientation around the yaw axes, in fact they are typically used in applications with planar movement on the vertical plane, such as gait analysis. This type of sensor fusion is suitable for fast movements (*e.g.* for gaming) and when absolute orientation is not necessary.

9-axes sensor fusion uses data from the accelerometer, gyroscope and magnetometer and provides absolute orientation in 3D space include *heading* (*i.e.* the magnetic North direction).

All these filters give back as output the orientation of the rigid body in the space; some of the possible ways to represent it are describe in Appendix A and will be used in the following part of this section to describe the sensor fusion algorithms that are used to obtain orientation data from M-IMU.

44 Performance evaluation of magneto-inertial motion units and sensor fusion algorithms

3.2.1 Sensor fusion filters: state of the art

In this section we are going to describe several possible sensor fusion filters used to reconstruct the orientation from M-IMUs.

The goal of the orientation estimation filter is to provide an estimate of the rotation between the moving body coordinate frame of the sensor frame \mathbf{S} and a global fixed frame (often the inertial reference frame \mathbf{I}), described in Appendix B.

The easiest way to obtain the orientation of the object is given by gyroscopes integration, but it suffers from a bias integration which typically yields to an error increasing indefinitely over time; to overcome this issue, two main classes of filters are adopted for sensor fusion algorithms: Kalman filters (KF) and complementary filters (CF).

Gyroscope Integration

Gyroscope integration provides an estimate of the relative rotation from an initial known reference frame. As the angular velocity measured by the gyroscopes is directly integrated, this method provides smooth estimates even during rapid movement.

Gyroscope integration can be implemented very efficiently using the difference Equation 3.9 [66],

$$\hat{q}_t = \hat{q}_{t-1} + \frac{1}{2} [\hat{q}_{t-1} \otimes [(0, \hat{\omega}) - \beta]] \cdot \Delta t \quad (3.9)$$

where \hat{q} is the estimated orientation, in quaternion form; Δt is the sample period; $\hat{\omega}$ is the angular velocity vector in radians per second; and the operator \otimes , is the quaternion multiplication operator (see Equation A.13 in Appendix A.4.1). After each update, the estimated quaternion should be re-normalized to minimize the effects of rounding errors in limited precision implementations.

The only one parameter which can be tune in this filter is β that is the gyroscope bias and it is used to compensate the drift given by integration. This parameter is subtracted to the acquired value of gyroscopes.

The integration process has two significant disadvantages: firstly, any bias in $\hat{\omega}$ will result in an increasing cumulative error in the estimated orientation; secondly, the initial orientation of the device must be known. In addition to this, it gives an imprecise orientation when movements are in a low frequency bandwidth.

To solve this issue, vector observation is inserted; it provides an estimate of the orientation, relative to a fixed world frame. By measuring the position of two, or more, vectors (*e.g.* gravity and magnetic field) in the body frame \mathbf{B} of a device and comparing these with the known position of the vectors in the fixed frame \mathbf{L} , the rotation between the two frames can be

calculated. This operation also comes to the aid of getting the orientation in the low frequency bandwidth. Example of filters which overcomes these limits are the Complementary and Kalman filters.

Kalman Filter

One of the most widespread sensor fusion technique is the Kalman Filter [67]; it uses a stochastic approach to account for noise statistics. Kalman filter needs two different inputs which represents the same kind of information: the first should represent a possible prediction of the desired output, obtained only using linear calculations; the second value should represent a more reliable value which may be used to correct the first one.

KFs work in the time domain focusing on the noise corrupting the signal and leads to optimally when the noise is Gaussian. Young [68] made a comparison between several typologies of filters and explains how Kalman filter uses the knowledge of the expected dynamics of a system to predicate future system states given the current state and a set of control input. KF is formally described by

$$\vec{x}_{k+1} = A\vec{x}_k + B\vec{u}_k + \vec{w}_k \quad (3.10)$$

where \vec{x} is the state vector, A is a state transition matrix relating the previous state to the next state, \vec{u} is a control input vector, B is a matrix relating control inputs to system states and \vec{w} is a process noise vector with covariance matrix Q_k representing uncertainty in the system dynamics.

Then a set of indirect measurements of the state are taken into account

$$\vec{y}_k = C\vec{x}_k + \vec{v}_k \quad (3.11)$$

where C is an observation matrix relating system state to observed measurements and \vec{v} is a measurement noise vector with covariance matrix R_k .

The KF can be defined as [67]

$$\hat{x}_{k+1} = (A\hat{x}_k + B\vec{u}_k) + K_k(\vec{y}_{k+1} - C\hat{x}_k) \quad (3.12)$$

where K_k is the Kalman gain defined as

$$K_k = AP_kC^T(CP_kC^T + R_k)^{-1} \quad (3.13)$$

$$\vec{P}_{k+1} = AP_kA^T + Q_k + AP_kC^TR_k^{-1}CP_kA^T \quad (3.14)$$

46 Performance evaluation of magneto-inertial motion units and sensor fusion algorithms

where K is the Kalman gain and P is the estimation error covariance matrix. The KF can be thought as a predictor-correct filter with the first term in Equation 3.12 is the prediction, according to the process model, and the second term the correction, based on indirect measurements of the system state.

An intuitive understanding of the filter operation can be gathered by examining the Kalman gain equation, *i.e.* Equation 3.13.

$$\lim_{R_k \rightarrow 0} K_k = AC^{-1} \quad \lim_{P_k \rightarrow 0} K_k = 0 \quad (3.15)$$

Using Equation 3.15 into the Equation 3.12 can be seen that as the measurement error R_k decreases, a greater weight is given to the correction; while as the estimation error P_k decreases, a greater weight is given to the prediction.

Kalman filters were originally developed for linear systems [50] and then extended to cope with non-linearities via linearization techniques: the Extended Kalman Filter (EKF) is the most immediate solution that has been adopted to use the KF approach with nonlinearities [69].

However, the Kalman filter implementation would impose an unacceptable computational burden due to so many recursive formulas which need to be calculated to make the mean square error least [70]. Furthermore, different kinds of Kalman filter are needed for different state vectors, dynamic models and measurement models, and with the increase of accuracy of the result, the larger dimension state vectors are needed, which will lead to higher computation cost [49]. In addition to this, the linear regression iterations, fundamental to the Kalman process, demand sampling rates which can far exceed the subject bandwidth (512 Hz - 30 kHz), in case we use the KF to acquire human movements [71]. Nevertheless, there are some examples of sensor fusion algorithm which use KF with optimal results, *e.g.* STMicroelectronics digital filter¹ and Xsens Kalman Filter [72].

In our work we use a closed library freely provided by STMicroelectronics² which uses a digital filter based on the Kalman theory to fuse M-IMU data to get quaternions. In this filter gyroscope calibration is handled automatically by the library itself by continuously compensating the zero-rate offset effect.

Although Kalman filters can be extended to nonlinear cases, they fail in capturing the nonlinear structure of the configuration space of problems involving rotation of a rigid body;

¹STMicroelectronics, "Getting started with MotionFX sensor fusion library in X-CUBE-MEMS1 expansion for STM32Cube", *UM2220*, 2018.

²STMicroelectronics, "Getting started with MotionFX sensor fusion library in X-CUBE-MEMS1 expansion for STM32Cube", *UM2220*, 2018.

and most importantly, they can run into instabilities, which can be better analyzed using complementary filters.

Complementary Filter

Complementary filters exploit the different frequency spectra of gyroscope, accelerometer and magnetometer signals. Basically, many of the methods that exploit the CF approach apply the following steps: the accelerometer signal is used to estimate the acceleration due to gravity in sensor frame \mathcal{S} ; this first estimate, combined with the magnetometer signal, are then used to obtain a low frequency estimate of the sensor's attitude and heading; at the same time an estimate of the dynamic component of the orientation is computed from the integration of the gyroscope measurements at high frequency. These two estimates are then fused together by the complementary filter.

In other words, the CF handle both low-pass and high-pass filter simultaneously [73]. The high-pass filter takes into account the gyroscopes in order to keep the dynamic characteristic of this sensors, avoiding at the same time the drift obtained after the integration. The low pass filter relies on data from magnetometer and accelerometers signal which for quasi-static movements are strongly related to the gravitational and magnetic static fields. The idea of complementary filter is shown in Figure 3.2a where signals x and y are respectively noisy measurements in high frequency and low frequency of signal z ; \tilde{z} is the estimated output of z operated by complementary filter. Then, the filter $H(s)$ performs a high pass filter to filter out the low frequency noise in a x signal. Similarly, the filter $[1 - H(s)]$ is a low pass filter to filter out the high frequency noise in a y signal.

An alternate version of complementary filter is shown in Figure 3.2b, where the input signal given to the filter $H(s)$ is the difference of the two measured signals, where η_1 and η_2 is the signal noise,

$$x - y = (z + \eta_1) - (z + \eta_2) = \eta_1 - \eta_2 \quad (3.16)$$

hence, the filter $H(s)$ filters out only the noise of the two signals ($\eta_1 - \eta_2$).

A typical application of complementary filter is to estimate the rotation of a rigid body by combining measurement of angle θ_{am} from accelerometer and magnetometer, and the same angle θ_g obtained from the integration of angular velocity ω_g , measured from gyroscopes (Figure 3.3).

Let $\tilde{\theta}$ be the estimate of angle θ . The angular velocity measurement ω_g is integrated ($\frac{1}{s}$) to produce the angle signal θ_g . The integration attenuates the high frequency in the angle

48 Performance evaluation of magneto-inertial motion units and sensor fusion algorithms

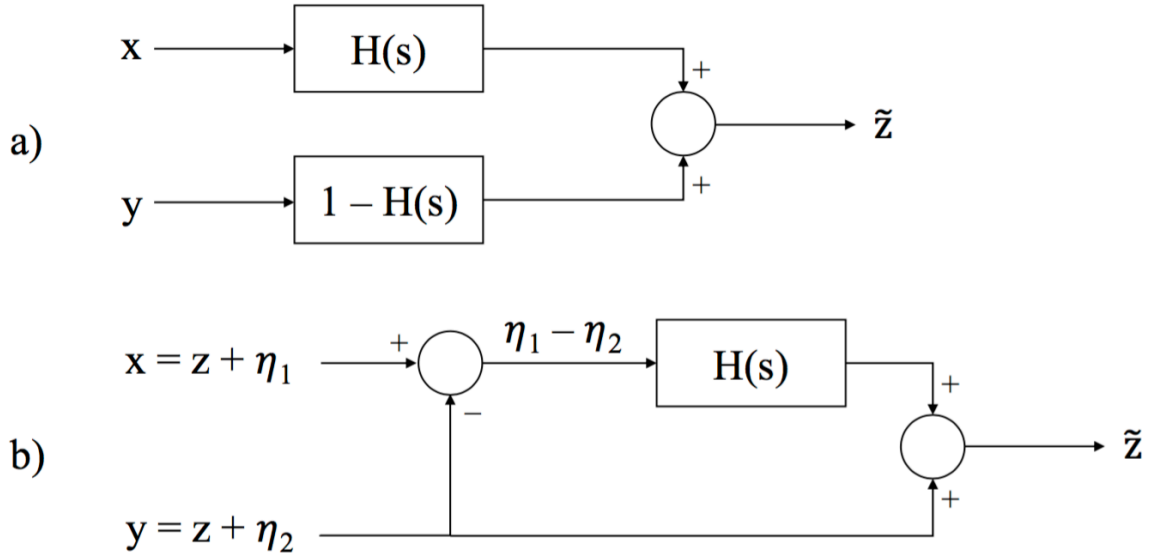


Fig. 3.2 a) The standard complementary filter: $H(s)$ is a high pass (or low pass) filter, $1 - H(s)$ is a low pass (or high pass) filter. b) Alternate version of complementary filter which filter only the noise.

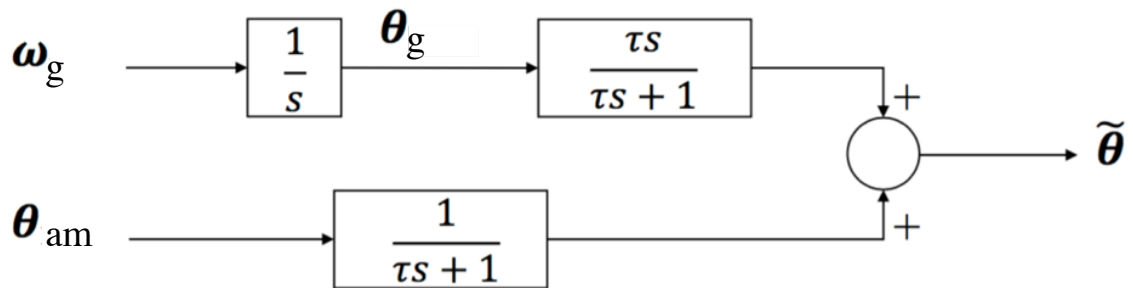


Fig. 3.3 A typical complementary filter used to get the orientation from an M-IMU. The low passed signal comes from gyroscopes (ω_g), while the high passed signal derives from accelerometers and magnetometers (θ_{am}).

measurement, hence, the θ_g is filtered by the high pass filter, whereas the noise in the θ_{am} is filtered by the low pass filter.

The transfer function is

$$\tilde{\theta} = \frac{1}{1 + \tau s} \theta_{am} + \frac{\tau s}{1 + \tau s} \frac{1}{s} \omega_g = \frac{\theta_{am} + \tau \omega_g}{1 + \tau s} \quad (3.17)$$

where the inverse of τ represents the cutoff angular frequency of the filter.

Mahony et al. [51] presents an idea to correct the input of the complementary filter, described in the special orthogonal group $SO(3)$ (Appendix A.5), by a correction provided

by proportional controller. To implement the CF it is necessary to map the angular velocity Ω , measured in the body moving reference frame \mathcal{S} , into the inertial fixed reference frame \mathcal{I} . To do that, a rotation matrix R between the two reference frames needs to be estimated.

In general a CF described in $SO(3)$ is schematically represented in Figure 3.4, where the \hat{R}^T operation is an inverse operation on $SO(3)$ and is equivalent to a "-1" operation for a linear complementary filter. The " $\hat{R}^T R$ " operation is equivalent to generating the error existing between the measured rotation matrix and the estimated one. The two operations $\mathbb{P}_a(\tilde{R})$ and $(R\Omega)_\times$ are maps from error space and velocity space into the tangent space of $SO(3)$. The kinematic model ($\dot{\hat{R}} = A\hat{R}$) (Appendix A.5) is the Lie-group equivalent of a first order integrator.

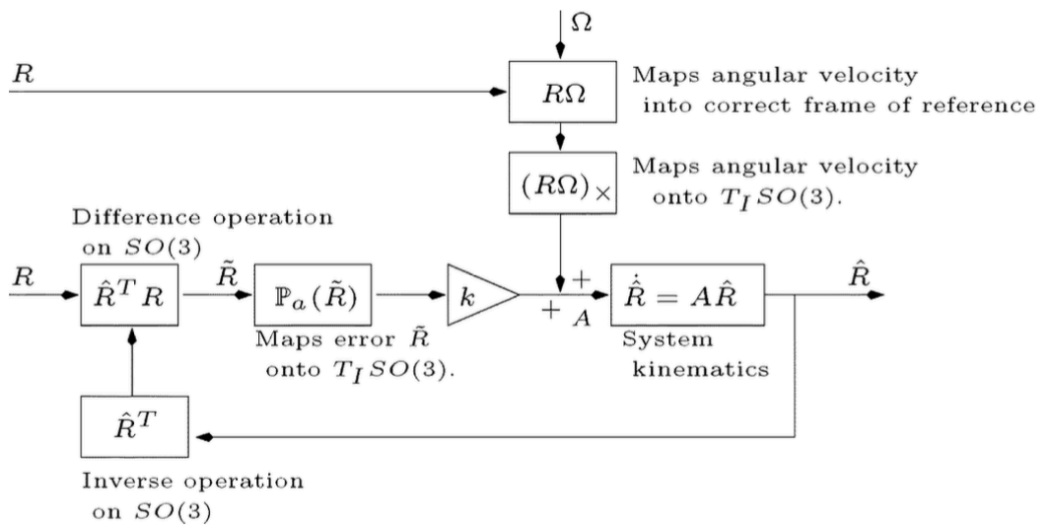


Fig. 3.4 Block diagram of the generic Mahony complementary filter in $SO(3)$ [51].

In the following equations is assumed that a reconstructed rotation R_y and a biased measure of angular velocity Ω_y are available

$$R_y \approx R, \quad \text{valid for low frequencies} \quad (3.18)$$

$$\Omega_y \approx \Omega, \quad \text{for constant bias } b \quad (3.19)$$

In detail, the authors considered two different possibilities:

- Direct Complementary Filter: the estimated attitude R_y is used to map the velocity into the inertial frame \mathcal{I}

50 Performance evaluation of magneto-inertial motion units and sensor fusion algorithms

$$\dot{\hat{R}} = (R_y \Omega_y + k_p \hat{R} \omega) \times \hat{R} \quad (3.20)$$

A block diagram of this filter design is shown in Figure 3.5. The approach has the advantage that it does not introduce an additional feedback loop in the filter dynamics; however, high frequency noise in the reconstructed attitude R_y will enter into the feed-forward term of the filter.

- Passive Complementary Filter: the filtered attitude \hat{R} is used in the predictive velocity term

$$\dot{\hat{R}} = (\hat{R} \Omega_y + k_p \hat{R} \omega) \times \hat{R} \quad (3.21)$$

A block diagram of this architecture is shown in Figure 3.6. The advantage lies in avoiding corrupting the predictive angular velocity term with the noise in the reconstructed pose. However, the approach introduce a secondary feedback loop in the filter and stability needs to be proved.

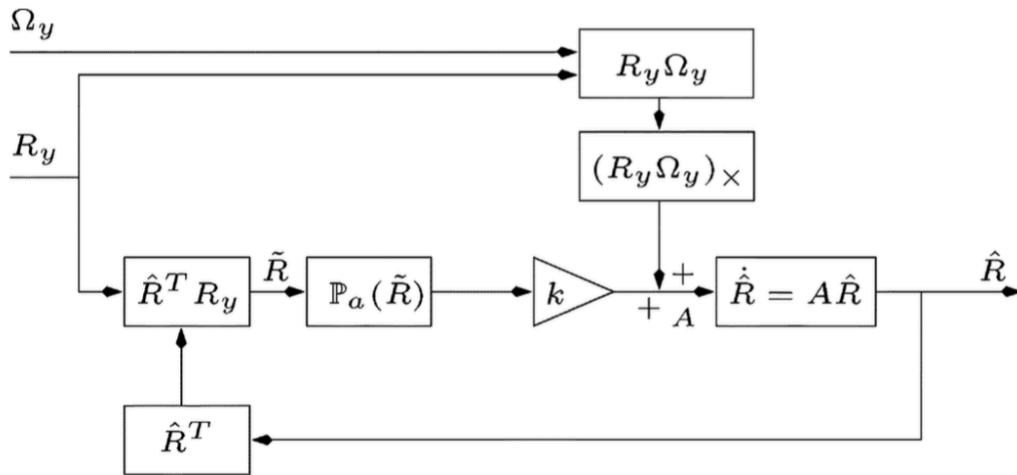


Fig. 3.5 Block diagram of the direct Mahony complementary filter in $SO(3)$ [51].

There is no particular theoretical advantage to use either the direct or the passive filter architecture in the case where exact measurements are assumed. However, it is straightforward to see that the passive filter described in Equation 3.21 can be written as

$$\dot{\hat{R}} = \hat{R}(\Omega_{\times} + k_p \mathbb{P}_a(\tilde{R})) \quad (3.22)$$

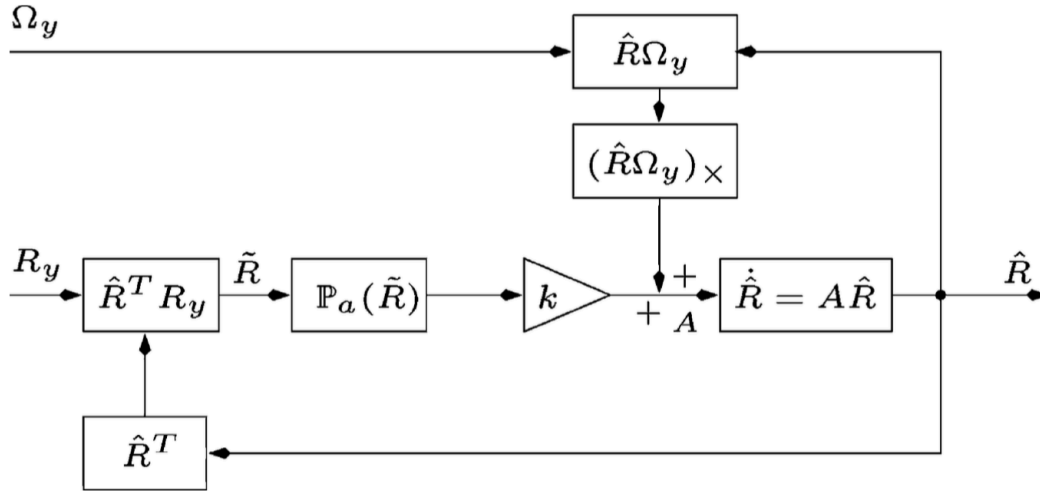


Fig. 3.6 Block diagram of the passive Mahony complementary filter in $SO(3)$ [51].

This formulation suppresses the requirement to represent Ω and $\omega = k_p \mathbb{P}(\tilde{R})$ in the inertial frame I , making the architecture way easier.

Differently from other cases, $SO(3)$ (Appendix A.5) is a *nonlinear* space, and that is where the advantages of a geometric approach can be fully appreciated. Besides nonlinear dynamics, the definition of estimation error requires caution.

Defining R^* and θ^* as the estimates of R and θ , in the linear case $e = \theta - \theta^*$ is a typical choice while quantities such as $R - R^*$ with $R, R^* \in SO(3)$ are no longer guaranteed to belong to $SO(3)$. In this case the error is defined as $E = R^T R^*$.

Campolo et al. [74] developed a geometric approach for the estimation of R in $SO(3)$; in Figure 3.7 is shown the relative functional block diagram.

In the filter they designed gyroscopes are not necessary for stability, at least when tracking a certain subset of trajectories of interest, for which the measurements of 2 vector fields such as the gravitational and the geomagnetic ones are sufficient [75], but knowledge of the angular velocity is beneficial for performance, especially in dynamic attitude estimation, *i.e.* when higher disturbance is present. Hence, these filters can be still used for stable tracking when the information from gyroscopes is completely or partially missing, of course with a worsening of the performance.

From Figure 3.7 can be noticed that the block diagram of the filter, and in particular the integration block $\frac{1}{s}$, is a continuous time filter. Any digital implementation of the filter would transform the filter in a discrete time one, with time sequence t_n and necessarily introduce numerical errors. The main risk is that, as numerical errors accumulate, quantities such as $R_n^* = R^*(t_n)$ are likely to drift away from $SO(3)$, *i.e.* the $\det R_n^*$ very different from 1 and/or $R_n^{*T} R_n^*$ different from the identity matrix I .

52 Performance evaluation of magneto-inertial motion units and sensor fusion algorithms

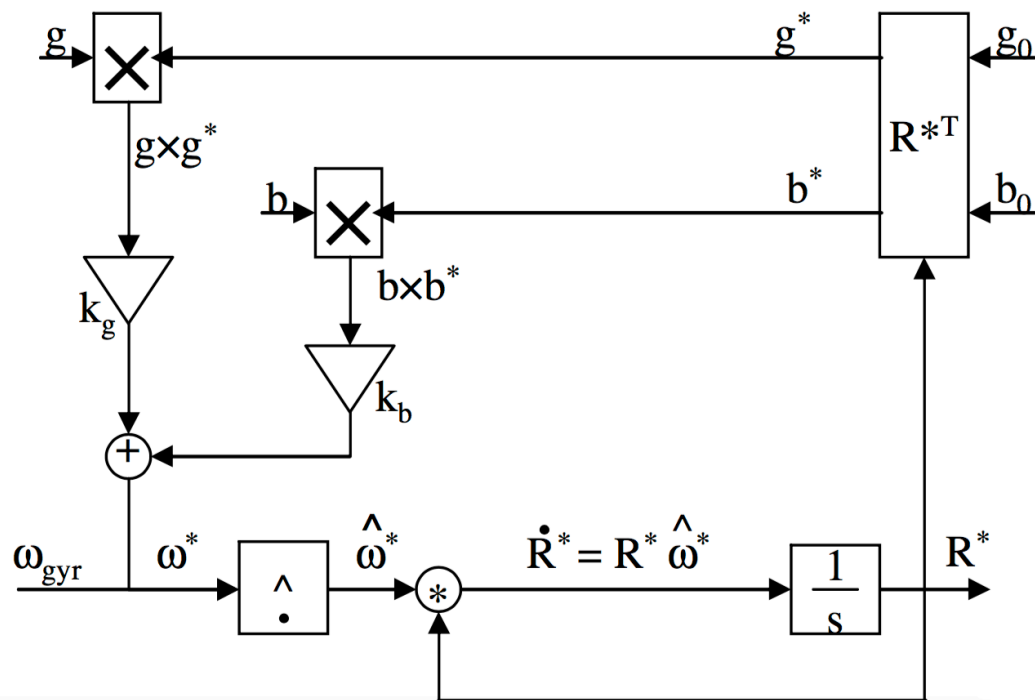


Fig. 3.7 Complementary Filter in $SO(3)$ for dynamic attitude estimation, developed by Campolo et al. [75].

This can be avoided by considering that data from analog sensors are typically acquired via DACs (Digital to Analog Converters) with a fixed sampling time, let this sampling time be ΔT . In the time interval included from a sample and the following one, data from sensors are assumed constant, hence, is it possible to compute R_{n+1}^* via the Rodriguez's formula [76], which is guaranteed not to drift away from $SO(3)$ space.

The parameters used to tune this filter are k_g and k_b that are the gains used to weight the error between the reconstructed (R^*) and the real (R) attitude, depending on the vectors \vec{g} and \vec{m} , using the data reliability acquired from the sensors.

Madgwick et al. [71] [66] introduce an orientation estimation algorithm which employs a quaternion representation to describe the coupled nature of orientations in three dimensions and is not subjected to the problematic singularities associated with an Euler angle representation.

Similarly to the other filters presented above, they fuse together the orientation obtained both from the angular rate (*i.e.* gyroscopes) and vector observation (*i.e.* accelerometer and magnetometer). This filter is schematized in Figure 3.8, where can be noticed how the authors also added two groups of blocs, one to compensate magnetic distortion (Group 1) and the other to compensate the bias given by the gyroscope drift (Group 2). To estimate

the orientation from accelerometers and magnetometers this filter exploits a gradient descent algorithm.

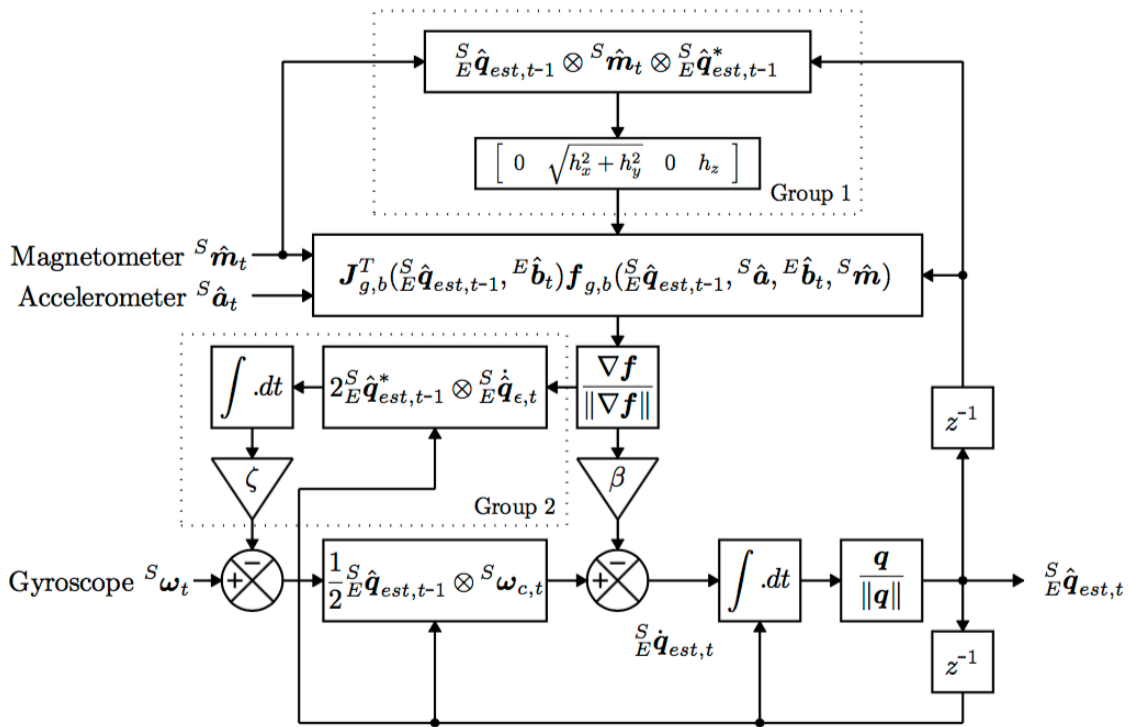


Fig. 3.8 Block diagram representation of the complete orientation filter for a M-IMU implementation including magnetic distortion (Group 1) and gyroscope drift (Group 2) compensation, developed by Madgwick et al. [71].

In the end, this algorithm computes an error based on an analytically derived Jacobian which results in a significant reduction in the computation load relative to a Gauss-Newton method [77]. In addition to this, it can also be used with a lower sampling rate (50-100 Hz) with respect to Kalman filters.

In this filter the two gains used to adjust its performance are β (Equation 3.23) and ζ (Equation 3.24), which represent the gyroscope biases. The first one represents all mean zero gyroscope measurement errors, expressed as the magnitude of a quaternion derivative. The other filter gain is ζ which represents the rate of convergence to remove gyroscope measurement errors which are not mean zero. It is convenient to define β and ζ using the angular quantities $\tilde{\omega}_\beta$ and $\tilde{\omega}_\zeta$ respectively, where $\tilde{\omega}_\beta$ represents the estimated mean zero gyroscope measurement error of each axis and $\tilde{\omega}_\zeta$ represents the estimated rate of gyroscope bias drift in each axis.

54 Performance evaluation of magneto-inertial motion units and sensor fusion algorithms

$$\beta = \left\| \frac{1}{2} \hat{\mathbf{q}} \otimes \begin{bmatrix} 0 & \tilde{\omega}_\beta & \tilde{\omega}_\beta & \tilde{\omega}_\beta \end{bmatrix} \right\| = \sqrt{\frac{3}{4}} \tilde{\omega}_\beta \quad (3.23)$$

$$\zeta = \sqrt{\frac{3}{4}} \tilde{\omega}_\zeta \quad (3.24)$$

The last Complementary Filter we studied and used in this work is the one designed and developed by Tian et al. [49]. They proposed an adaptive-gain orientation filter based on the basic theory of deterministic approach and frequency-based approach (*i.e.* complementary filter).

The deterministic approaches are a variation of the least square minimization problems. One of the solutions to this problem is the QUEST (QUaternion ESTimator) algorithm, a widespread filter used in multi-dimension vector optimization, such as the gradient descent algorithm (GDA) and the Gauss-Newton algorithm (GNA).

The main framework of the proposed filter includes four major parts: the gyro integration; the vector observation, based on the GNA; the CF which merges together the two orientation data; and the compensation schemes. All the groups of blocks which compose the filter are shown in Figure 3.9, and are shown as dotted blocks.

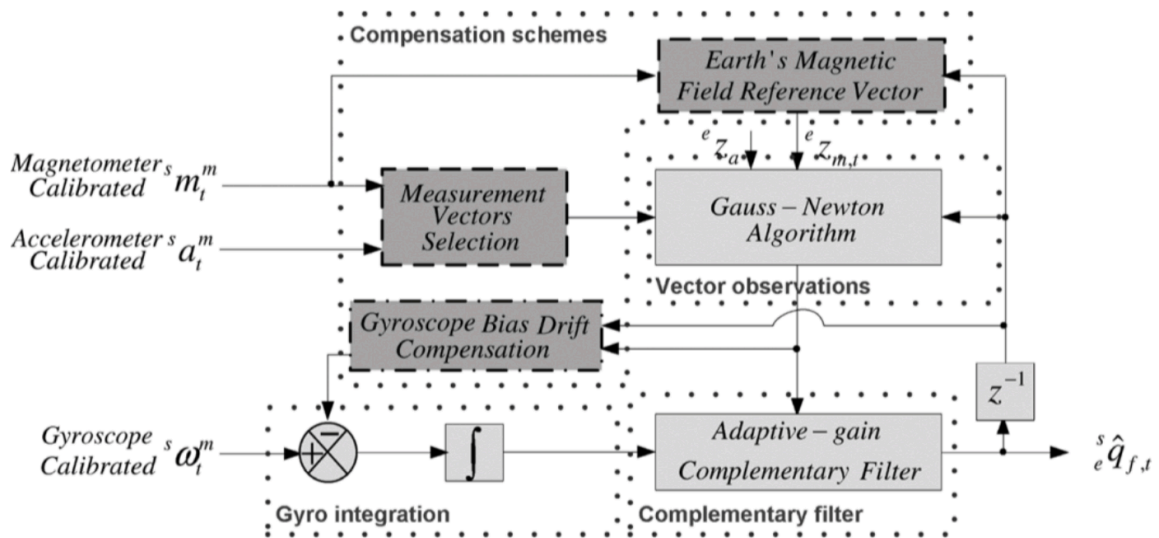


Fig. 3.9 Main framework for orientation estimation of the method proposed by Tian et al. [49].

The main contribution of this filter is given by the analytic approach of combining the GNA with the complementary filter for faster quaternion updates. In addition to this, they

propose a gyroscope bias drift compensation scheme for one input of the complementary filter, and an adaptive-gain complementary filter based on the convergence rate from the GNA and the divergence rate from the gyroscopes.

Analyzing the complete filter schema it is clear that two filter gains, β and ζ , should be determined. Since the theorization of this filter comes from the Madgwick filter, described here above, the two gains can be computed in the same way expressed in Equation 3.23 and Equation 3.24.

3.2.2 Two-frame sensor calibration

As already said, one purpose of our work is to identify the sensor fusion filter algorithm with best performance. To do this, a motion tracking system has been used as ground truth, in order to compare the orientation angle acquired from the sensor and the optical system itself. In fact, the two systems are connected together through a rigid body, and ideally they should give back as output the same orientation of the rigid body which they are connected to with respect to a fixed global reference frame.

To this purpose, it is important to solve the two-frame sensor calibration problem: *i.e.* finding rigid-body homogeneous transformation matrices (X, Y) which best describe the transformations between the M-IMU (\mathbf{S}) and motion capture frames (\mathbf{M}) [78].

To do this, we take into account the idea proposed by Ha et al. [79], which uses a stochastic global optimization method over existing local quaternion-based methods.

Figure 3.10 shows the general context in which the two-frame sensor calibration problem arises. On the body there are two moving frames, one referred to the M-IMU and the other to the stereophotogrammetric system. The transformations between one of these frames and the respective frame at time zero (*i.e.* the fixed frames relative to M-IMU and optical tracking system) are respectively A and B . The two transformations between the two moving frames and the two fixed frames are respectively X and Y .

The way they define the two-frame sensor calibration problem is: given pairs of homogeneous rigid-body transformation matrices (A_i, B_i) , $i = 1, \dots, N$, where each A_i and B_i is a 3×3 homogeneous rigid-body transformation matrix belonging to the special Euclidean group $SO(3)$ of rigid-body rotations, find $X, Y \in SO(3)$ that is a best fit to the N matrix equalities

$$A_i X = Y B_i \in SO(3) \quad i = 1, \dots, N \quad (3.25)$$

In its most common form, this problem is framed as a least-squared optimization problem over $X, Y \in SO(3)$, in which the objective function is given by

56 Performance evaluation of magneto-inertial motion units and sensor fusion algorithms

$$\min_{X, Y \in SO(3)} \sum_i \|A_i X - Y B_i\|^2 \quad (3.26)$$

where $\|\cdot\|$ denotes the Frobenius matrix norm, *i.e.* $\|A\| = \sqrt{\text{tr}(AA^t)}$ for a matrix A .

Here X and Y are unknown; to determine them, various sensors are used to measure the displacements $A_i, B_i \in SO(3)$ of the frames at various configurations of the two rigid bodies. In the absence of measurement noise, the loop closure equation $A_i X = Y B_i$ must be satisfied for all measurements $i = 1, \dots, N$. If the two rigid bodies (and the locations of the attached reference frames) are identical, then $X = Y$, and the loop closure equation simplifies to $A_i X = X B_i$; this is the one-frame sensor calibration problem.

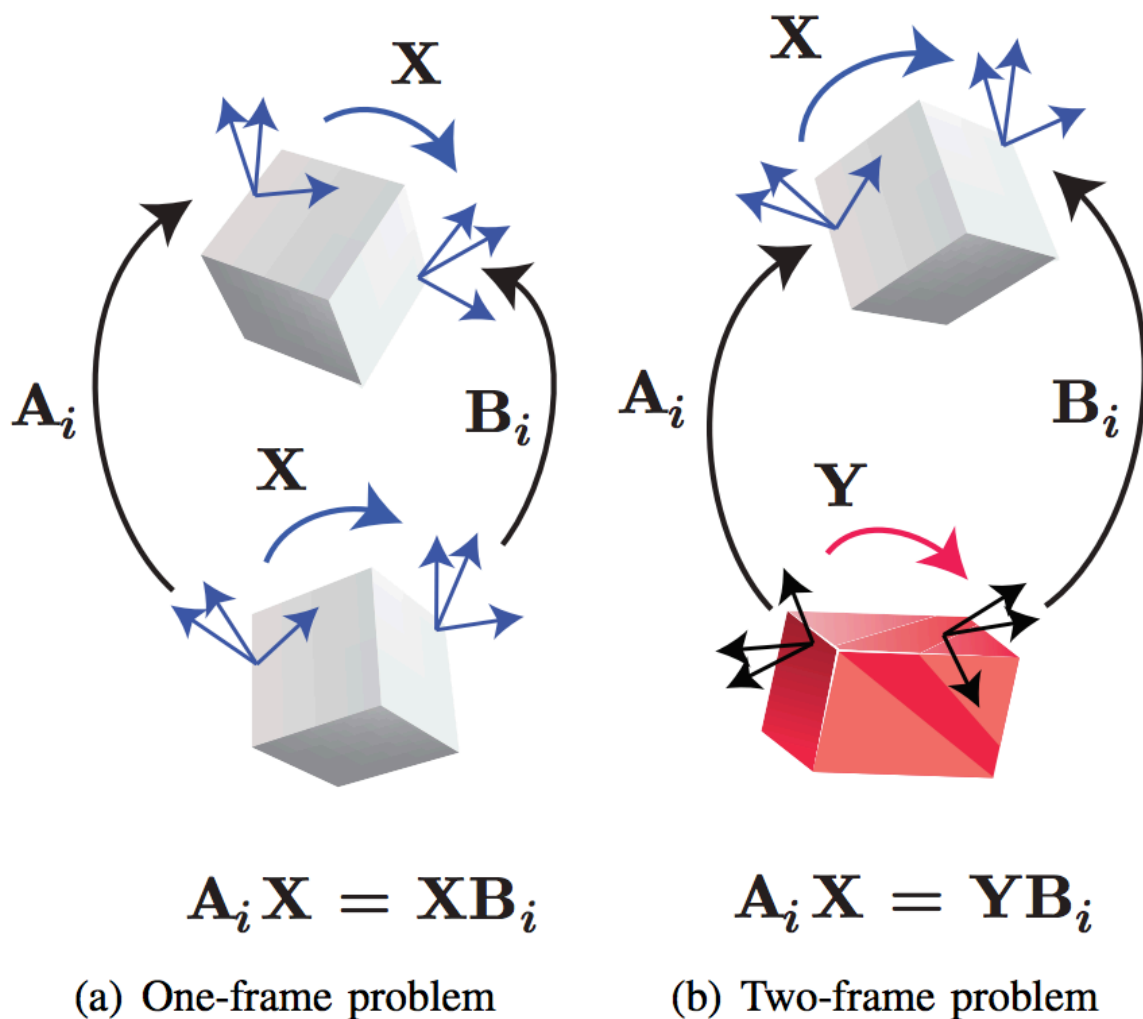


Fig. 3.10 Sensor calibration problems involving (a) one frame and (b) two frame [79].

For example, relative rotations between cameras and M-IMUs on a sensor unit along with their corresponding reference world frames, must satisfy the Equation 3.25 as illustrated in Figure 3.11, where $SO(3)$ denotes the rotation group.

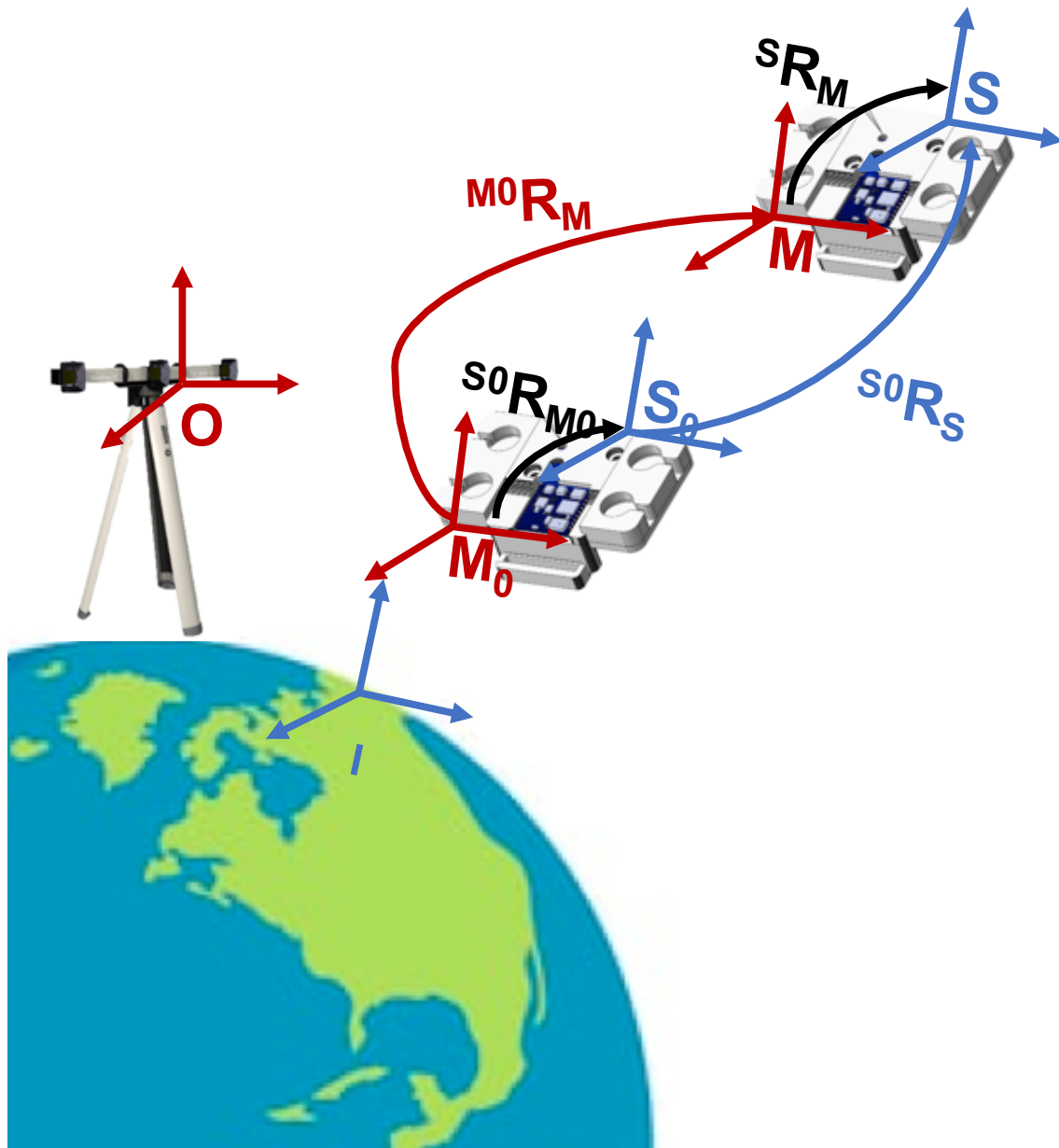


Fig. 3.11 Example of two-frame sensor calibration [79] referred to our specific application. The fixed frames used are M_0 and S_0 respectively for the motion capture and the M-IMU reference frame. The matrices A, B acquired for the two-frame sensor problem solution are respectively ${}^M R_{M_0}$ and ${}^S R_{S_0}$. The output matrices X, Y are ${}^S R_M$ and ${}^{S_0} R_{M_0}$.

58 Performance evaluation of magneto-inertial motion units and sensor fusion algorithms

This method can also be used to evaluate the goodness of the filters used to obtain the representation of the orientation. In fact, after computing the matrices X, Y with the two-frame sensor calibration described by the Equation 3.26, we can make a further acquisition to evaluate the error in the orientation data obtained by the M-IMU.

In that second acquisition, we get new matrices which represent the homogeneous rigid-body transformation of motion capture and M-IMU frames at a certain time t with respect to initial time t_0 . These N pairs of transformation matrices $(C_i, D_i) \in SO(3)$, $i = 1, \dots, N$, can substitute the pairs (A_i, B_i) in Equation 3.25. And with some mathematical operation we obtain

$$Z = D_i^{-1} Y^{-1} C_i X \in SO(3) \quad i = 1, \dots, N \quad (3.27)$$

Since (A_i, B_i) are acquired with the same system setup of (C_i, D_i) , the matrix Z should theoretically be equal to the identity matrix I ; but, due to several errors (*e.g.* sensor noise and filtering error), the M-IMU filter's output may be different between the two acquisition, so that the Z matrix represent the M-IMU filter error in estimating the orientation. Using the logarithm operator defined in the special orthogonal group $SO(3)$ (Appendix A.5), it is possible to compute the angle which represents the rotation error in the filter's output.

To solve this problem it is very important to notice which is the direction of each transformation. As a matter of fact, the two-frame sensor calibration taken into account in this Section is based on the transformations showed in Figure 3.10, but the filters we used may have different ones. For what it concerns the filters described in Section 3.2.1, only the filter developed by Campolo et al. [74] gives the transformation matrix which refers to the rotation from the sensor frame to the fixed frame, all the other filters give the transformation matrix of the fixed frame with respect to the sensor frame.

From all the M-IMU filters it is possible to get the rotation matrix which represents the transformation between the sensor frame and the inertial frame ${}^I R_S$. This matrix at starting time ${}^I R_{S_0}$ represents the rotation between these two frames at the initial time. Of note, the inertial frame does not change during time, that means

$$B = ({}^I R_S)^T \cdot {}^I R_{S_0} = {}^S R_I \cdot {}^I R_{S_0} = {}^S R_{S_0} \quad (3.28)$$

which represents the rotation the sensor frame at a generic time with respect tot the sensor frame at time zero.

For what concerns the motion tracker, it returns the position of the optical markers in the space (\mathbf{M}), with respect to a fixed optical global frame (\mathbf{O}) defined by the optical tracker system. From three markers, as explained in Section 3.2.4, it is possible to define a frame

referred to a moving body and we can represent the rotation of this frame with respect the global frame ${}^O R_M$. Similarly to the M-IMU orientation, we can obtain the orientation from the motion tracker as follow

$$A = ({}^O R_M)^T \cdot {}^{O_0} R_{M_0} = {}^M R_O \cdot {}^O R_{M_0} = {}^M R_{M_0} \quad (3.29)$$

These are the matrices A, B used to solve the two-frame sensor problem, where the matrix obtained are

$$X = {}^S R_M \quad Y = {}^{S_0} R_{M_0} \quad (3.30)$$

and utilized to compute the error given by the result of $\log(Z)$ in $SO(3)$ (Appendix A.5), where

$$Z = D_i^{-1} Y^{-1} C_i X = ({}^S R_{S_0})^{-1} ({}^{S_0} R_{M_0})^{-1} ({}^M R_{M_0}) ({}^S R_M) \quad (3.31)$$

3.2.3 Generation of synthetic M-IMU data

Before tuning and evaluating the filters with real data, some simulated M-IMU data have been generated and used to test the proposed algorithms. In this Section we are going to describe how to generate virtual magneto-inertial data from a given pose of a rigid body, *i.e.* a trajectory in the space and a orientation in $SO(3)$.

Given a body frame \mathbf{B} , identified by three orthogonal directions on a rigid body, monoaxial sensors are, by construction, assembled on a rigid body in such a way that their sensitive axes coincides with one of axes defined by \mathbf{B} .

As shown in Figure 3.12, at a generic time t the M-IMU sensor, colored in green, has a frame centered in O'' . It is attached to a rigid body, colored in blue, which refers to a moving frame centered in O' ; their movements are jointed and the distance between the two frames is given at the initial time t_0 by the vector $\vec{a} = \overrightarrow{O'O''}$ of fixed modulus. The rigid rotation of the moving and sensor frames, with respect to the fixed frame, are represented by the matrix $R \in SO(3)$. The displacement of the moving frame, with respect to the fixed frame centered in O , is given by the vector $\overrightarrow{OO'}$; while the displacement of the sensor frame with respect to the fixed frame is represented by the vector $\overrightarrow{OO''} = \overrightarrow{OO'} + R \cdot \vec{a}$.

By construction, a set of three monoaxial gyroscopes provides the components of the angular velocity, expressed in $\frac{rad}{s}$, with respect to the body frame \mathbf{B} , and can be computed applying the *vee* operator (Appendix A.5) to

$$g\hat{y}r = \hat{\omega} = R^T \dot{R} \quad (3.32)$$

60 Performance evaluation of magneto-inertial motion units and sensor fusion algorithms

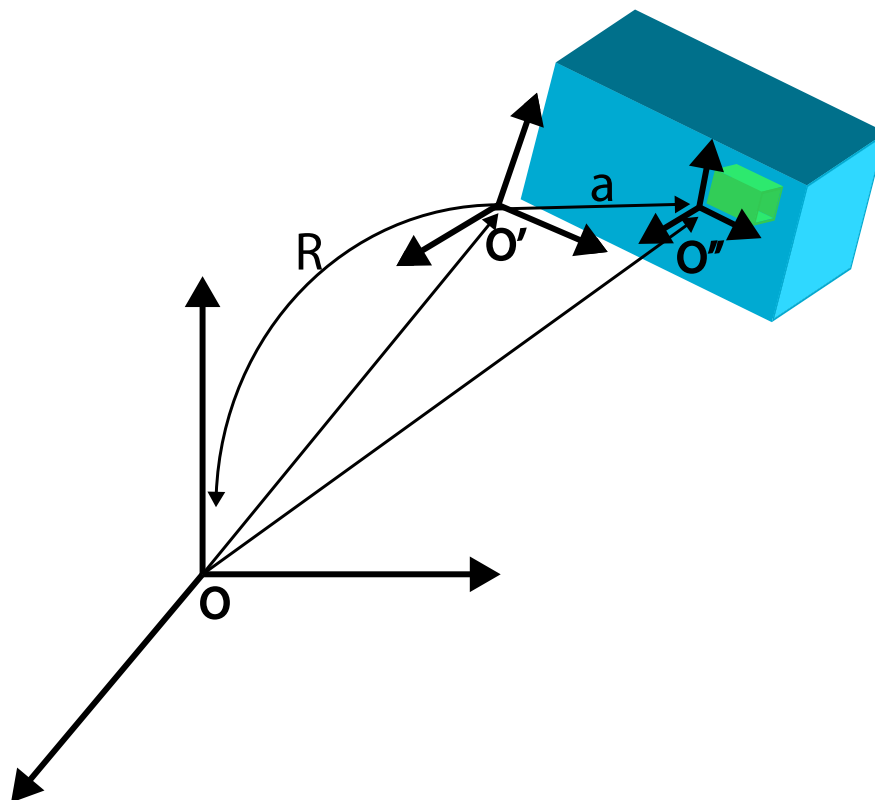


Fig. 3.12 Transformation of a sensor fixed on a rigid body. The fixed frame is the one centered in O , the moving frames are the body one, centered in O' , and the sensor centered in O'' .

For what it concerns the value of accelerometer, the vector $\overrightarrow{OO''}$ need to be derived two times in order to obtain the acceleration of the M-IMU sensor from the displacement. In addition to this, the accelerometers will also measure the gravity vector, that has a constant modulus equal to \vec{g} and fixed direction with respect to the fixed frame. Hence,

$$acc_{gravity} = R^T \cdot \begin{bmatrix} 0 \\ 0 \\ -g \end{bmatrix} \quad (3.33)$$

As already said, the other element which composes the accelerometer signal is acceleration of the body, given by the double derivative of $\overrightarrow{OO''}$

$$\overrightarrow{OO''} = \overrightarrow{OO'} + R \cdot \vec{a} \quad (3.34)$$

$$\dot{\overrightarrow{OO''}} = \dot{\overrightarrow{OO'}} + \dot{R} \cdot \vec{a} + R \cdot \dot{\vec{a}} = \dot{\overrightarrow{OO'}} + R \cdot \omega \cdot \vec{a} \quad (3.35)$$

$$acc_{body} = \overrightarrow{OO''} = \overrightarrow{OO'} + \dot{R} \cdot \omega \cdot \vec{a} + R \cdot \dot{\omega} \cdot \vec{a} + R \cdot \omega \cdot \vec{a} = \overrightarrow{OO'} + R \cdot \omega^2 \cdot \vec{a} + R \cdot \dot{\omega} \cdot \vec{a} \quad (3.36)$$

where $\vec{a} = 0$ because a is constant during time; and, since we know from Equation 3.32 that $\hat{\omega} = R^T \dot{R}$, hence we can write $\dot{R} = R \cdot \hat{\omega}$.

Hence the final value of the simulated accelerometer sensors is

$$acc = \overrightarrow{OO'} + R \cdot \omega^2 \cdot \vec{a} + R \cdot \dot{\omega} \cdot \vec{a} + R^T \cdot \begin{bmatrix} 0 \\ 0 \\ -g \end{bmatrix} \quad (3.37)$$

Finally, for what concerns magnetometers, they theoretically measure only the three components of the Earth's magnetic field vector \vec{m} . It is not perpendicular with the \vec{g} vector; it has an inclination, *i.e.* the angle γ between the vector and the horizontal plane is variable at any location (*e.g.* $\approx 14^\circ$ at Singapore³). The module M of this vector ranges between approximately 25 and 65 μT [80]. Hence, the vector which represents the Earth's magnetic field can be described with two components, and the simulated value measured by magnetometers is

$$mag = R^T \cdot \begin{bmatrix} M \cdot \cos(\gamma) \\ 0 \\ -M \cdot \sin(\gamma) \end{bmatrix} \quad (3.38)$$

In addition to this, it is also important to emulate the noise of each sensor [81], to do that a quick estimation of it can be easily taken from sensor's datasheets.

3.2.4 Filter tuning and performance evaluation of M-IMUs' sensor fusion algorithms

Most of the commercial IMUs do not explain the detail of the orientation estimation algorithm implemented and it is quite difficult to compare the performance among them. The embedded sensors specifications on the attitude evaluation are often not clearly stated and the performance among them are hardly comparable.

The objective of this part of the work is to find a standard and reliable method in $SO(3)$ to tune and compare filters used to get orientation from M-IMU sensors. As we have already described in Section 3.2.1, each filter exploits some gain parameters to tune the output of the filter. Knowing that, it is important to understand how to tune these parameters, but also find

³It is possible to find these values in some government websites, *e.g.* Natural Resources Canada (<http://geomag.nrcan.gc.ca/calc/mfcal-en.php>).

62 Performance evaluation of magneto-inertial motion units and sensor fusion algorithms

a way to compare all the filters, in order to understand which of them is the best solution to apply.

System Architecture

The hardware used in this experiment is composed of a device embedding a M-IMU, *i.e.* the SensorTile by STMicroelectronics, and an optical motion capture system used as ground truth, *i.e.* the VZ4000v by Phenix Thechnologies Inc. (PTI).

SensorTile⁴ is a highly integrated development platform with a broad range of functions aimed at improving system design cycles and accelerating the delivery of results. This device perfectly fits with our purpose, in fact it is cheap and immediate to use, with respect to other industrial M-IMU systems already existing on the market.

The tiny SensorTile core system board (13.5 mm x 13.5 mm) embeds high-accuracy and very low-power inertial sensors, a barometric pressure sensor and a digital MEMS top-port microphone. The onboard 80-MHz MCU features ultra low-power support. The wireless network processor provides BLE connectivity and the integrated balun maximizes RF performance for minimum size and design effort.

It can be mounted on a compact cradle host, which features a battery charger and SD card interface for on-field testing and data acquisition. The complete mounted module is shown in Figure 3.13. In its kit it is also provided by a plastic case to put in and a 100 mAh LiPO battery.



Fig. 3.13 SensorTile module, soldered on the Cradle board, powered with the battery and inserted in its case.

⁴STMicroelectronics, “STEVAL-STLKT01V1: SensorTile development kit,” DB2956, 2017.

In particular it embeds the following M-IMU sensors:

- **LSM6DSM**⁵ is a system-in-package featuring a 3D digital accelerometer and a 3D digital gyroscope. It can use both SPI and I²C as data transmission protocol. The LSM6DSM has a full-scale acceleration range of $\pm 2/\pm 4/\pm 8/\pm 16\text{ g}$ and an angular rate range of $\pm 125/\pm 250/\pm 500/\pm 1000/\pm 2000\text{ dps}$.

We decided to use the accelerometer with a full-scale acceleration of $\pm 2\text{ g}$ with a sensitivity of 0.061 mg/LSB ; that means the accelerometer's noise density is $\sim 75\text{ }\mu\text{g}/\sqrt{\text{Hz}}$. The gyroscope full-scale has been set to 2000 dps with a sensitivity of 70 mdps/LSB ; its noise density is $\sim 3.8\text{ mdps}/\sqrt{\text{Hz}}$. Both sensors have a resolution of 16 bits per axis.

- **LSM303AGR**⁶ is a ultra low-power high-performance system-in-package featuring a 3D digital linear acceleration sensor and a 3D digital magnetic sensor. It has linear acceleration full scale of $\pm 2/\pm 4/\pm 8/\pm 16\text{ g}$ and a magnetic field dynamic range of $\pm 50\text{ gauss}$. The LSM303AGR includes an I²C serial bus that supports standard, fast mode, fast mode plus, and high-speed (100 kHz, 400 kHz, 1 MHz, and 3.4 MHz) and an SPI serial standard interface. It has a digital resolution of two bytes per axis, *i.e.* its magnetic resolution is around 2 mgauss .

The accelerometer of this sensor has not been used, since we decided to use the one included in the LSM6DSM. For what concerns the magnetometer we used the full scale $\pm 50\text{ gauss}$ with a sensitivity of $\sim 1.5\text{ mgauss/LSB}$; it has a RMS noise equal to $\sim 3\text{ mgauss}$.

All these sensors are sampled at 100 Hz that is also the sampling frequency of the internal Kalman filter provided by STM.

The SensorTile is programmed to acquire data and transfer them through BLE to a master board which communicates with the PC using a USB cable. This master board is composed of two STM boards, the MCU NUCLEO-F401⁷ and *BlueNRG* expansion X-NUCLEO-IDB05A1⁸.

⁵STMicroelectronics, "iNEMO inertial module: always-on 3D accelerometer and 3D gyroscope", DS11179, 2017.

⁶STMicroelectronics, "Ultra-compact high-performance eCompass module: ultra-low-power 3D accelerometer and 3D magnetometer", DS10999, 2017.

⁷STMicroelectronics, "STM32F401xD STM32F401xE: ARM cortex-m4 32B MCU+FPU, 105 DMIPS, 512kB flash/96kB RAM, 11 TIMs, 1 ADC, 11 comm. interfaces," DS10086, 2017.

⁸STMicroelectronics, "X-NUCLEO-IDB05A1: Bluetooth low energy expansion board based on the SPBTLERF module for STM32 nucleo," DB2592, 2015.

64 Performance evaluation of magneto-inertial motion units and sensor fusion algorithms

VZ4000v⁹, shown in Figure 3.14 is part of a family of 3D motion measurement and tracking systems called *Visualeyez*, developed by Phenix Technologies Inc. (PTI). It consists of only a tracking unit with tripod, target control modules, light emitting diode (LED) targets, and a graphical user interface represented by the software *VZSoft*¹⁰. The tracking unit detects the lights from a LED target, calculates its 3D position, then transmits the computed position coordinates to the host computer immediately. This is carried out for each LED target in sequence, one at a time, at very high speed.



Fig. 3.14 *Visualeyez II VZ4000v* motion tracker by Phenix Technologies Inc.

The LED target positions are captured one by one in the user-specified order and sampling interval. After all targets in the user-specified 'target sampling sequence' have been captured once (*i.e.* when capture cycle is complete), the system will command all LED to

⁹*Visualeyez II VZ4000v* motion tracker by Phenix Technologies Inc. (<http://www.ptiphoenix.com/products/trackers/VZ4000v>).

¹⁰*VZSoft* Graphical User Interface (<http://www.ptiphoenix.com/products/software/VZSoft>).

re-synchronize in case noise caused one or more of them to go out of synchronization with the others; then, another capture sequence will be repeated.

The three sensing cameras of VZ4000v tracker capture lights from a LED target for subsequent computation of its coordinates. Each eye has an operating angle of $\pm 45^\circ$ (for a total of $\pm 90^\circ$) in both pitch and yaw directions. In order to compute the three-dimensional coordinates of a target, all three eyes must see the target simultaneously when the target is illuminated.

The motion tracker also provides an End-Of-Frame (EOF) signal pulse that can be brought out to trigger other equipment to sample additional signals synchronized with this system.

The VZ4000v's technical specifications are summarized in Table 3.1, and a schema of the work space is shown in Figure 3.15.

Table 3.1 Technical specification of *Visualeyez II* VZ4000v motion tracker.

Sensing Volume	$\sim 190 \text{ m}^3$ of useful space, over 7.0 m radius
Minimum Sensing Distance	0.5 m
Position Resolution	0.015 mm at 1.2 m distance
Number of Markers	512 Max
Accuracy	0.5~0.7 mm RMS
Operation Angle	$90^\circ (\pm 45^\circ)$ in both pitch and yaw (107° diagonally)
Sensing Rate	~ 4500 rel-time 3D data points per second
Data Latency	< 0.0005 s at maximum sample rate
Computer Communication	Serial RS232/RS422 (922.6 kbps) real-time protocol

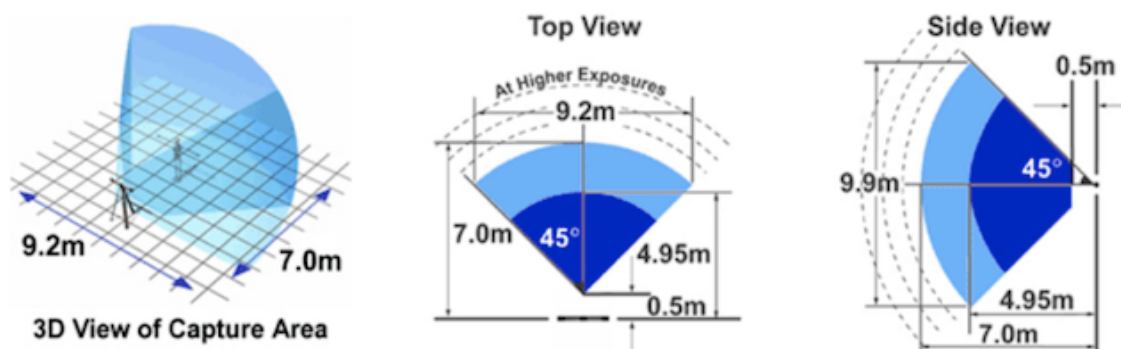


Fig. 3.15 VZ4000v sensing volume.

Two-frames sensor setup

In order to evaluate the goodness of the orientation obtained from M-IMU we need to connect the SensorTile to the LED target markers of the motion capture system through a rigid body.

To do this, we designed and printed, using the N2 3D printer by Raise 3D¹¹, a housing which can hold both SensorTile and LEDs. As can be seen in Figure 3.16, there are four slots for the LEDs, but in the end we need only three of them to draw a frame (\mathbf{M}) which motion capture system may refer to.

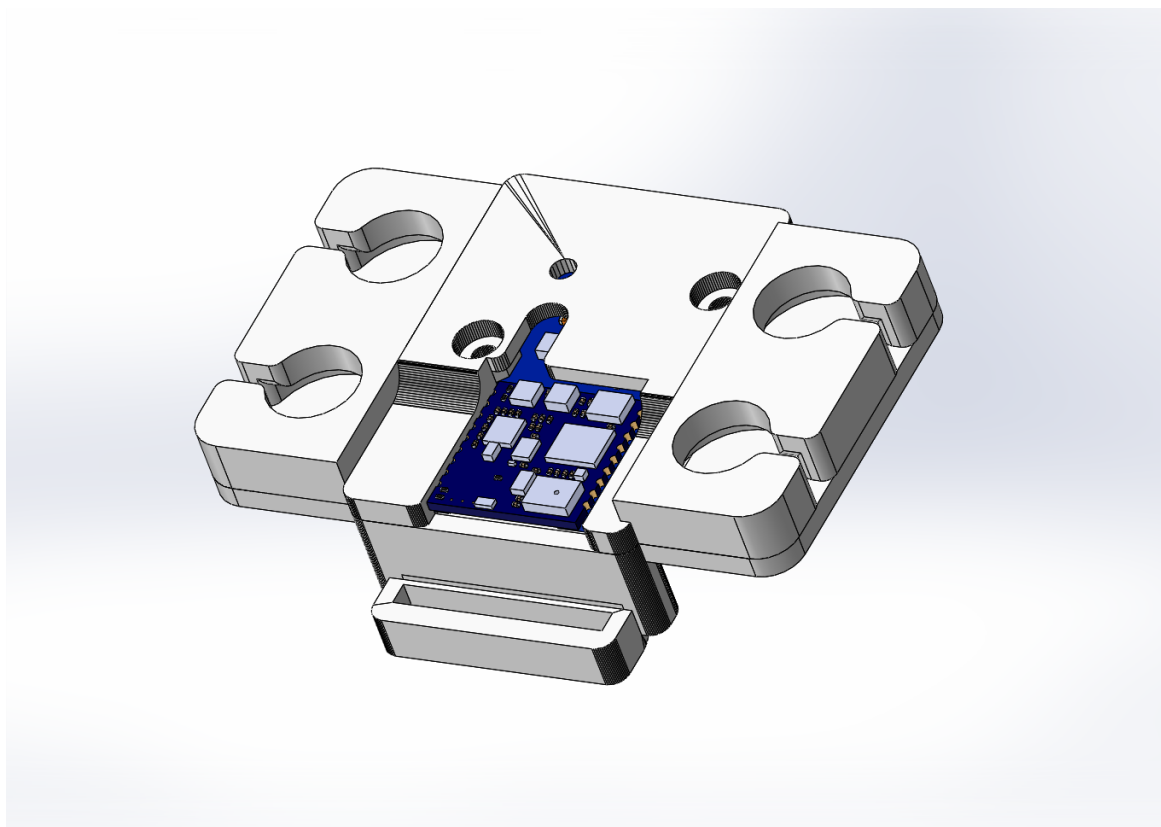


Fig. 3.16 Assembly of SensorTile and LED targets. (AGGIUNGERE LED AL CAD TODO)

The M-IMU motion capture reference frame (\mathbf{S}) is the one defined from the embedded accelerometer sensor (Figure 3.17), while the other sensors, *i.e.* gyroscopes and magnetometers, are modified so that their frames coincide with the one of accelerometer.

For what it may concern the motion capture frame \mathbf{M} , as already said we put three LEDs in the case and we tried to obtain a frame \mathbf{M} as much like as possible to the one defined by the SensorTile \mathbf{S} , even if it is not strictly necessary. Hence, after defining the LEDs L_1, L_2

¹¹N2 3D printer by Raise 3D (<https://www.raise3d.eu/products/raise3d-n2-fff-3d-printer>).

and L_3 , and the vectors \hat{v}_1 and \hat{v}_2 , as shown in Figure 3.17, we fix the x-axis as $-\hat{v}_1$, the z-axis as the cross product $\hat{v}_1 \times \hat{v}_2$ and the y-axis as the cross product $\hat{v}_1 \times \hat{z}$.

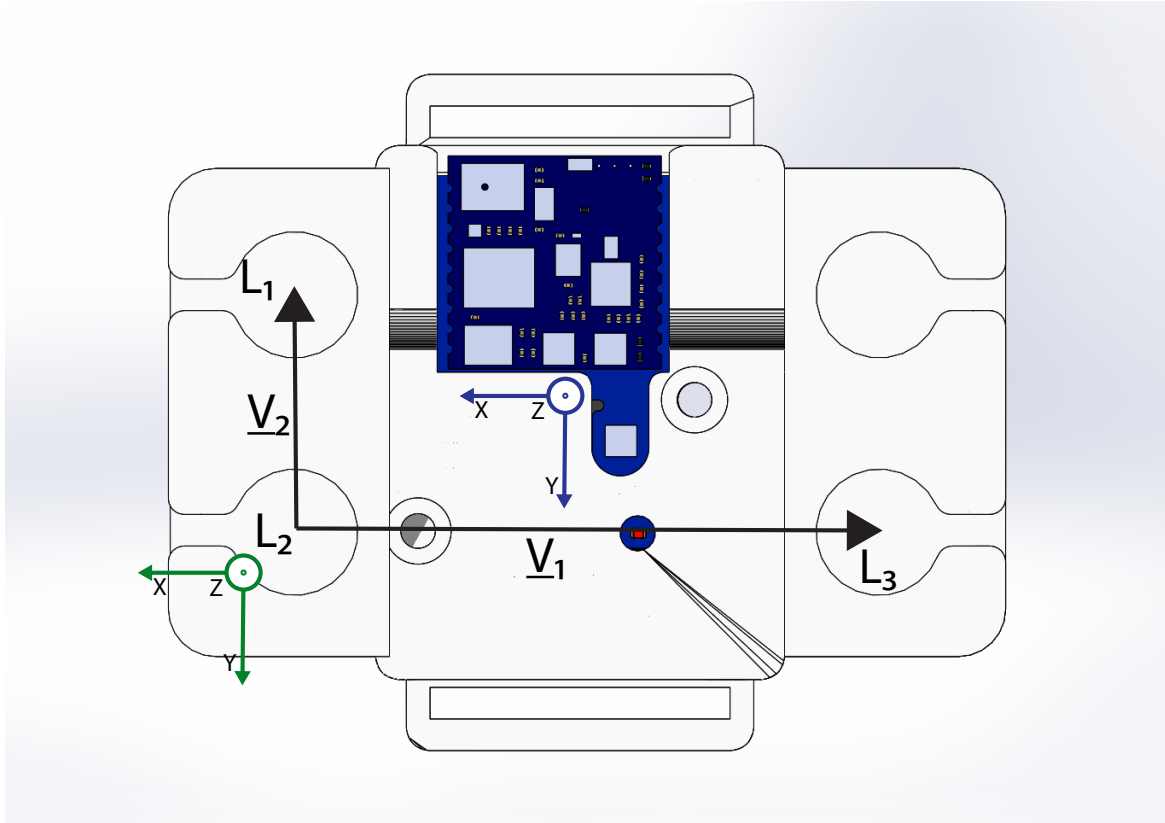


Fig. 3.17 Assembly of SensorTile and LED targets, top view. The three LEDs we put in the case are represented as L_1 , L_2 and L_3 . The vectors used to compute the three axes of the motion tracking frame \mathbf{M} are \vec{v}_1 and \vec{v}_2 . The three-dimensional frame represented in blue is the one referred to the M-IMU frame \mathbf{S} . The green reference frame represents three-dimensional frame referred to the optical motion tracking system \mathbf{M} .

The rotation matrix which represents the orientation of the motion tracking sensors with respect to the global frame defined by the VZ4000v \mathbf{O} is given by

$${}^O R_M = [\hat{x} \hat{y} \hat{z}] \quad (3.39)$$

Usually a preprocessing stage is needed in order to synchronize together each sensor and the ground truth utilized. To do that, we synchronize together SensorTile and the motion capture system, sending a trigger from the VZ4000v to the M-IMU master board to start the acquisition of the SensorTile. After some trials, we measure that the latency between the beginning of the acquisition of the motion tracker and the sensor tile is 15.3 ± 0.9 ms of mean and standard error.

68 Performance evaluation of magneto-inertial motion units and sensor fusion algorithms

Protocol

As we have already said, the objective of this experiment is to understand how to tune the different filters and evaluate the performance of each of them in $SO(3)$.

The first step is to evaluate filters with emulated M-IMU data, generated as explained in Section 3.2.3. We add a white gaussian noise to those data with a density equal to $75 \mu g/\sqrt{Hz}$ for accelerometer, $3.8 \text{ mdps}/\sqrt{Hz}$ for gyroscopes, $3 \mu T$ RMS for magnetometer and we generate sensor data from a specific trajectory. This trajectory is composed of ten monoaxial movements, with an amplitude of the rotation equal to $\pi/5$ and the axis of rotation is different per each movement; the frequency used to virtually sample these sensors is 100 Hz . Each rotation follows a minimum jerk trajectory in a time of 0.5 s , then it stops for 2 s ; resulting simulated trajectories are represented in Figure 3.18.

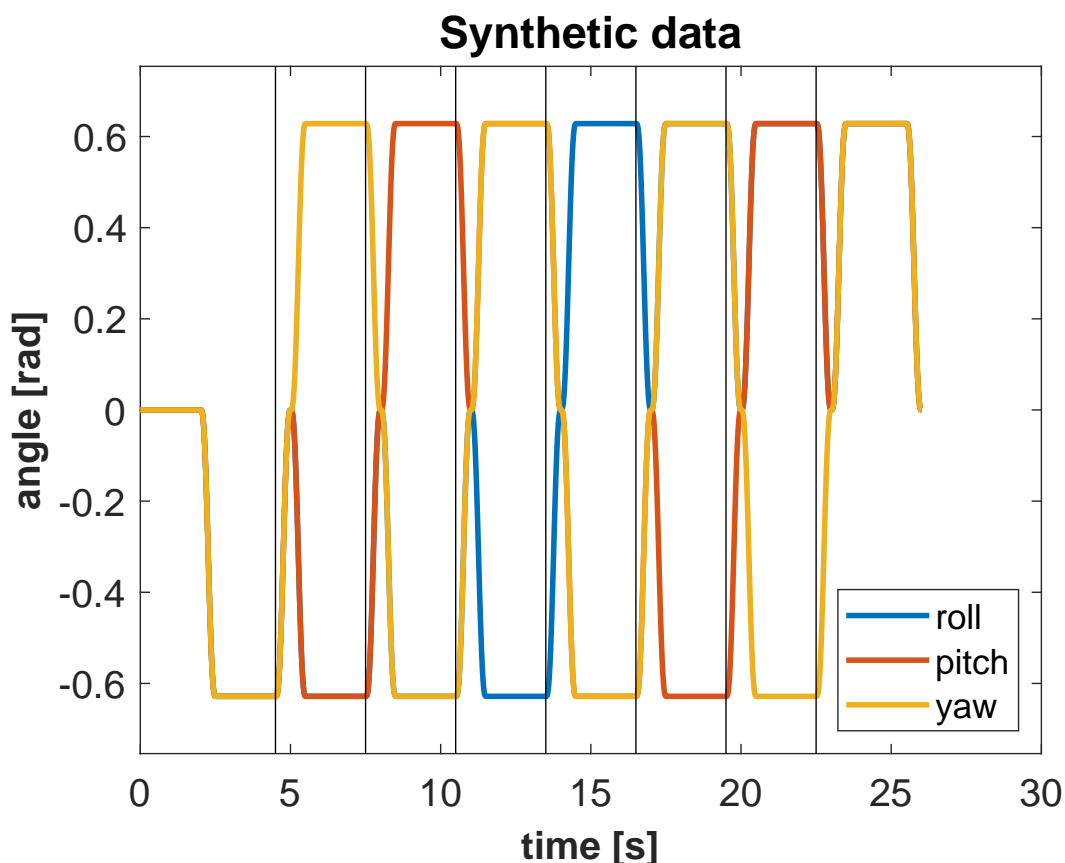


Fig. 3.18 Trajectory used to compute M-IMU data from a known rotation. The vertical black bars represents the points used as input data to resolve the two-frame problem algorithm.

So we firstly use this trajectory to tune each filter, *i.e.* find the value of the gains which minimizes the error. To do that, we defined for each sensor a set of parameter to test. After

several trials, we found the range of gain variation, where filter's error has usually the minimum value, is between 0 and 0,3. Kalman filter, Section 3.2.1, has not been analyzed since we used a closed library developed by STM, so it is not possible to tune it; in particular, this filter automatically handles the gyroscope calibration by continuously compensating the zero-rate offset effect.

We analyzed all these data using MATLAB and, in particular, since we have a very high computational burden we use the parallel computing toolbox, which exploits all the cores of the PC.

Given all the data we acquired, we firstly fit the data in order to get a function of one or two degrees of freedom, depending on the number of parameters, secondly we do an unconstrained optimization with the particle swarm solver [82] to obtain the global minimum of the function.

After finding the best parameter for each of this sensors we started the performance evaluation of each filter. In the case of synthetic data, we do not need to solve the two-frame sensor problem, because the ground truth is a trajectory defined by us. So we can directly measure how much is the error per each sensor, as already explained in Section 3.2.4.

After doing this evaluation with synthetic data, we do the same analysis using data acquired with the SensorTile and the optical motion tracker system. For the assessment with real data, we first perform a calibration of gyroscopes and magnetometers, as explained in Sections 3.1.1 and 3.1.3. As already said, we executed two acquisitions in order to generate two separate dataset: the first one is needed to calibrate the different system reference frames (*i.e.* to solve the two-frame problem); the second one to evaluate the accuracy of the different filters.

For the calibration dataset, we only use static poses in order to let the filters converge and reduce the error as much as possible. To do that, we keep the M-IMU fixed for a short period of time (around 20 s) after each movement, and acquire data exclusively in that static poses. On the other side, for evaluation dataset, we made different movements and acquire data during the whole procedure. In this experiment, with real data, we can also add the results relative to proprietary Kalman filter embedded in the MCU of the SensorTile.

Results

First of all, in Figure 3.19 are shown the error angles variations with respect to the filters' gain variation for each filter. Some of them have only one parameter to tune, such as Madgwick Figure 3.19d and the gyroscope integration Figure 3.19a, while the others have two gains to tune. The values measured in each graph is the error angle expressed in *rad*, computed as explained in Section 3.2.2, relatively to synthetic data.

70 Performance evaluation of magneto-inertial motion units and sensor fusion algorithms

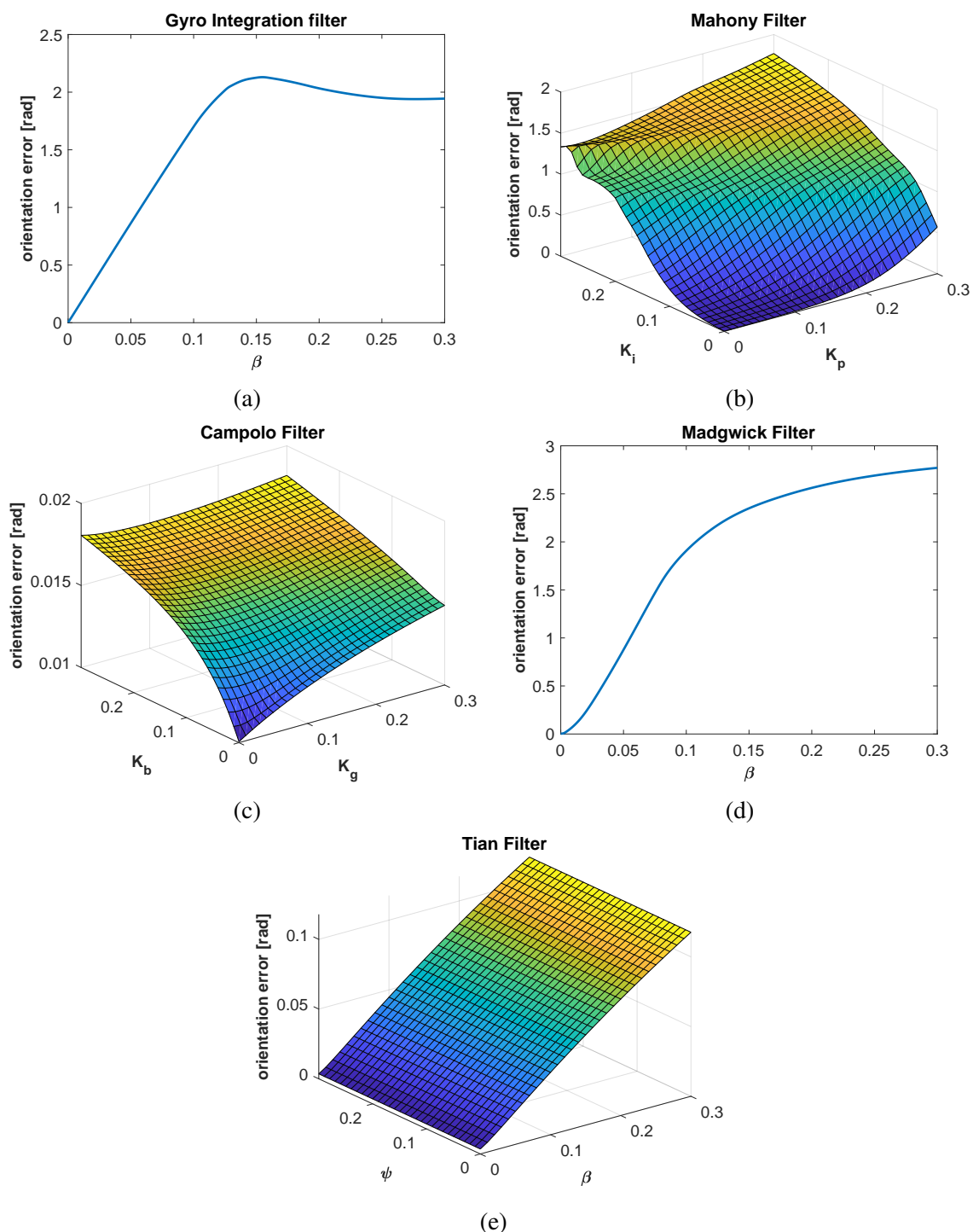


Fig. 3.19 Tuning of orientation filters using synthetic M-IMU data. The value measured is the error angle (Equation A.19), expressed in *rad*, represents the displacement between the M-IMU sensor fusion filter algorithm and the ground truth. Figure 3.19a represents the parameters of gyroscope integration filter, Figure 3.19b is Mahony filter [51], Figure 3.19c is Campolo filter [74], Figure 3.19d is Madgwick filter [66] and Figure 3.19e is Tian [49].

3.2 Validation of sensor fusion algorithms for attitude estimation with M-IMUs 71

Tuning the filters we obtain the optimal gains which give back the lowest error angle possible. The gains obtained and used to compute the error angle are shown in Table 3.2.

Table 3.2 Error angle represented by mean \pm standard deviation and maximum peak value, computed with optimal gain parameters.

Filter	Gain value	error angle	Max peak
Gyro integration [66]	$\beta = 0$	0.0039 ± 0.0076 rad	0.0243 rad
Madgwick [66]	$\beta = 0$	0.0040 ± 0.0075 rad	0.0243 rad
Mahony [51]	$K_p = 0$ $K_i = 0$	0.0040 ± 0.0075 rad	0.0243 rad
Campolo [74]	$K_g = 0$ $K_b = 0$	0.0118 ± 0.0227 rad	0.0727 rad
Tian [49]	$\beta = 0.0082$ $\psi = 0$	0.0080 ± 0.0066 rad	0.0308 rad

In Figure 3.20 are shown the values of the error angles obtained using the gain parameters computed previously. In particular, its mean value with the standard deviation, and the maximum peak value are represented in Table 3.2.

Then, we analyzed data which come from a real acquisition with the SensorTile and the motion tracker.

The trajectory acquired from the calibration dataset, the one used to solve the two-frame sensor problem, is shown in Figure 3.21. First of all, we tune the filters on this trajectory (*i.e.* the calibration dataset), in Figure 3.22 it is possible to see the error angle relative to each filter, in relation to the variation of the gain parameters; secondly, we compute the X, Y matrices using the evaluation dataset (Section 3.2.2).

During the acquisition with the evaluation dataset, the one used to evaluate filter performance, the trajectory is mainly composed of monoaxial movements, shown in Figure 3.23. On this data we firstly tune the filters used (Figure 3.24), then we evaluated the error of the filter, as explained in Section 3.2.2. The optimal gains are reported in Table 3.4 together with the error angle, represented in mean and standard deviation, and the maximum peak reached by the error itself. In addition to this, the error path per each filter is also shown in Figure 3.26.

Another important parameter to be analyzed is the computational time spent by each filter to get orientation from M-IMU data. These results are shown in Table 3.5. Of note, it is not possible to compare the computational time needed by the Kalman filter in the MCU with the filters algorithms used on MATLAB.

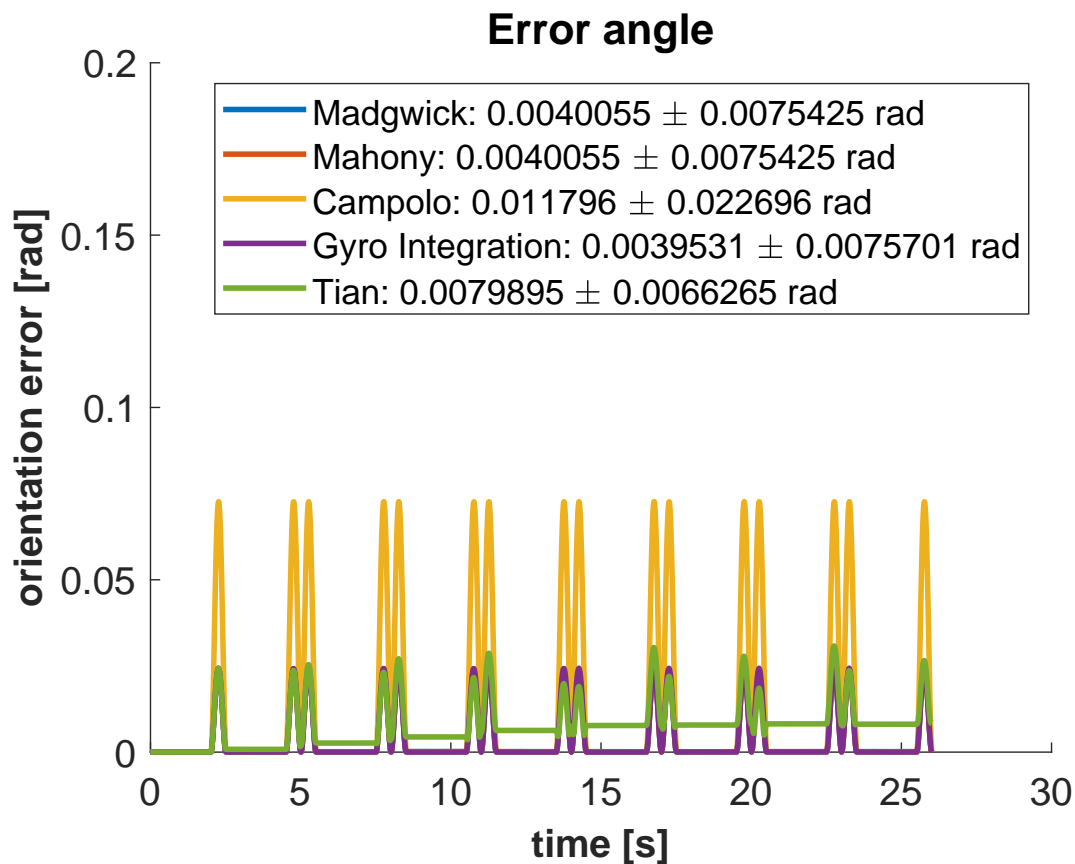


Fig. 3.20 Error angle computed per each filter on synthetic data, using the optimal gain parameters.

Discussion and conclusions

The aim of this work is to propose a standard method for analyzing, tuning and evaluating performance of several sensor fusion filters. Since other works in the literature have already analyzed the performance of different sensor fusion filters with M-IMUs [54], we decided to propose a new methodology in $SO(3)$ based also on a preprocessing of data which aims to tune filter parameters in order to obtain the best performance for each specific application. Since it is not possible to do a detailed and complete analysis, taking into account all the possible filters present in the literature with their relative parameters, we decided to do this methodological work in order to measure the quality of the filter.

For what concerns the experiment based on the synthetic data, it can be easily noticed how all the gains are close to zero. That is related to the low noise value; in fact, the gains can be used either to compensate the gyroscope drift or as multiplicative factors of accelerations and magnetic field errors; in that case, since the gyroscope value is affordable due to the low value of the noise, it is not needed to compensate and all the filters mainly use zero

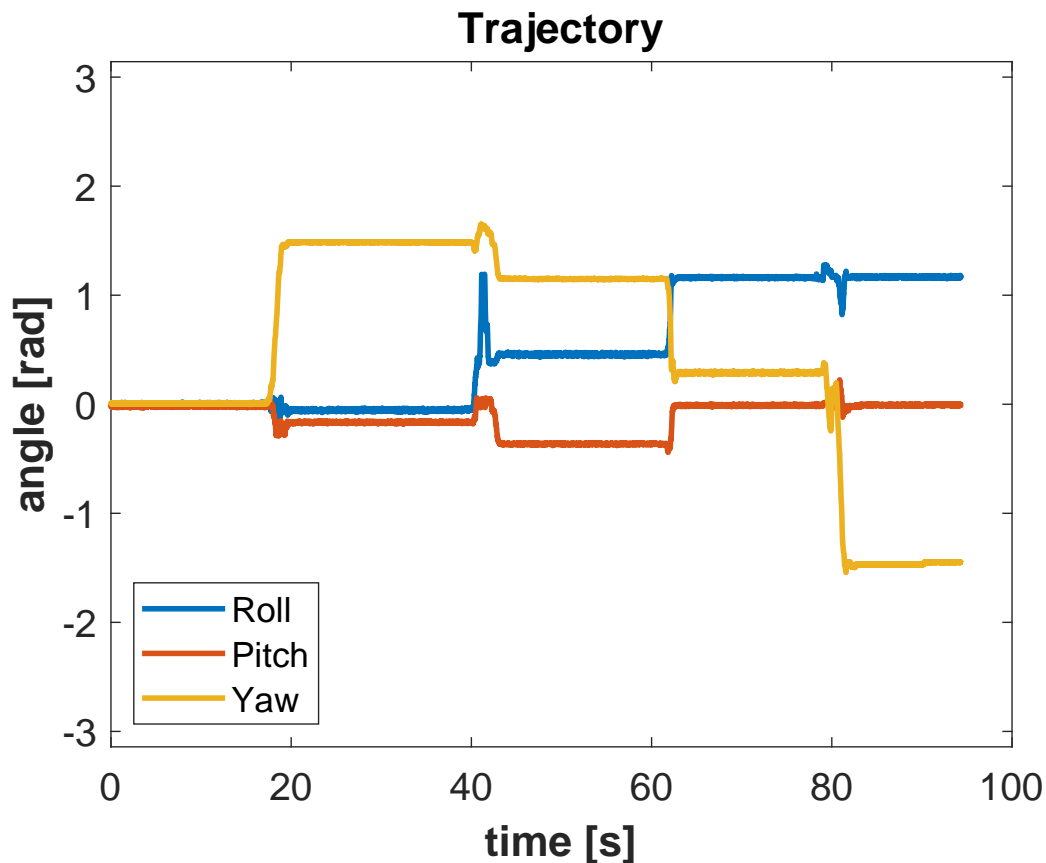


Fig. 3.21 Trajectory acquired from the acquisition used to solve the two-frame sensor problem.

value for compensation gains. For example, in Campolo filter we found how, augmenting the gyroscope noise, also the gains increase in order to weight more the signals coming from accelerometer and magnetometer.

The output error is very low, around 0.005 rad by mean, that is an important result which confirms how the tuning of gain parameters can drive through better performance.

In addition to this, can also be noticed how Tian filter has a drift, due to gyroscopes, differently from other filters. This effect suggests that there is a scope of improvement in the tuning of the filters' parameters.

In the end, in this trial, where we used synthetic data, the filters which give the best results are the gyroscope integration, the Madgwick and the Mahony filters. That is due to the low value of gyroscope noise, that is clearly shown by the low error in the gyroscope integration filter, which does not use an accelerometer and magnetometer compensation at all.

74 Performance evaluation of magneto-inertial motion units and sensor fusion algorithms

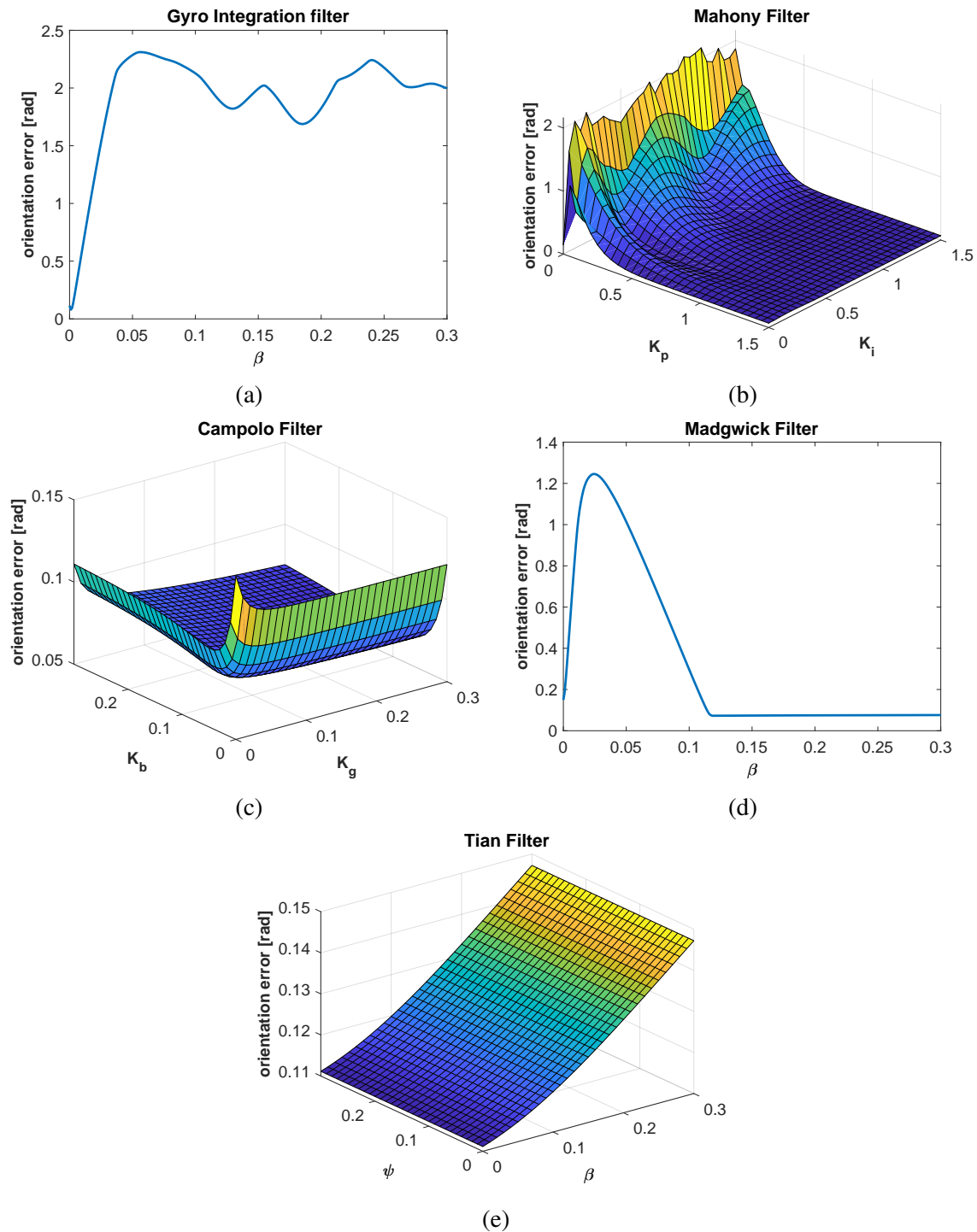


Fig. 3.22 Tuning of orientation filters using real M-IMU data. The value measured is the error angle (Equation A.19), expressed in *rad*, represents the displacement between the M-IMU sensor fusion filter algorithm and the ground truth. Figure 3.22a represents the gyroscope integration filter, Figure 3.22b is Mahony filter [51], Figure 3.22c is Campolo filter [74], Figure 3.22d is Madgwick filter [66] and Figure 3.22e is Tian [49].

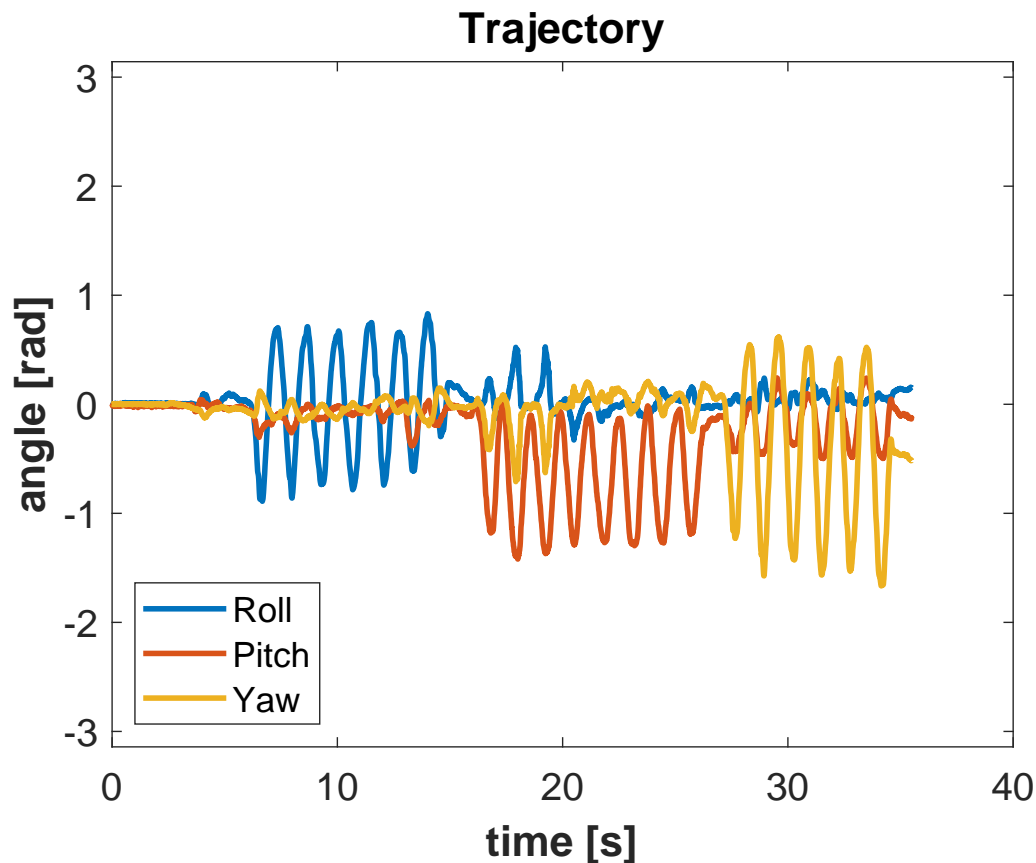


Fig. 3.23 Trajectory acquired from the acquisition used to evaluate filter performance.

For what it may concern the experiment which analyzes real data, we firstly tuned the data acquired to solve the two-frame sensor problem; secondly we performed the calibration in order to get X, Y matrices; finally we acquired another set of data, tuned the filters, and computed the errors.

The tuning of the parameters from real data (Figure 3.22 and Figure 3.24) yields due to gain values different from synthetic data, due to the variability of a real data with respect to the synthetic one. Filters with real data need more to compensate the drift due to gyroscope integration, using accelerometer and magnetometer data.

For what concerns the calibration error, shown in Figure 3.25, it is shown how all the complementary filters have a drift which witnesses for possible improvement in the tuning process.

The output error is low and guarantees good performance in each filter, as shown in Figure 3.26, that is lower than or around 0.1 rad . In particular the best result is given by Kalman filter developed by STMicroelectronics, where the error is $0.08 \pm 0.04 \text{ rad}$ expressed as mean and standard, with peaks of 0.23 rad . Of note, between the complementary filters

76 Performance evaluation of magneto-inertial motion units and sensor fusion algorithms

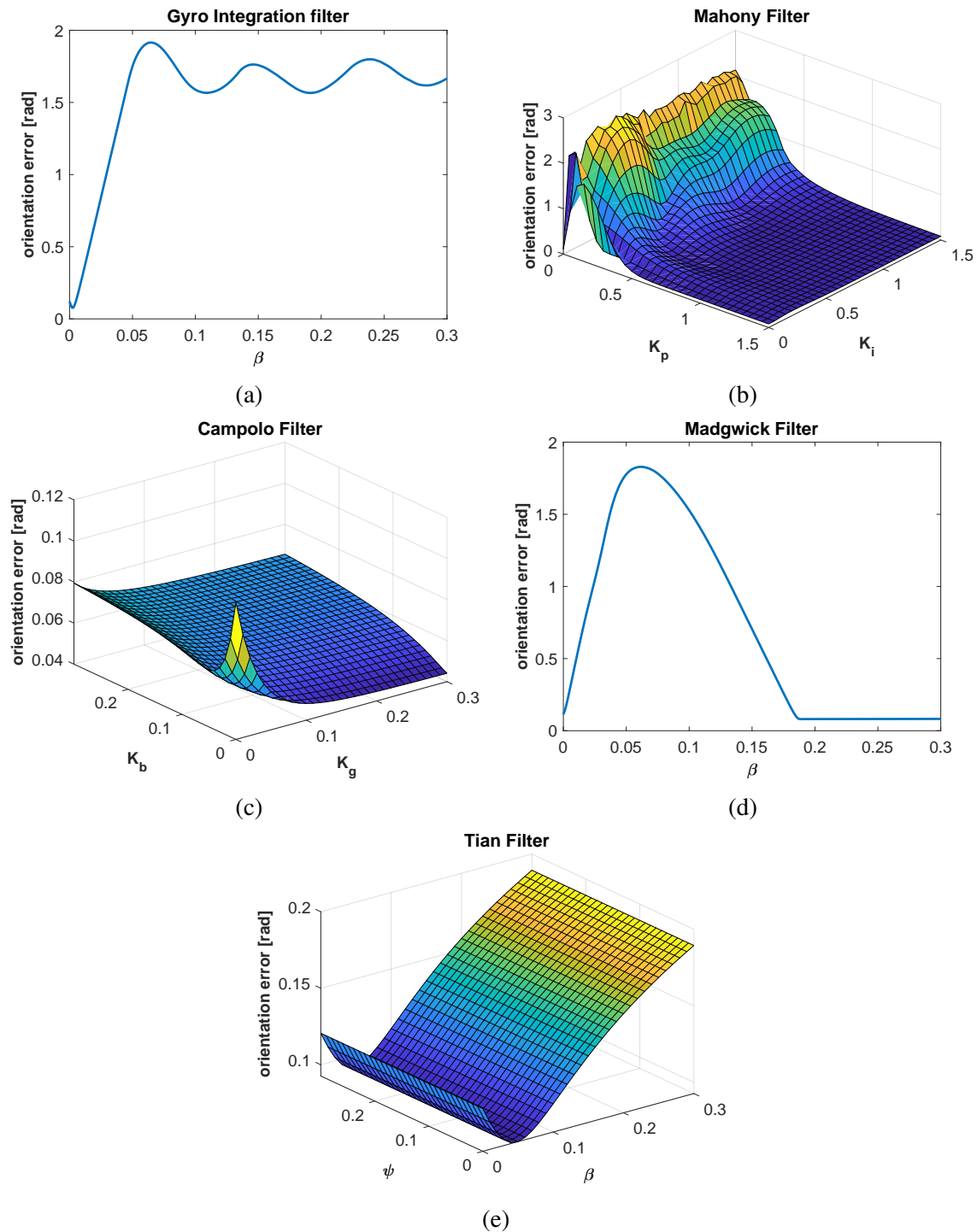


Fig. 3.24 Tuning of orientation filters using real M-IMU data. The value measured is the error angle (Equation A.19), expressed in *rad*, represents the displacement between the M-IMU sensor fusion filter algorithm and the ground truth. Figure 3.24a represents the gyroscope integration filter, Figure 3.24b is Mahony filter [51], Figure 3.24c is Campolo filter [74], Figure 3.24d is Madgwick filter [66] and Figure 3.24e is Tian [49].

Table 3.3 Error angle represented by mean \pm standard deviation and maximum peak value, computed with optimal gain parameters. Data acquired to solve two-frame calibration problem.

Filter	Gain value	error angle	Max peak
Kalman Filter ¹²	N.A.	0.0446 ± 0.0336 rad	0.4513 rad
Gyro integration [66]	$\beta = 0.0000$	0.1296 ± 0.0333 rad	0.4670 rad
Madgwick [66]	$\beta = 0.0000$	0.13076 ± 0.0341 rad	0.4732 rad
Mahony [51]	$K_p = 1.5000$ $K_i = 0.1500$	0.1164 ± 0.0295 rad	0.4289 rad
Campolo [74]	$K_g = 0.3000$ $K_b = 0.0000$	0.1279 ± 0.0517 rad	0.4667 rad
Tian [49]	$\beta = 0.0400$ $\psi = 0.2076$	0.1515 ± 0.0375 rad	0.4941 rad

Table 3.4 Error angle represented by mean \pm standard deviation and maximum peak value, computed with optimal gain parameters. Data acquired to evaluate filter's performance.

Filter	Gain value	error angle	Max peak
Kalman Filter ¹³	N.A.	0.0839 ± 0.04213 rad	0.2337 rad
Gyro integration [66]	$\beta = 0.0025$	0.1162 ± 0.0732 rad	0.3182 rad
Madgwick [66]	$\beta = 0.1891$	0.1243 ± 0.0648 rad	0.3219 rad
Mahony [51]	$K_p = 0.9000$ $K_i = 0.9000$	0.1024 ± 0.0554 rad	0.3130 rad
Campolo [74]	$K_g = 0.3000$ $K_b = 0.0000$	0.0939 ± 0.0453 rad	0.2470 rad
Tian [49]	$\beta = 0.0500$ $\psi = 0.2790$	0.1233 ± 0.0704 rad	0.3131 rad

the one developed by Campolo results to have the best performance, $0.09 \pm 0.04rad$ as error mean and standard deviation, and maximum peak values of equal to $0.25rad$.

Using these algorithms to get orientation filter, is also important to evaluate the computational time, shown in Table 3.5; this measure has been done in MATLAB, where the filters have been implemented. In this case the Campolo filter, the one with best performance also need the highest computational time, which has implications also in power consumption.

78 Performance evaluation of magneto-inertial motion units and sensor fusion algorithms

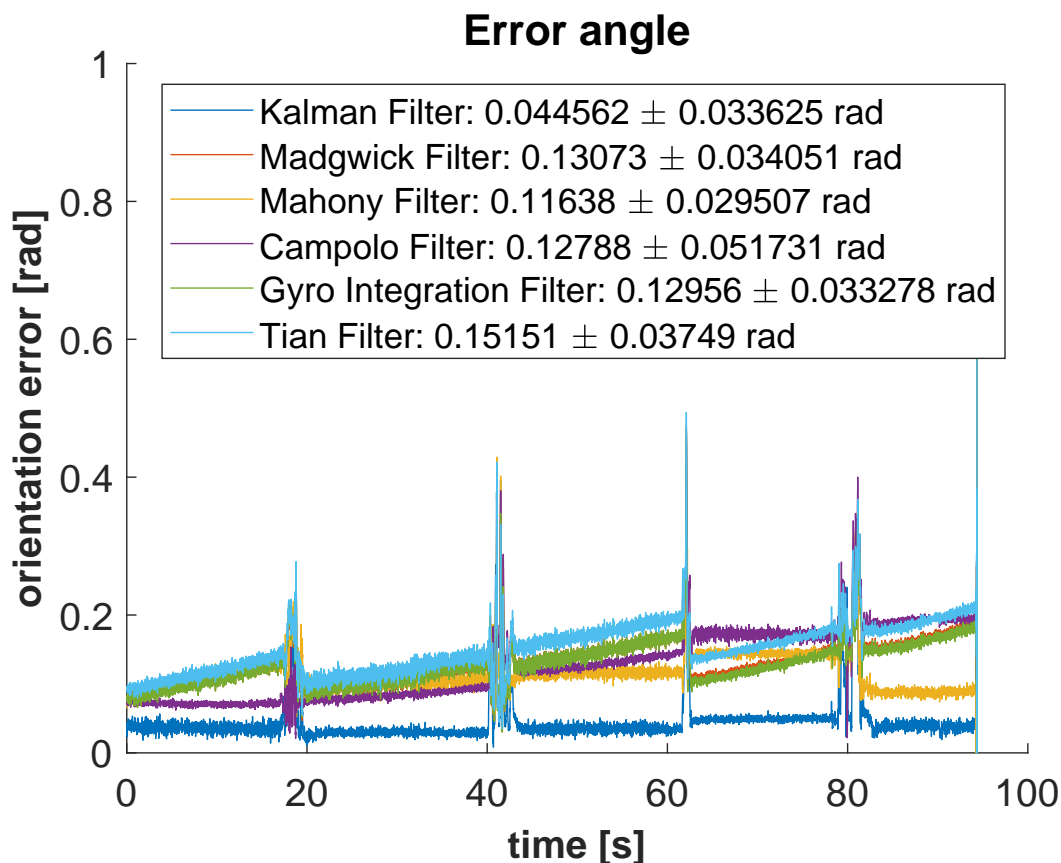


Fig. 3.25 Error angle computed per each filter on real data, using the optimal gain parameters for two-frame calibration error.

Another interesting improvement that may be done, in order to have a more complete analysis of the filters, is to modify the trajectory used to reduce the static part of the movement and understand the performance in relation to the speed and frequency in the motion. In fact, we tuned the sensor with low speeds and low frequency, that may improve the behaviour of the filter with a low dynamic behaviour, but decrease its performance in the dynamic. In fact, as can be seen in Figure 3.20, the error is close to zero in the static part of the motion, while the peaks are very higher during the movement.

As further improvement, it could be useful to create a database or also define some standard movement for filter tuning and assessment. In this way will be easier to test the performance of new filters and compare them with those already analyzed.

As a matter of fact, we suppose that can not probably exist a filter with a better behaviour regardless of the application. Hence, the idea is to design a standard method of analysis and a database of defined motions in order to evaluate the filter we want to use, in accordance with the application in which it will be implied on.

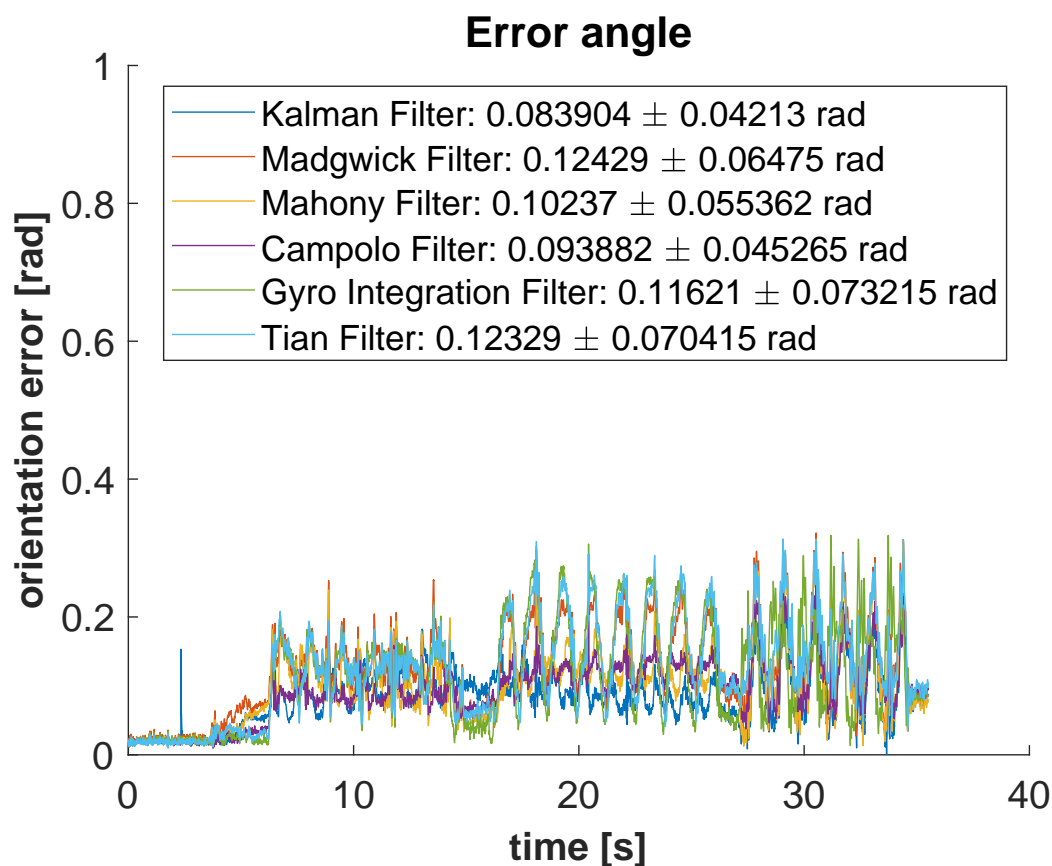


Fig. 3.26 Error angle computed per each filter on real data, with the optimal gain parameters used for filters performance evaluation.

Table 3.5 Computational time measured per each filter, expressed in μs

Filter	Computational time
Gyro integration [66]	28 μs
Madgwick [66]	66 μs
Mahony [51]	61 μs
Campolo [74]	109 μs
Tian [49]	109 μs

Tesi di dottorato in Bioingegneria e bioscienze, di Jacopo Tosi,
discussa presso l'Università Campus Bio-Medico di Roma in data 28/05/2019.
La disseminazione e la riproduzione di questo documento sono consentite per scopi di didattica e ricerca,
a condizione che ne venga citata la fonte.

Chapter 4

Use of M-IMUs for the assessment in neurological diseases

Citations:

- [J.II] Lazzaro di Biase, Susanna Summa, **Jacopo Tosi**, Fabrizio Taffoni, Massimo Marano, Angelo Cascio Rizzo, Fabrizio Vecchio, Domenico Formica, Vincenzo Di Lazzaro, Giovanni Di Pino, and Mario Tombini. Quantitative analysis of bradykinesia and rigidity in Parkinson's disease. *Frontiers in Neurology*, 9(MAR):121, 3 2018.
- [C.I] Susanna Summa, **Jacopo Tosi**, Fabrizio Taffoni, Lazzaro Di Biase, Massimo Marano, Angelo Cascio Rizzo, Mario Tombini, Giovanni Di Pino, and Domenico Formica. Assessing bradykinesia in Parkinson's disease using gyroscope signals. In *2017 International Conference on Rehabilitation Robotics (ICORR)*, pages 1556–1561, London, 7 2017. IEEE.
- [C.II] **Jacopo Tosi**, Susanna Summa, Fabrizio Taffoni, Lazzaro di Biase, Massimo Marano, Angelo Cascio Rizzo, Mario Tombini, Emiliano Schena, Domenico Formica and Giovanni Di Pino. Feature Extraction in Sit-to-Stand Task Using M-IMU Sensors and Evaluation in Parkinson's Disease. In *2018 IEEE International Symposium on Medical Measurements and Applications (MeMeA)*, pages 1–6. IEEE, 6 2018.

The final part of this work aims to use M-IMU to assess neurological diseases with motor disorders, such as Parkinson's disease (PD), from an objective point of view. It is crucial to evaluate and quantitatively describe patient's motor symptoms without the necessity of the physician. First, this chapter briefly describe PD, highlighting basic information such as the causes, the symptoms and the therapies that are used with the patients; second, we try to assess patient's motor symptoms, *e.g.* bradykinesia, with M-IMUs on different task defined in the UPDRS.

4.1 Parkinson's Disease: basic concepts

Parkinson's disease is a neurodegenerative brain disorder, with a slow but progressive evolution, caused by the depletion of the dopaminergic signal, due to the death of the 70% of the nerve cells sited in a specific part of the brain, called *Substantia Nigra*. It mainly affects the motor system and produces severe symptoms, including akinesia, rigidity, postural disorders, tremor, bradykinesia and gait impairment [83], but also loss of equilibrium which comports the risk of falling [84].

The prevalence of PD in industrialized countries is estimated at 0.3% of the entire population, with the 1% in people over 60 years old [85]. In Europe its prevalence is between 0.5 – 3.5% [86] for people over 65 years old and it is present in Italy with the highest incidence rate, that is equivalent to 250-700 cases per year each 100.000 people older than 65 years. Parkinson's disease is twice as common in men than in women in most populations, probably due to a protective effect of female sex hormones, a sex-associated genetic mechanism or sex-specific differences in exposure to environmental risk factor [87] [88].

With the disease progression, daily patients motor status starts to fluctuate between ON and OFF, *i.e.* to a status when the motor symptoms are adequately controlled by therapy, to a status when motor impairments are more evident. In order to control these motor symptoms changes, with a personalized and fine-tuned therapy, a precise clinical rating is needed, thus requiring periodic clinical visit.

The most common pharmacological therapy for PD consists in the administration of levodopa, which can reduce symptoms and restore motor abilities in patients [89].

The cardinal motor symptoms of PD patients are bradykinesia, resting tremor [90] [91] and rigidity [5] [92] [93] and are used as core feature for the diagnosis of parkinsonism. In particular, is fundamental the presence of bradykinesia as a slowness of movement and decrements in amplitude or speed (or progressive hesitations or halts) as movements are continued; in addition to this this first criteria needs to exist in combination with at least one of rigidity and/or rest tremor [6]. Bradykinesia is considered the most important and representative between the motor symptoms, and it is defined as slowness in the initiation of voluntary movement with progressive reduction in speed and amplitude of repetitive actions [93]. Following the definition of bradykinesia, the fatigability of speed and amplitude, is a core feature; however, this is not a simple feature to catch with clinical evaluation, but it can be detected through an instrumented quantitative evaluation. The most studied cardinal symptom, by means of sensors, is the tremor, and in the last years there are several studies that have explored the characteristics of PD tremor [94] [4] in order to allow differential diagnosis with other tremor syndromes [90], or simply to monitor fluctuations of this symptoms. Finally,

4.1 Parkinson's Disease: basic concepts

83

rigidity is the most challenging motor symptom, to measure in an objective way, and only few studies have explored the accuracy of instrumental evaluation of rigidity with different devices [4]. In addition to the cardinal motor features, a majority of patients with PD also have non-motor symptoms; those symptoms and their progression are shown in Figure 4.1.

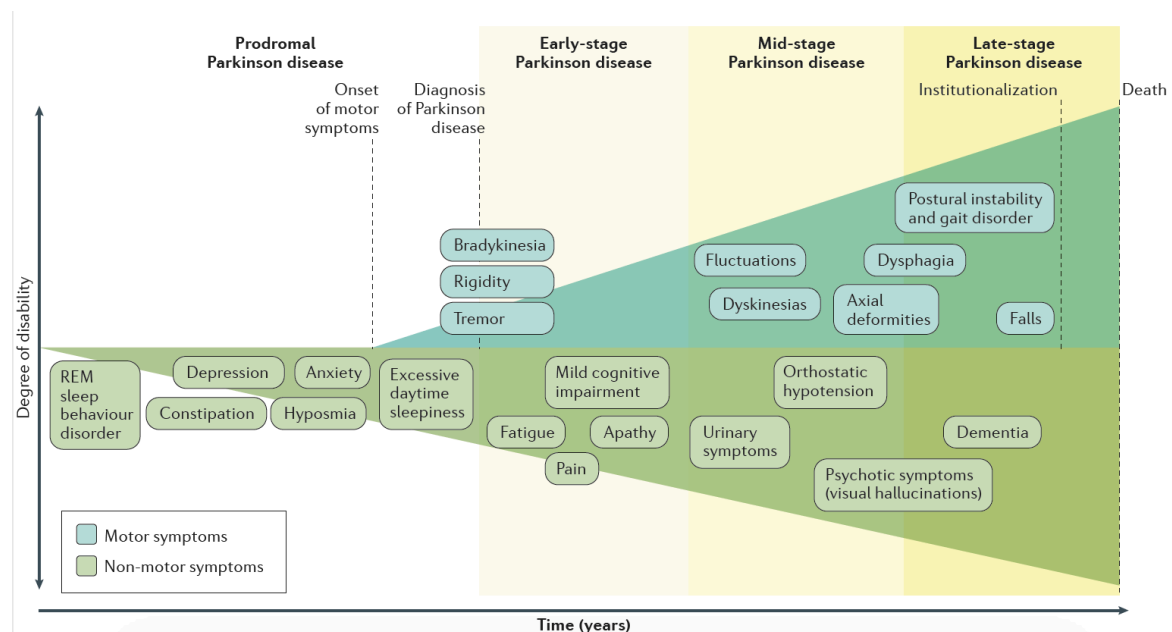


Fig. 4.1 Clinical symptoms associated with Parkinson's disease progression. Diagnosis of Parkinson disease occurs with the onset of motor symptoms (early-stage Parkinson disease) typically in the late fifties, but can be preceded by a prodromal phase of years or even decades, which is characterized by specific non-motor symptoms, such as REM, *i.e.* rapid eye movement (prodromal PD). Non-motor symptoms become increasingly prevalent and obvious over the course of the illness, but can be present to a variable degree throughout all stages of PD. Progressive disability from Parkinson's disease is driven by the combination of these non-motor problems with increasing severity of cardinal motor features, the development of L-dopa-induced motor complications (mid-stage PD) and the evolution of poorly L-dopa-responsive motor disabilities, such as postural instability, gait problems (including freezing), dysphagia (late-stage Parkinson disease) [6].

PD diagnosis, staging, and clinical grading, to date, rely on clinical observation by an expert neurologist. Moreover, clinical diaries can help to evaluate the global motor performance; however, they are affected by poor objectiveness [95], and low compliance. The most objective and standardized clinical evaluation available, is based on semiquantitative

scoring systems, by means of clinical rating scale like the Unified Parkinson's Disease Rating Scale (UPDRS) or also the more recent MDS-UPDRS sponsored by the Movement Disorder Society [96]. The MDS-UPDRS retains the UPDRS structure of four parts with a total summed score, but the parts have been modified to provide a section that integrates non-motor elements of PD: I, non-motor Experiences of Daily Living; II, Motor Experiences of Daily Living; III, Motor Examination; and IV, Motor Complications. All items have five response options with uniform anchors of 0 = normal, 1 = slight, 2 = mild, 3 = moderate, and 4 = severe [96]. There is also another clinical scale used to classify PD gravity and describes the different stages of disease, the Hoenn and Yahr scale [97].

4.2 Assessment of Parkinson's disease by means of a wearable M-IMU network

To date, using current diagnostic criteria [93], even for a neurologist expert of movement disorders, the error rate in the diagnostic accuracy can be estimated around 20% [98]. The most relevant problems related to PD clinical evaluation are that: it is a time-consuming activity; it is not objective; to make it reliable, an expert of movement disorders is needed; it is not remotely administrable. All these issues lead to high direct and indirect cost for the health system and for the patients.

Medical applications, for example, paid a growing attention to human motion caption systems to obtain more efficient rehabilitation therapies [99] [100], and to build monitoring networks for patients and elderly people in the hospitals and in their own homes [101].

In the last decades, several studies showed that wearable sensors, used for assessing Parkinson's Disease motor symptoms and recording their fluctuations, could provide a quantitative and reliable tool for patient's motor performance monitoring. In particular, the spread of low cost and non-invasive technologies for motion analysis, such as magneto-inertial wearable devices, brings to new methods for the assessment of pathologies characterized by motor dysfunction. Modern technologies like wearable sensors can provide a non-invasive, accurate, rapid, remote, low cost, operator independent, objective, and scalable system. The idea to monitor pathological motion deficits using wearable sensors dates back to 1950s [102], and its application for PD patients started in 1990s [103]. Although their clinical use is not so common yet, wearable M-IMUs are largely used with the purpose of measuring movement and physiological signals [104] [105] [106]. However, further work is needed to validate these systems and bring them to the everyday clinical practice.

To ensure proper monitoring of PD motor symptoms, a wearable system must be able to discriminate healthy subjects (HS) from PD patients, as well as to differentiate the ON from the OFF motor status in PD patients.

In this part of the work we try to do a step forward in the assessment of PD's motor symptoms using M-IMUs, in particular we investigate rigidity and bradykinesia in two different configurations:

- the first configuration aims to measure bradykinesia and rigidity by mean of M-IMUs applied on the most affected upper arm. We evaluate three tasks of the MDS-UPDRS part III, *i.e.* rigidity (task 22), finger tapping (task 23) and prono-supination movements of the hands (task 25).
- the second analysis mainly consists in a feature extraction specifically from the sit-to-stand task of MDS-UPDRS part III (task 27). In this configuration, M-IMUs are distributed on the whole body, acquiring data from all the four limbs, the trunk and the waist.

4.2.1 Upper limb monitoring for quantitative analysis of bradykinesia and rigidity in Parkinson's disease

M-IMUs have already been used for the assessment of PD through the measurement of motor data from the upper limb [107] [108]. These authors suggest that accelerometers and gyroscopes are suitable for monitoring motor symptoms in PD.

An example of a portable device is an instrumented glove used to quantify motor symptoms, during deep-brain stimulation surgery [105]; they used only a 6-axes IMU placed on the middle finger for tremors and bradykinesia assessment. The authors chose five UPDRS motor tasks, but that involve only the upper arm (*i.e.* rest tremor, postural tremor, finger-to-nose, repeated hand movements and rigidity). Experimental results showed that their system is reliable for tremor amplitude determination and movement angles measurement only. Such a similar device has also been proposed by [91].

A network of uniaxial accelerometers, four located on the upper limbs and four on the lower limbs has been proposed by [107]. Data were acquired during the execution of motor tasks that belong to the MDS-UPDRS scale, including finger-to-nose, finger tapping, repeated hand movements, heel tapping, sitting and alternating hand movements. The results indicated that it is possible to reliably estimate clinical scores on the basis of four feature that are: the root mean square value of accelerometers, the data range value of accelerometers, the dominant frequency and the ratio of energy of the dominant frequency component to the total

energy. Although differences were observed, several motor tasks performed equally well. That suggests the proposed accelerometer features capture aspects of the movement patterns that are not specific for a given motor task; it further suggests that the proposed analyses could be extended to activities of daily living.

Similarly, Heldman et al. [106] used two 6-axes motion sensors positioned on the index finger and thumb, but they analyzed only the gyroscope signals. They tested PD patients in OFF and ON states, while performing only bradykinesia tasks, *i.e.* finger tapping, hand grasping and prono-supination of arms. Looking at the comparison with kinematic measures, they found that the log of root mean square of the angular velocity better correlates with the MDS-UPDRS scores concerning speed; the root mean square of the excursion angle correlates closely with scores concerning amplitude; the coefficient of variation correlates closely with rhythm scores. Their results suggest that motion sensors can objectively measure speed, amplitude, and rhythm and they are highly correlated with clinician scores.

The good correlation with the clinical score reported these studies encourages the use of a wide number of parameters. Interactive motor tasks, recorded using M-IMUs, worn by subjects, allowed to deeply analyze the kinematic and dynamic characteristics of goal-directed movements of upper limb, in addition to the extraction of quantitative and useful indices for the motor symptoms evaluation.

Therefore, one objective of this work is to go one step forward in the capability of quantitatively describe PD motor symptoms. In particular, our primary aim is to find few simple parameters to monitor bradykinesia and rigidity, as it has already and largely been done for tremor. We also aim at pointing out the advantages and limitations of such technologies with respect to the validated clinical scales.

Moreover, in literature, among studies focused on the use of wearable sensors in PD, there is a lot of variability about the body distribution of sensors and about the specific indexes used to sense cardinal motor symptoms.

In conclusion, the aims of the present study are: identify the most sensible place where to locate sensors to monitor PD bradykinesia and rigidity; identify objective indexes able to discriminate PD patients from HS, and able to differentiate PD patients in ON from OFF motor status.

Subjects

Fourteen PD patients (Table 4.1) (8 males, age: 67 ± 6 years) were enrolled in the study to evaluate bradykinesia and rigidity. Inclusion criteria for PD patient group were: a possible-probable diagnosis of PD according to UK PD Brain Bank criteria [93] and an Hoen and Yahr stage [97] between 1 and 2.5. Exclusion criteria for PD patient was Hoen and Yahr

stage higher than 2.5; for both PD and HS group, another exclusion criteria was limitation of the physiological joints range of motion caused by other pathologies.

Thirteen age-matched healthy subjects composed the control group (seven males, age: 69 ± 19 years).

The research has been carried out in accordance with the Declaration of Helsinki. All patients and control subjects gave informed consent and the study was approved by local research ethics committee.

For PD group patients, kinematic analysis has been performed for the most affected arm. For the HS group, the kinematic analysis has been done on dominant arm, identified with the Oldfield test [109].

Parkinson's disease subjects were analyzed twice: after 12 h withdrawal of any medications (OFF motor condition) and after 1 h from administration of 150% of patient's l-dopa morning dose (ON motor condition).

Motor tasks

Subjects were sitting in a chair and were asked to perform three motor tasks from the UPDRS part III.

Rigidity (UPDRS task 22) has been tested, without an activation maneuver, on slow passive movement of elbow joints, with the patient in a relaxed position. During this task, the examiner, holding the arm against gravity, moves the forearm 10 times for each side.

Bradykinesia has been evaluated performing two tasks: finger tapping (UPDRS task 23) and prono-supination movement of the hands (UPDRS task 25). During the finger-tapping task, subjects were asked to tap the index finger on the thumb 15 times as quickly and as big as possible; each side has been evaluated separately. During the prono-supination task, it has been asked to subjects to extend the arm out in front of them with the palms down; then to turn the palm up and down alternately 15 times as fast and as fully as possible.

A movement disorders expert rated the three tasks according to the UPDRS part II scoring scale.

Data acquisition

In order to identify the most informative parameters to describe PD motor symptoms, motor tasks have been recorded using five commercial magneto-inertial measurement units called Opal, by APDM Inc. (Portland, OR, USA). This sensor provides the value of acceleration ($\pm 16g$), angular velocity (± 2000 deg/s), the intensity of the magnetic field (± 8 Gauss) and the quaternions, computed via the manufacturer's Kalman filter. Its sampling frequency is 128

Table 4.1 Parkinson's disease patients characteristics. The columns represent an ID unique per each patient; the time since the disease has been started, measured in years; the gender, where M stands for male and F for female; the dominant hand, defined with the Oldfield test [109]; the side most affected by PD; the LEDD, *i.e.* the levodopa equivalent daily dose, measured in mg; and the UPDRS part III score, measured in OFF condition. NA stands for not applicable.

ID	Duration	Gender	Dominant hand	PD side	LEDD	UPDRS (OFF)
S1	10	M	Right	Right	750	45
S2	5	M	Right	Left	750	29
S3	9	F	Right	Left	950	29
S4	7	F	Right	Right	660	36
S5	21	F	Right	Left	660	29
S6	10	M	Right	Right	925	65
S7	4	F	Right	Left	550	23
S8	NA	M	Left	Left	NA	49
S9	7	M	Right	Right	700	20
S10	2	F	Right	Right	300	25
S11	7	F	Right	Left	1.150	29
S12	6	M	Right	Left	600	25
S13	10	M	Right	Left	700	27
S14	7	M	Right	Right	670	43

Hz and the A/D has a 16-bit resolution. These specific sensors have already been validated in detail by Ricci et al. in [3].

All the acquisitions were recorder with a camera, the GoPro Hero4 Silver (GoPro, San Mateo, CA, USA). The GoPro camera uses a 800x480 video format with a frame rate of 120 fps.

The data were acquired with MotionStudio software by APDM Inc. (Portland, OR) which sends a trigger to the camera in order to synchronize it with the Opal sensors.

The experiments have been performed positioning sensors on the following anatomical landmark: second phalanx of the index finger (with the sensor X-axis in line with the same bone), distal phalanx of thumb (with the sensor X-axis in line with the same bone), metacarpus (fixed at medium point of third metacarpal bone, on the dorsal metacarpus, with the sensor X-axis in line with the third metacarpal bone), wrist (fixed at the medium point

between radius and ulna bones, on the most distal dorsal part of radius and ulna bones, with the sensor X-axis in line with the radius bone), and arm (fixed at medium point between the greater tubercle of the humerus and its lateral epicondyle, with the sensor X-axis in line with the humerus). The setup described here above is showed in Figure 4.2.

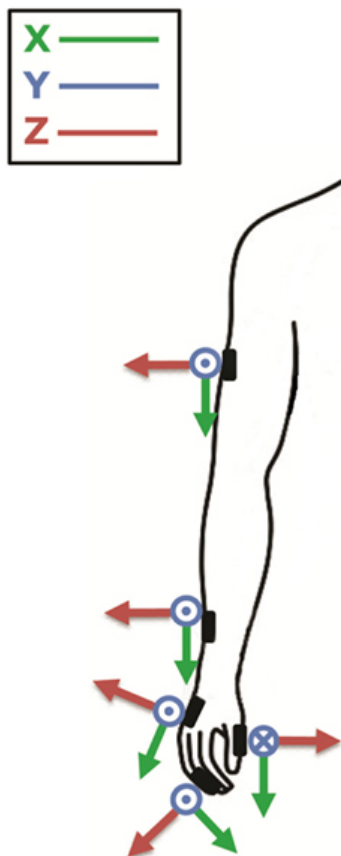


Fig. 4.2 The figure shows position of each M-IMU on the upper limb and their orientation. Adapted from [92].

Data analysis

According to literature [105] [107], raw data are first high-pass filtered with a cut-off frequency of 1 Hz, to remove the effect of gross changes in the orientation of body segments. Moreover, the frequency component of interest for estimating each symptom can be isolated; specifically for tremor, a bandpass filter with bandwidth 4-8 Hz has been used, while for bradykinesia data are band passed between 1-4 Hz.

In the task used to assess bradykinesia severity, we defined a movement cycle as the set of submovements needed to complete the task for one repetition. For instance, a finger-tapping cycle consists of starting with the hand opened, closing, and then opening the fingers again to

the initial position for one time. We estimated the movement time as the interval between the beginning and end of cycles, identified from the speed profile with a threshold of 10% of the peak value of each cycle. In addition to this, we calculate the total time needed to complete the full task as

$$t_{TOT} = t_b - t_a \quad (4.1)$$

In summary, total time (t_{TOT}) is the difference between the end time (t_b) of the last cycle and the beginning of the first cycle (t_a).

From gyroscope signals in the time domain, we estimated the peak-to-peak values of angular velocity for all three axes. In order to capture the progressive reduction in speed amplitude, we perform a first-order regression between these peak-to-peak values and the progressive number of cycles. We defined the fatigability index as the slope of the fitted linear equation computed from the peak-to-peak values of angular velocities extracted from the gyroscope signals.

Of note, for what it concerns the fatigability index, we consider for each task only the gyroscope axis most relevant for that specific task.

As regards the frequency domain, we extract the total power (the integral of the power spectrum) from the power spectrum density (PSD) of angular velocity as suggested by Kim et al. [108]. In fact, one of the results of Fourier analysis is the Parseval's theorem, which states that the area under the energy spectral density curve is equal to the area under the square of the magnitude of the signal, *i.e.* the total energy. A similar result holds for power; the total power is expected to represent the overall intensity of movement.

We also introduce a smoothness parameter as a bradykinesia descriptor. According to previous studies [110] [111], we measure smoothness using the spectral arch length (SAL) of movement speed profile as an appropriate index of movement fluidity, as shown in Figure 4.3. We decide to look at this type of smoothness measure because Balasubramanian et al. [110] showed that the SAL can account for the change in the number of submovements and the inter-submovement interval, which are movement features influenced by bradykinesia. As explained by the authors [110] [111], to compute smoothness it has not been necessary to filter data because of the inherent low-pass filtering action performed. Specifically, we compute the SAL within the frequency range 0-4 Hz of the speed profile in each movement cycle and in each single movement.

Spectral arch length estimates smoothness by calculating the arch length of the magnitude of the Fourier Spectrum of a given speed profile $v(t)$, with a frequency range $(0 - \omega - c)$, showed in Equation 4.2.

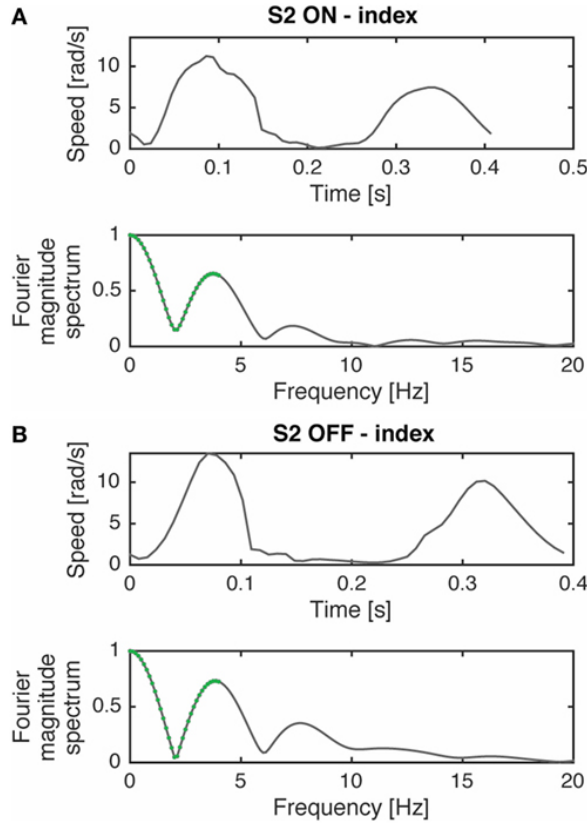


Fig. 4.3 Movement speed profile during prono-supination task of a typical subject (S2) in ON (A) and OFF (B) phases and their respective Fourier magnitude spectrum. The segments used for computing spectral arch length are highlighted in green. The complexity of the Fourier magnitude spectrum changes with the submovement characteristics variations (*i.e.* inter-submovement interval) of the movement speed profile, as already shown by [110]. Adapted from [92].

$$SAL \triangleq \int_0^{\omega_c} \left[\left(\frac{1}{\omega_c} \right)^2 + \left(\frac{d\hat{V}(\omega)}{d\omega} \right)^2 \right]^{\frac{1}{2}} d\omega; \quad \hat{V}(\omega) = \frac{V(\omega)}{V(0)} \quad (4.2)$$

where $V(\omega)$ is the magnitude of the Fourier spectrum of $v(t)$; $\hat{V}(\omega)$ is the spectrum magnitude normalized with respect to the magnitude at zero frequency $V(0)$, and ω_c is adaptively selected, based on the following equation.

$$\omega_c \triangleq \min\{\omega_c^{max}, \min\{\omega, \hat{V}(r) < \bar{V} \forall r > \omega\}\} \quad (4.3)$$

Equation 4.3 defines ω_c as the minimum value between: (i) an upper bound limit for this parameter ω_c^{max} , which has been set in our analysis to 4 Hz; (ii) the value of frequency above

which the normalized spectrum magnitude is always lower than a given threshold \bar{V} , set in our analysis to 10%.

The definition of the SAL modified with the adaptive parameter ω is referred in the literature as the SPARC index [111].

Finally, we investigate the relationship between this index and the elbow joint rigidity and we test the smoothness index as rigidity descriptor. In PD, the classic cogwheel rigidity causes a fragmentation and decomposition of the passive movement, leading to less smooth than normal passive movements. We estimate the beginning and the end of movement looking at the speed profile with a threshold of 10%. Then, we compute the averaged SAL of movement speed profile for each movement and look at differences between OFF and ON motor statuses. Specifically, we computed the SAL within the frequency range 0-20 Hz of the speed profile in each movement cycle.

Statistical analysis

First, we look for normality of distributions with the Shapiro-Wilk test, because of the number of participants in each group [112].

As mentioned previously, we are investigating those indexes able to differentiate the OFF motor status from the ON one in PD patients; moreover, we want to identify the most sensible place where to locate sensors. Therefore, for each indicator we conduct two-way repeated measures ANOVA with state (ON vs OFF) and sensors locations - 5 levels in bradykinesia tasks (arm, index, metacarpus, thumb, and wrist) - as within-subjects factor, that is the multiple comparisons of the interactive effect state \times sensor location.

For OFF vs HS discrimination, data are analyzed using a mixed-design ANOVA with a within-subjects factor sensor location and a between-subject factor the group (OFF or HS). For ON vs HS discrimination, we run a mixed-design ANOVA with a within-subjects factor sensor location and a between-subject factor the group (ON or HS). We additionally assessed the most sensible place where to locate sensors while discriminating the group factor, that is the multiple comparisons of the interactive effect group \times sensor location.

In order to identify the most sensible place where to locate sensors, to monitor PD bradykinesia and rigidity, while excluding false-positive results under multiple testing, we apply Bonferroni correction, and p -values are compared against α divided the number of comparisons, instead of $\alpha = 0.05$.

For total time index, we use a paired-sample t -test to test its capability to differentiate the ON vs OFF motor status. Similarly, we used an independent sample t -test to see if total time index is capable to discriminate HS from the OFF or from the ON status.

We also look at the correlation of each indicator in the OFF and ON conditions, with the UPDRS part III scale. Correlation has been reported as *R*-squared values.

For data analysis Matlab (Mathworks, Natick MA, USA) has been used.

Results

The results of clinical rating with UPDRS part III scale, for each task are shown in Table 4.2 and Table 4.3, respectively for bradykinesia and rigidity task.

Table 4.2 Bradykinesia tasks clinical rating. In this table it is shown the UPDRS score of task 23 and 25 of UPDRS part III, *i.e.* finger tapping and arm prono-supination.

Subjects	UPDRS part III score			
	Task 23: finger tapping		Task 25: arm prono-supination	
	OFF	ON	OFF	ON
S1	3	3	2	2
S2	2	1	1	1
S3	1	0	1	0
S4	2	1	2	1
S5	1	1	1	1
S6	3	2	4	4
S7	1	0	1	0
S8	3	2	2	2
S9	2	1	1	1
S10	1	1	1	1
S11	2	1	1	0
S12	2	1	2	1
S13	1	1	1	1
S14	3	2	1	1

Parkinson's disease patients S13 and S14 were excluded from the kinematic analysis due to artifacts into accelerometrics signal.

First of all, we look at the total time needed to complete the finger-tapping and the arm prono-supination tasks. In the OFF condition, PD subject needed more time to complete the task than during the ON condition. Considering the arm prono-supination task, statistical analysis showed that the total time is able to discriminate the OFF vs ON motor condition (*p*

Table 4.3 Rigidity task clinical rating. In this table it is shown the UPDRS score of task 22 of UPDRS part III, *i.e.* the measurement of the rigidity of the arm.

Subjects	UPDRS part III score, task 22			
	Right arm rigidity		Right arm rigidity	
	OFF	ON	OFF	ON
S1	2	2	2	2
S2	2	1	2	1
S3	2	2	2	2
S4	2	1	1	1
S5	2	1	2	2
S6	2	2	2	2
S7	1	0	1	1
S8	2	2	3	2
S9	0	0	0	0
S10	2	1	2	1
S11	1	1	2	1
S12	1	1	2	2
S13	1	1	2	1
S14	2	2	1	1

= 0.01) and also to differentiate the HS group from PD patients in OFF and ON conditions (OFF $p = 0.001$; ON $p=0.04$), showed in Figure 4.4A. Regarding the finger-tapping task, the total time is able to discriminate the OFF vs ON motor condition ($p=0.001$) and also to differentiate th HS group from PD patients in OFF condition ($p=0.02$), as shown in Figure 4.4B. Good correlations have been found in the finger-tapping task, between total time and UPDRS item 23 score, for both motor conditions (ODD $R^2 = 0.34$; ON $R^2 = 0.74$). No correlation has been found between total time and UPDRS item 25 score in arm pronosupination task.

To catch the whole kinematic information, related to the task performed, it is important to consider where to place the sensor and which orientation axis to use for the analysis. For finger tapping task, the x-axis has been the most informative (Figure 4.5). Therefore, we look also at the fatigability on these two axes depending on the task (Table 4.4 and Table 4.5).

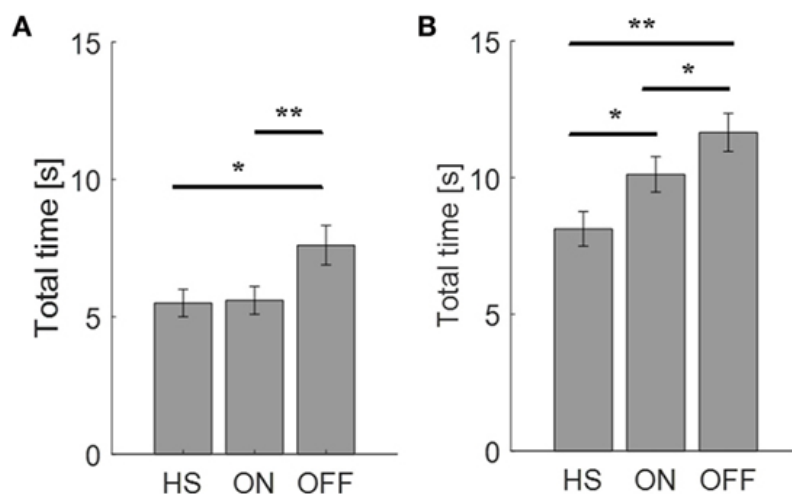


Fig. 4.4 Total time needed, measured in second to complete the finger-tapping (A) and the arm pronation-supination tasks (B). Values are averaged for each group. Bars denote the Standard Error (SE). The symbol * represents a $p < 0.05$; ** represents $p < 0.01$ (t -test).

Table 4.4 Finger-tapping task kinematic results. The symbol * represents $p < 0.05$; ** is $p < 0.01$ (ANOVA). Sensor location is referred to the index finger.

	Kinematic index		
	Fatigability	Total power	Smoothness
State (PD ON vs PD OFF)		**	**
Sensor location		**	**
State (ON/OFF) \times sensor location		**	
State (PD OFF vs HS)		**	**
Sensor location		**	**
State (OFF/HS) \times sensor location		**	
State (PD ON vs HS)			
Sensor location		**	**
State (ON/HS) \times sensor location		*	

The fatigability index assessed in the finger-tapping and arm pronation-supination tasks are shown, respectively, in Figure 4.6 and Figure 4.7. As mentioned before, the fatigability represents the progressive reduction in speed of the movement, as shown in Figure 4.5.

Analyzing the finger-tapping task, the ANOVA shows no significant main effect of the state in none among the three states comparison; *i.e.* ON/OFF, OFF/HS, and ON/HS on fatigability index (Figure 4.6).

Table 4.5 Prono-supination task kinematic results. The symbol * represents $p < 0.05$; ** is $p < 0.01$ (ANOVA). Sensor location is referred to the index finger.

	Kinematic index		
	Fatigability	Total power	Smoothness
State (PD ON vs PD OFF)	**	**	**
Sensor location	**	**	**
State (ON/OFF) × sensor location	**	**	
State (PD OFF vs HS)		**	**
Sensor location	**	**	**
State (OFF/HS) × sensor location		**	
State (PD ON vs HS)	*	**	**
Sensor location	**	**	**
State (ON/HS) × sensor location		**	

Analyzing the arm prono-supination task, there is a significant main effect of ON/OFF state [$F(1) = 9.899$; $p = 0.009$] and of sensor location [$F(4) = 8.548$; $p < 0.001$] on fatigability index. There is also a significant interaction between ON and OFF states and sensor location on fatigability index [$F(4) = 3.957$; $p = 0.008$].

The *post hoc* test, showed the following sensors significance, thumb $p = 0.003$; wrist $p = 0.006$.

There has been no significant effect of OFF/HS states on fatigability index, there has been a significant main effect of sensor location on this index [$F(4; 92) = 3.556$; $p = 0.01$] and there has been no interaction between OFF/HS status and sensor location on this index.

In addition to this, there has been a significant main effect on ON/HS states [$F(1; 23) = 5.76$; $p = 0.025$] and of sensor location [$F(4; 92) = 3.556$; $p = 0.01$] on this index. There has been no interaction between ON/HS conditions and sensor location on fatigability index. *Post hoc* analysis showed no statistically significant differences among sensors.

We found a good correlation between the UPDRS item 23 score and the fatigability measured in the finger-tapping task but only in the OFF condition for the index finger ($R^2 = 0.49$). no correlation has been found between the fatigability and UPDRS item 25 score in arm prono-supination task.

Power spectral density in PD subject in ON phase increases in amplitude compared with the one in OFF phase, as shown in Figure 4.8.

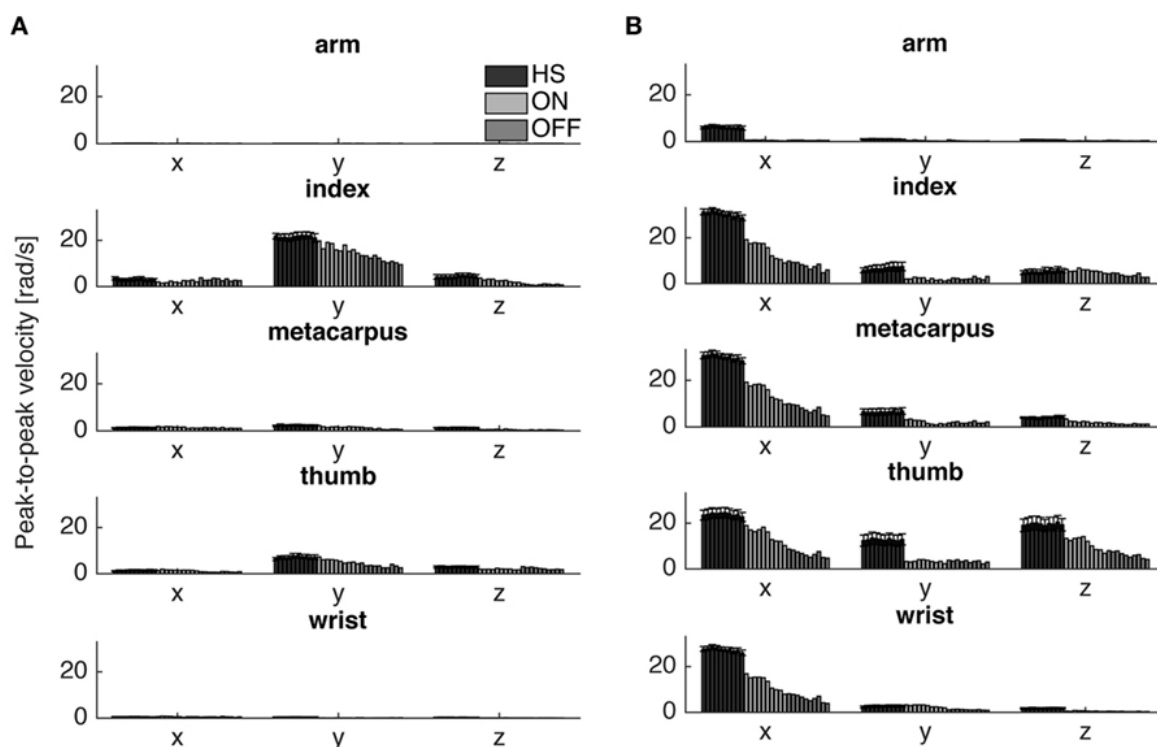


Fig. 4.5 Peak-to-peak velocity of all cycles of a typical Parkinson's disease subject (S6) in a comparison with the averaged values of a healthy subject (HS) group, relative to finger-tapping (A) and the arm pronosupination tasks (B) for each gyroscope channel. Values HS group values are averaged and bars denote the SE.

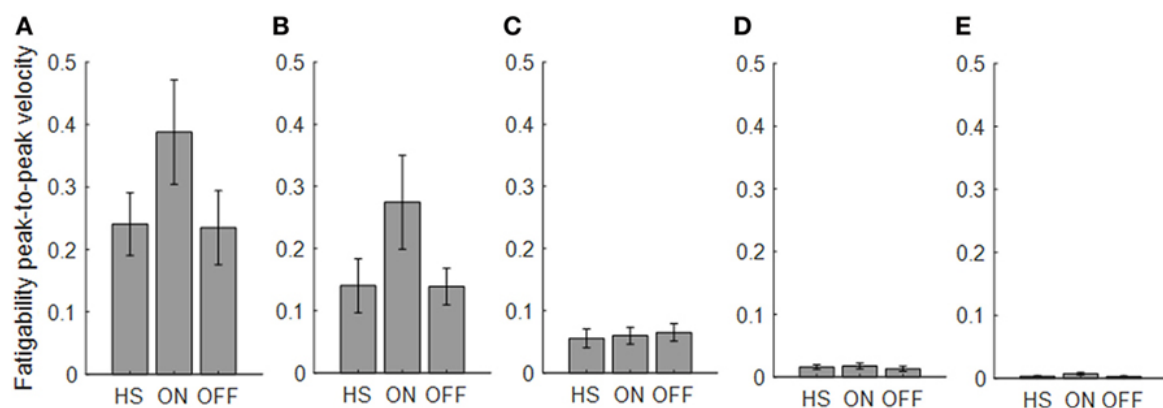


Fig. 4.6 Fatigability index computed in the finger-tapping task. Each panel shows the averaged values for each group, *i.e.* OFF, ON, and HS for index finger (A), thumb (B), metacarpus (C), wrist (D), and arm (E). Bars denote SE.

For the finger-tapping task (Table 4.4), there is a significant main effect of ON/OFF state [$F(1) = 14.047$; $p = 0.003$] and of sensor location [$F(4) = 47.709$; $p < 0.001$] on total power index, with a significant interaction between ON/OFF status and sensor location on this

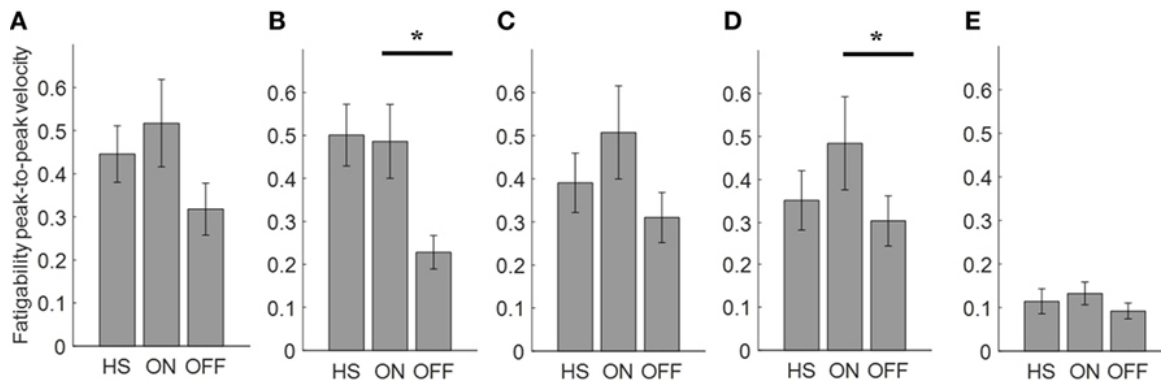


Fig. 4.7 Fatigability index computed in the arm pronosupination task. Each panel shows the averaged values for each group, *i.e.* OFF, ON, and HS for index finger (A), thumb (B), metacarpus (C), wrist (D), and arm (E). Bars denote SE. Bonferroni correction $*p < 0.01$.

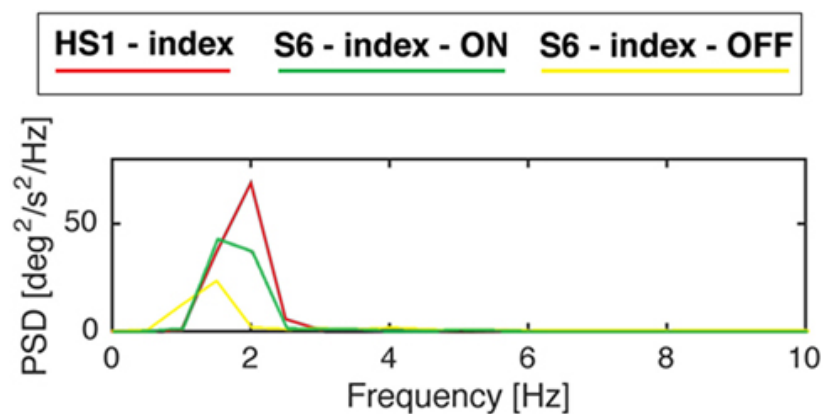


Fig. 4.8 Power spectral density of gyroscope signal of subjects S6 from the Parkinson's disease group and S1 from the HS group, while performing finger-tapping task. Adapted from [92].

index [$F(4) = 16.786$; $p < 0.001$] (Table 4.4). *Post hoc* analysis showed the following sensors location significance, index finger $p = 0.001$ (Figure 4.9).

ANOVA analysis shows a significant main effect of OFF/HS [$F(1; 23) = 16.247$; $p < 0.001$] and of sensor location [$F(4; 92) = 82.576$; $p < 0.001$] on total power index, with a significant interaction between OFF/HS and sensor location on this index [$F(4) = 15.946$; $p < 0.001$]. *Post hoc* analysis showed the following sensors' location significance, index finger $p < 0.001$ (Figure 4.9).

There has been no significant effect of ON/HS on total power index, during the finger-tapping task.

In this task, the correlation between total power and the UPDRS item 23 score in OFF motor condition is good for the index finger ($R^2 = 0.57$) and the thumb ($R^2 = 0.47$).

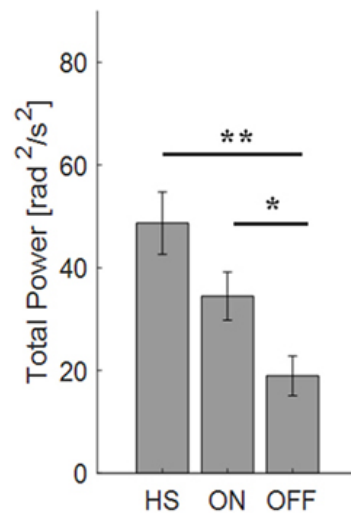


Fig. 4.9 Total power index computed in the finger-tapping task, with sensor on index finger. Values are averaged for each group OFF, ON, and HS. Bars denote the SE. Bonferroni correction $*p < 0.01$; $**p < 0.001$.

If we use the arm prono-supination to assess bradykinesia (Figure 4.10), it is possible to discriminate OFF vs ON motor status, OFF vs HS, and ON vs HS group (Table 4.5).

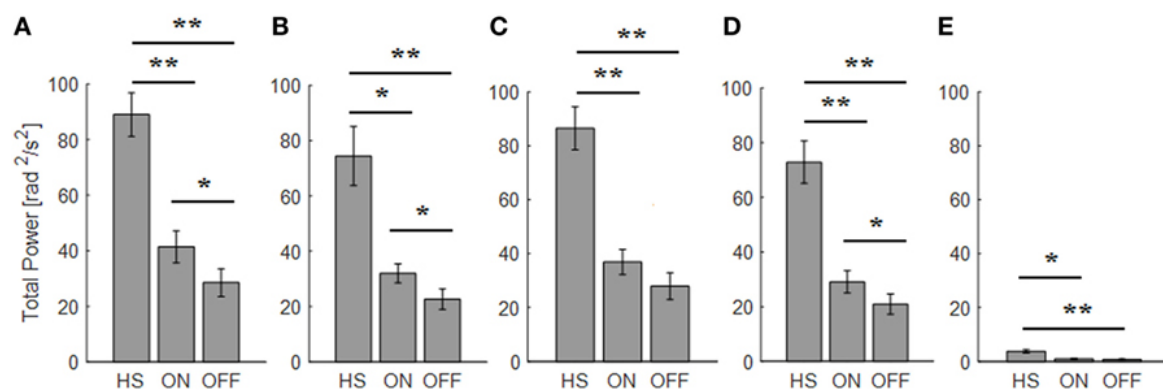


Fig. 4.10 Total power index computed in the arm prono-supination task. Each panel shows the averaged values for each group OFF, ON, and HS for index finger (A), thumb (B), metacarpus (C), wrist (D), and arm (E). Bars denote the SE. Bonferroni correction $*p < 0.01$; $**p < 0.001$.

There has been a significant main effect of ON/OFF state [$F(1) = 16.087$; $p = 0.002$] and of sensor location [$F(4) = 33.45$; $p < 0.001$] on total power index, with a significant interaction between ON/OFF state and sensor location on this index [$F(4) = 7.684$; $p < 0.001$]. *Post hoc* analysis showed the following sensors location significance, index $p = 0.003$; thumb $p = 0.001$; wrist $p = 0.005$ (Figure 4.10).

ANOVA analysis showed a significant main effect of OFF/HS [$F(1; 23) = 34.776; p < 0.001$] and of sensor location [$F(4; 92) = 84.44; p < 0.001$] on this index, with a significant interaction between OFF/HS state and sensor location on this index [$F(4) = 23.31; p < 0.001$]. *Post hoc* analysis shows the following sensors location significance, index, wrist, and metacarpus $p < 0.0001$; thumb $p = 0.0003$, and arm $p = 0.0002$ (Figure 4.10).

ANOVA analysis showed a significant main effect of OFF/HS [$F(1; 23) = 23.892; p < 0.001$] and of sensor location [$F(4; 92) = 93.198; p < 0.001$] on this index, with a significant interaction between OFF/HS state and sensor location on this index [$F(4) = 13.583; p < 0.001$]. *Post hoc* analysis shows the following sensors location significance, index, wrist, and metacarpus $p < 0.0001$; thumb $p = 0.001$, and arm $p = 0.0004$ (Figure 4.10).

The total power well correlates with the UPDRS item 25 score assigned. The sensor located on the index finger and thumb shows correlation in both OFF and ON motor condition (index OFF $R^2 = 0.35$; ON $R^2 = 0.34$; thumb OFF $R^2 = 0.35$; ON $R^2 = 0.35$), while for the wrist and metacarpus there is a correlation only in OFF motor status (wrist OFF $R^2 = 0.36$; metacarpus OFF $R^2 = 0.38$).

Since smooth and well-coordinated movements are typical features of a healthy and well-developed human motor behavior, we expect that the intake of the medication should be assessed by smoothness values near to zero.

For the finger-tapping task (Table 4.4), ANOVA analysis showed a significant main effect of ON/OFF state [$F(1) = 16.984; p = 0.002$] and of sensor location [$F(4) = 157.654; p < 0.001$] on smoothness index, without an interaction between ON/OFF state and sensor location on this index [$F(4) = 2.33; p = 0.071$]. *Post hoc* analysis showed the following sensors location significance, index finger $p = 0.003$; thumb $p = 0.004$; metacarpus $p = 0.005$; arm $p = 0.0001$ (Figure 4.11).

ANOVA analysis shows a significant main effect of OFF/HS [$F(1; 23) = 11.427; p = 0.003$] and of sensor location [$F(4; 92) = 138.011; p < 0.001$] on smoothness index, without an interaction between OFF/HS state and sensor location on this index [$F(4) = 1.58; p = 0.186$]. *Post hoc* analysis shows the following sensors location significance, index $p = 0.003$; metacarpus $p = 0.006$; wrist $p = 0.008$; arm $p = 0.002$ (Figure 4.11).

There is no significant effect of ON/HS status on smoothness index.

For arm pronation-supination task (Table 4.5, ANOVA analysis shows a significant main effect of ON/OFF state [$F(1) = 5.025; p = 0.047$] and of sensor location [$F(4) = 8.409; p < 0.001$] on smoothness index, without an interaction between ON/OFF state and sensor location on this index [$F(4) = 0.607; p = 0.659$]. *Post hoc* analysis shows no statistically significant differences among sensors (Figure 4.11).

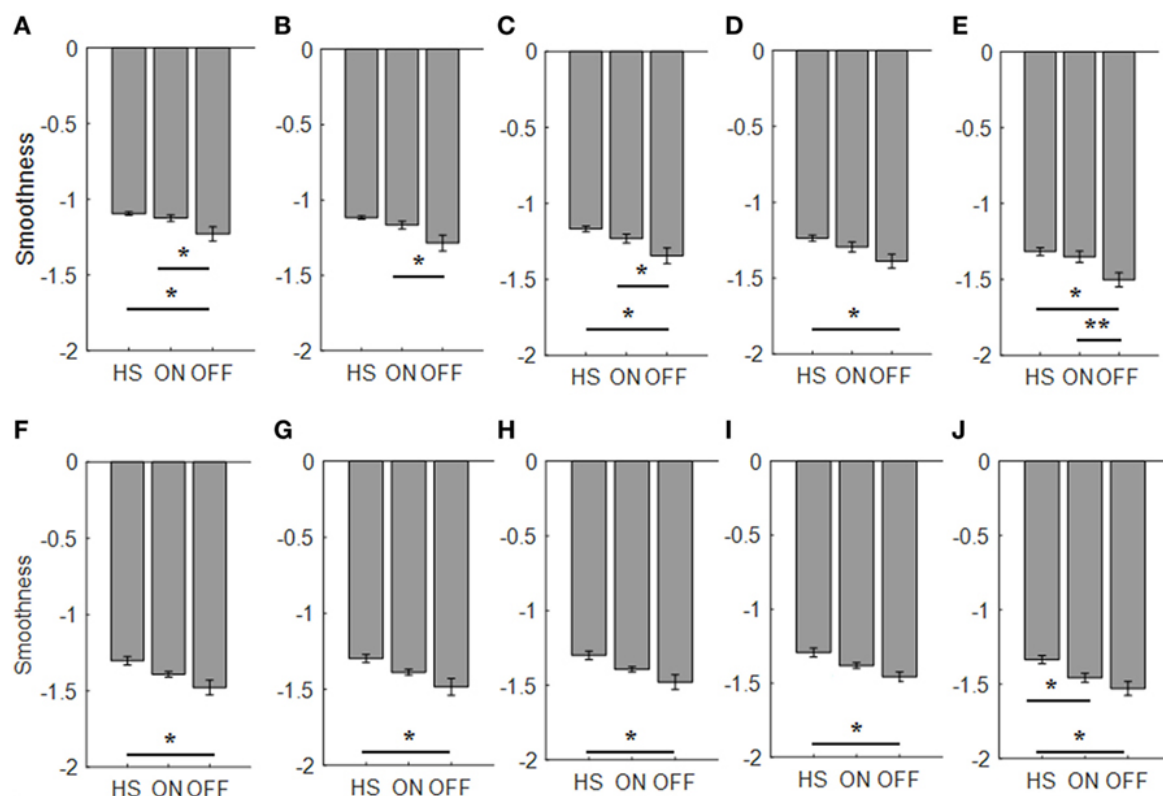


Fig. 4.11 Smoothness index. Each panel shows the averaged values for each group OFF, ON, and HS for index finger [(A): finger tapping; (F): arm pronation-supination], thumb [(B): finger tapping; (G): arm pronation-supination], metacarpus [(C): finger tapping; (H): arm pronation-supination], wrist [(D): finger tapping; (I): arm pronation-supination], arm [(E): finger tapping; (J): arm pronation-supination]. Bars denote the SE. Bonferroni correction $*p < 0.01$; $**p < 0.001$.

ANOVA analysis shows a significant main effect of OFF/HS state [$F(1; 23) = 12.089$; $p = 0.0002$] and of sensor location [$F(4; 92) = 7.315$; $p < 0.0001$] on smoothness index, without an interaction between ON/HS state and sensor location on this index [$F(4) = 0.514$; $p = 0.726$]. *Post hoc* analysis shows the following sensors' location significance, index, and metacarpus $p = 0.005$; wrist $p = 0.001$; thumb $p = 0.008$; arm $p = 0.002$ (Figure 4.11).

ANOVA analysis shows a significant main effect of ON/HS state [$F(1; 23) = 8.271$; $p = 0.009$] and of sensor location [$F(4; 92) = 15.072$; $p < 0.001$] on smoothness index, without an interaction between ON/HS state and sensor location on this index [$F(4) = 1.354$; $p = 0.256$]. *Post hoc* analysis shows the following sensors' location significance: arm $p = 0.005$ (Figure 4.11).

No correlation has been found with the arm pronation-supination task, between UPDRS item 25 score and the smoothness index, but there is a good correlation between UPDRS

item 23 score in ON motor condition and the smoothness index for sensors placed on wrist ($R^2 = 0.36$), thumb ($R^2 = 0.47$), metacarpus ($R^2 = 0.49$), and arm ($R^2 = 0.43$) during the finger-tapping task.

Taking into account the relationship between elbow rigidity and the smoothness index, results show no discrimination ability between PD OFF condition and ON status, or PD and HS, as shown in Figure 4.12. In addition to this, no correlation between UPDRS item 22 score and smoothness index has been found for rigidity.

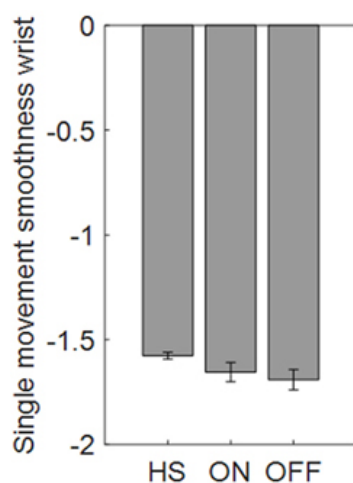


Fig. 4.12 Smoothness index computed for the wrist in the rigidity task. Values are averaged for each group. Bars denote the SE.

Discussion and conclusions

In the last years, a huge number of studies have been published about the quantitative analysis of movement in PD [4] [105] [107] [108] [106]. The variety of indicators extracted by accelerometer, gyroscope, magnetometer and other sensor's signals in the literature is high. Nevertheless, several questions are still open, since we have not yet reached the stage of a consensus about : which kind of sensor is more suitable for evaluating PD patients, and if it is better to have a single index for each Parkinsonian symptom, or a global index of impairment; where is the best place on the body to wear these sensors, the level of invasiveness acceptable by the patient for at-home long-term recording. A recent review [4], focused on published research papers on wearable technologies for PD in the last 10 years, showed that among the 848 analyzed studies only the 6% presents a reliable quantitative assessment system ready for clinical use in the next future. However, a huge number of studies present proof of concepts that could become useful for clinical use in the next years.

The state of the art of quantitative assessment tools for PD clearly shows that interactive motor tasks recorded using wearable magneto-inertial measurement units, allowed to deeply analyze the kinematic and dynamic characteristics of goal-directed movements of upper limb, and to extract quantitative and useful indices for the motor symptoms evaluation.

With the present study, we have searched answer to open questions, which slow the progression to clinical application of the available technologies.

The first question we addressed is: where is the best place where to locate sensors. By using a redundant number of upper arm sensors (index finger, thumb, metacarpus, wrist, and arm), our results showed that a distal location of sensors on upper arm (*i.e.* on index finger) is more sensible to catch the kinematic features of Parkinsonian movements. The following questions are: which index can better differentiate PD patients OFF from ON motor condition and patients in these two conditions from HS. Our results introduced new indexes that well describe the clinical motor symptoms, and are able to differentiate PD ON/OFF condition and PD vs HS.

For the first time, we provide a complete kinematic description of the classic definition of bradykinesia [93] through different quantitative kinematic indexes: the "slowness of voluntary movement" has been well described by the total time needed to complete the task (the finger-tapping or the arm prono-supination task); while the "progressive reduction in speed and amplitude of repetitive actions", has been properly described by a new kinematic index, defined fatigability index. These two kinematic indexes are able to discriminate the ON from the OFF motor condition in PD patients. Moreover, in order to describe bradykinesia, the prono-supination task seems to be the most informative, since we can discriminate PD ON vs OFF motor condition with this simple task (with any sensor location among thumb or wrist) and, in addition, we can discriminate PD patients in any of these two conditions from HS group. The intrinsic features of prono-supination task, which involves an highest number of muscles, leads to a more versatile task, able to describe the variability of Parkinsonian movement, with sensors placed in different location on upper arm. Conversely, the features of finger-tapping task, lock its utility to the sensor location on the index finger, in this case the results showed a good discrimination ability to distinguish the PD ON vs OFF motor condition.

Overcoming the classic bradykinesia definition, we describe the kinematic of Parkinsonian movement with further two indexes. In order to describe the overall "intensity" of movement, we have extract the total power, *i.e.* the power spectrum of the frequency of movement during finger-tapping and prono-supination task. Also for this kinematic index, the prono-supination task showed to be more informative compared with other condition, since the total power index can discriminate PD ON vs OFF motor condition and PD patients in

ant of these conditions from HS with any sensor location among index finger, thumb, or wrist. Even the most proximal sensor (arm) is useful to discriminate HS from PD in OFF condition during the prono-supination task. For finger-tapping task, with a sensor placed on the index finger, the total power can discriminate PD ON vs OFF motor condition, and the later from HS. Therefore, the results show that using prono-supination task, analyzing power index, is able to perform a complete PD ON/OFF and PD/HS discrimination with sensors placed on index finger, thumb, or wrist. The good performance of this index could be explained from its neurophysiological interpretation. In PD, repetitive movement are supposed to be arhythmic, other than slow, and characterized by a progressive reduction in speed and amplitude. Therefore, the total power index is a perfect index to catch the arhythmicity and the variability of a movement, since an arhythmic movement will be characterized from a more broad and flat PSD graph compared with a rhythmic movement.

The last index we proposed for the kinematic analysis, *i.e.* the smoothness index, could be interpreted as a bridge parameter, able to describe features that belong to both bradykinesia and rigidity. This kinematic index describes the fluidity of movements, so that it can catch the features of both the bradykinesia, related to the variation of movements rhythm, caused by interruptions or hesitations during task, as well as the cogwheel rigidity, which fragment and decompose passive movement around the joint. For bradykinesia, the smoothness index during prono-supination task is able to discriminate PD in OFF motor condition from HS, with any sensor location among index finger, thumb, metacarpus, wrist and arm; but also PD in motor condition from HS with sensor placed on arm. During finger-tapping task, the smoothness index is able to discriminate DP in OFF from ON motor condition, with any sensor location except the wrist, and PD in OFF from HS group, with any sensor location except the thumb.

Total power is the only index which showed a good correlation with the related UPDRS score, for both finger-tapping and arm prono-supination task, in OFF/ON comparison. These versatile features suggest to explore this index in future studies, as a candidate to monitor PD motor symptoms. Total time, total power and smoothness show a good correlation with the UPDRS score for finger-tapping task, therefore the use of these indexes is suggested only for this task.

The first aim of the present study is to identify the most sensible place where to locate sensors to monitor PD motor symptoms. Our results suggest that a distal location of wearable sensors, on index finger or wrist, should be preferred in these kinds of studies, in order to better describe the kinematic features of Parkinsonian movements.

In order to differentiate PD OFF from ON motor condition, the best solution seems to be placing a M-IMU on index finger during finger-tapping task, obtaining data useful to extract

4.2 Assessment of Parkinson's disease by means of a wearable M-IMU network 105

the kinematic indexes proposed (total time, total power, or smoothness). In addition to this, this sensor location guarantees a good correlation between the clinical score as expressed by UPDRS scale and the kinematic measure, *i.e.* total power and total time.

In order to differentiate PD patients from HS, the total power index, computed from data acquired by a sensor placed in any location among index finger, thumb, metacarpus, wrist and arm, during prono-supination task, show the best accuracy. However, during the same task, also total time in any sensor location could be a valid alternative to differentiate PD patients from HS.

In conclusion, combining all results, our study shows that, taking into account all variables (*i.e.* sensor location, motor task performed, kinematic indexes), the most versatile and complete solution, which can solve both differentiations (OFF vs ON; PD vs HS), with the highest accuracy, is to place one M-IMU on index finger, thumb, or wrist, performing a prono-supination task, and use the total power as kinematic index. However, keeping in mind the small sample size of the present study, the proposed indexes are good candidates to be explored in further confirmation studies with larger population.

4.2.2 Feature extraction in Sit-to-Stand task using M-IMUs for the assessment of Parkinson's disease

Similarly to previous study we tried to assess Parkinson's disease monitoring of kinematic parameters by mean of M-IMUs. In this case we analyzed the sit-to-stand task (*SiSt*) of the UPDRS part II (task 27) on two groups, one of Parkinson's disease patients (PD) and another one of healthy control subjects (HS).

This task has an high relevance on a clinical point of view, as already studied in [113], since it consists in a posture transition which permits to dynamically pass from a static position to another one. It is also an important section of the most commonly used *timed up and go* test [114]. moreover, previous studies have shown that posture transitions, such as *SiSt*, evidence the risk of falling in elderly [115] as well as in stroke patients [116].

There are several types of wearable systems for estimating physiological parameters by body movements, based on M-IMUs, piezoresistive sensing elements and fiber optic sensors [117] [118] [119] [120]. In this study we used a system based on a 9-axes M-IMU, *i.e.* a combination of a 3-axes accelerometer, a 3-axes gyroscope, and a 3-axes magnetometer. This type of sensors have already been used in other recent studies which involve PD [5] [92] [121].

The main goal of this study is to propose a broad method for the detection of the most relevant features for the *SiSt* task analysis. The features extraction has been provided by

a meticulous analysis of the literature on this topic, with an implementation of further characteristics. Then, we underlined the best features which evidence different scores in the UPDRS, between PD patients in ON/OFF phase or HS subjects.

Measurement system

The measurement system we use is based on a M-IMU sensor, attached with a belt to the trunk, in front of the sternum, as shown in Figure 4.13.

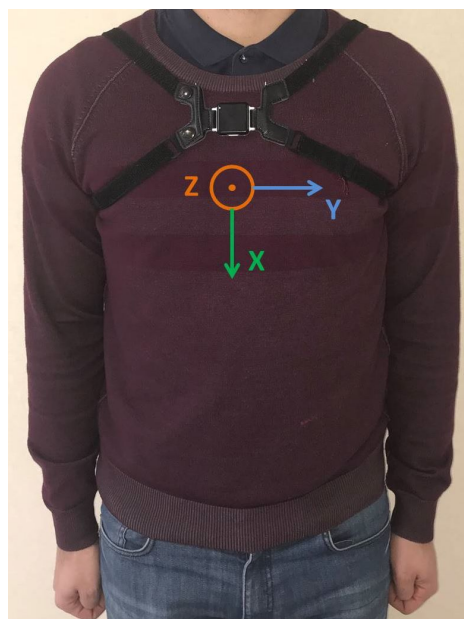


Fig. 4.13 Trunk sensor orientation has the x-axis roughly put in vertical and pointing to the ground, the z-axis is in the sagittal plane with the direction parallel to the horizontal axis and points frontally, and the y-axis is also horizontal and points to the left of the subject, completing the orthonormal basis.

The M-IMU sensor used is a commercial device called Opal, by APDM Inc. (Portland, OR, USA). This sensor provides the value of acceleration (± 16 g), angular velocity (± 2000 deg/s), the intensity of the magnetic field (± 8 Gauss) and the quaternions, computed via the manufacturer's Kalman filter. Its sampling frequency is 128 Hz and the A/D has a 16-bit resolution. These specific sensors have already been validated in detail by Ricci et al. in [3].

All the acquisitions have been recorder with a camera, the GoPro Hero4 Silver (GoPro, San Mateo, CA, USA). The GoPro camera uses a 800x480 video format with a frame rate of 120 fps.

The data have been acquired with MotionStudio software by APDM Inc. (Portland, OR) which sends a trigger to the camera in order to synchronize it with the Opal sensors.

Subjects and protocol

This study involve two groups of participants: the first included sixteen PD patients (6 females, ages 66.6 ± 6.5 years) and an age-matched group of thirteen HS (7 females, ages 64.0 ± 11.7 years).

The inclusion criteria are possible-probable diagnosis of PD following UK PD Society Brain Bank criteria [122] in addition to an Hoehn and Yahr stage between 1 and 2.5 [97]. On the other side the exclusion criteria are the Hoehn and Yahr stage bigger than 2.5 and a physiological joints movement reduction caused by the presence of other pathologies.

The protocol consists in an execution of the *SiSt* task, following the guidelines expressed in the UPDRS, while the physician assigns the appropriate score to the patient. PD patients execute the task in ON and OFF phase, while the HS subjects do it one time only.

In the *SiSt* task the physician asks the subject to cross his/her arms across the chest and then to stand up. If the patient is not able to do it, he/she must repeat this attempt a maximum up to two more times. If still unsuccessful, the patient can push himself/herself off using his/her hands on the arms of the chair.

Data analysis

The data analysis includes four steps: 1) detection of *SiSt* transition, 2) identification of subjects to exclude, 3) features extraction and 4) statistical analysis.

1) *detection of SiSt transition*: firstly, there is an evaluation of the trunk tilt, corresponding to the angle θ , obtained as the rotation around the y-axis, considering positive the angle obtained from a trunk flexion. After this, $\sin(\theta)$ is computed and filtered in order to cancel the drift and the high-frequency noise, using a discrete wavelet transform (DWT) based on Mallat's algorithm [123]. The DWT decomposes the signal in an iterated way, splitting it into many lower-resolution components. At each decomposition scale, the number of samples in the time domain is decreased by eliminating every second sample, in other words there is a down-sampling by a factor of 2. As the wavelet transform can distinguish noise and signal edge more precisely than other transforms (*e.g* Fourier), filters designed with this technique perform noise cancellation without distortion of the original signal [124].

Similar to [116], the signal was filtered in the frequency band 0.031 - 0.5 Hz, corresponding to the signal obtained subtracting the $\sin(\theta)$ at scale 7 with the one at scale 11. In Figure 4.14 are shown the original signal and the filtered one; it can be noted that the filtered one presents two relative minimums, *P1*, *P2* (Figure 4.14). These two peaks are chosen as the beginning and the end of the task, as already done in similar works [113].

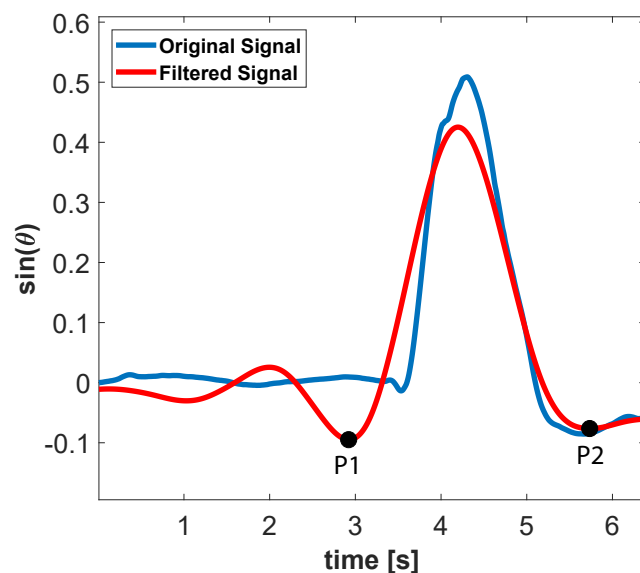


Fig. 4.14 Original signal of $\sin(\theta)$ computed from the quaternion data and the filtered signal obtained using a DWT. The original signal is decomposed between scales 7-11 with the wavelet Coiflet of order five [125]. The minimum peaks immediately before and after the maximum one are $P1$ and $P2$. These two points identify the $SiSt$ postural transition.

2) *identification of subjects to exclude*: at first approximation we hypothesized that large part of the $SiSt$ movement is with the main axis of rotation aligned with the y -axis of sensor (roughly horizontal, as shown in Figure 4.13). To check how good this hypothesis is, we use the method proposed by Ricci et al. [126], in order to estimate the main axis of rotation of a given movement.

Thus, in the ideal case, the estimated axis of rotation in sensor reference frame

$$a = [a_x, a_y, a_z] \quad (4.4)$$

should be aligned with the y -axis, *i.e.*:

$$[a_x, a_y, a_z] = [0, 1, 0] \quad (4.5)$$

In this study we assumed that a reliable value, for our approximation, is:

$$a_y \geq 0.95 \quad (4.6)$$

Subjects who do not verify this parameter have been excluded from the study.

4.2 Assessment of Parkinson's disease by means of a wearable M-IMU network 109

3) *features extraction*: examining the literature, the following *SiSt*-related parameters have been identified.

- *Transition Duration (TD [s])*: it is the duration of the postural transition [116], [127]. Defined as the interval between *P1* and *P2*, *i.e.* $TD = t(P2) - t(P1)$.
- *Time of Postural Transition (tPT [s])*: it is time in which the subjects passes from the flexion to the extension of the thorax [128].
- *Max Trunk Flexion (MAX(θ) [rad])*: it is the amplitude of the positive peak of θ (Figure 4.15), it coincides to the angle value in tPT ($\theta(tPT)$) [113].

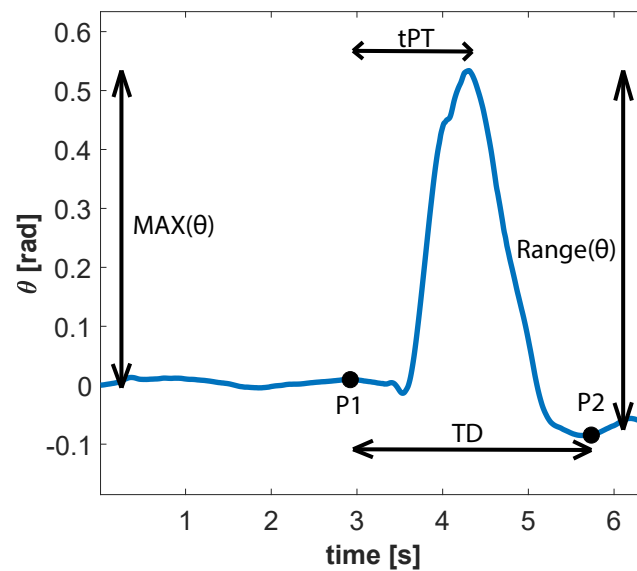


Fig. 4.15 Feature referred to the values of θ . This signal is filtered with a DWT in the frequency band 0.031 - 0.5 Hz.

- *Range theta* ($Range(\theta)$ [rad]): it is the maximum range of flexion-extension tilt of the trunk [113].
- *Peak Angular Velocity* ($MAX(vel)$ [rad/s]): it is the peak of the angular velocity, ω_y (Figure 4.16), of trunk in the sagittal plane [129].

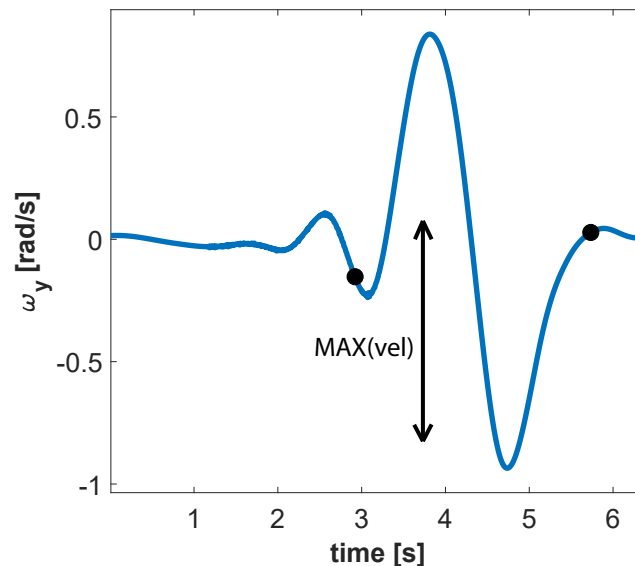


Fig. 4.16 Feature referred to the values of ω_y . The value of gyroscopes is filtered using a DWT filter between scales 6 and 11, i.e. a bandpass between frequencies 0.031 - 1 Hz.

- *Average Angular Velocity (Mean(vel) [rad/s]):* it is the mean of the angular velocity of trunk in the sagittal plane [129].
- *Minimum of Acceleration (min(acc) [m/s²]):* it is the minimum value of the vertical acceleration (a_v) [113], shown in Figure 4.17, computed as described in [130] and [131]. In particular, the acceleration signals, after subtracting the gravity contribution, have been firstly filtered with a DWT, using a low pass filter with a cut-off frequency of 1 Hz (scale 6). The derived acceleration is a composition of the vertical projection of x and z axes of the accelerometers, respectively acc_x and acc_z , then the vertical acceleration a_v is computed as follows:

$$a_v = -acc_x \cdot \cos(\theta) - acc_z \cdot \sin(\theta) \quad (4.7)$$

- *Maximum of Acceleration (MAX(acc) [m/s²]):* it is the maximum value of the vertical acceleration [113].
- *Range of Acceleration (Range(acc) [m/s²]):* it is the amount of the acceleration included between the maximum and the minimum values [113].

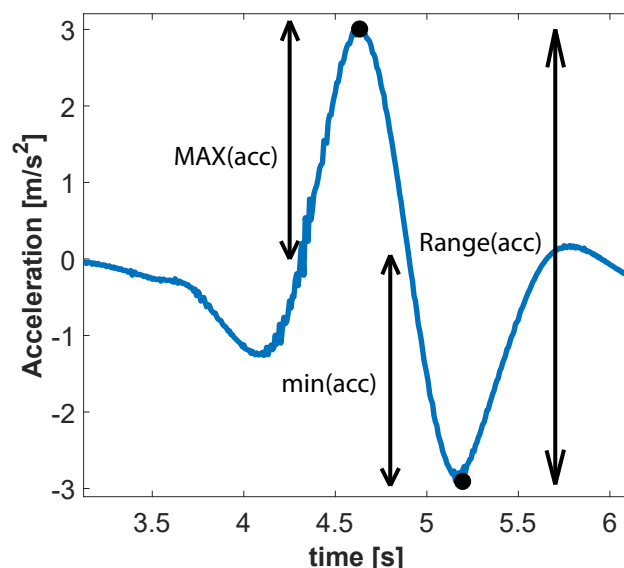


Fig. 4.17 Feature referred to the values of a_v . The value of accelerometers is filtered using a DWT filter using the scale value of 6, i.e. a lowpass with a cut-off frequency of 1 Hz.

- *Number of Attempts (nATT)*: this is the number of attempts a subject needs to stand up. This value has already been examined by [113] and it is very reliable since this parameter is analysed also by the physician in order to assign the UPDRS score. This feature has been extracted evaluating the number of positive peaks of the $\sin(\theta)$ signal, before the definitive standing up.
- *Rho (ρ)*: this feature is defined in [126] as an index referred to the reliability of the computed reference axis. It is bounded in $[\frac{1}{3}, 1]$ and an high value is referred to a good reliability of the axis. This means that an high value is referred to a pure rotation around the y-axis of the trunk M-IMU, while a low value means that the subjects has been uncoordinated and not clean in the *SiSt* transition.
- *Spectral Arch Length (SPARC)*: this feature, defined in [110] and [111], can account for the change in the number of submovements and the inter-submovement interval, which are movement characteristics influenced by bradykinesia. To compute smoothness it is not necessary to filter data, because of the inherit low-pass filtering action performed by the *SPARC* algorithm. In particular we decided to compute *SPARC* of speed profile in the frequency band 0-4 Hz, as already done in [92] and [5].

4) *Statistical analysis*: finally, we perform a simple statistical analysis in order to investigate which parameters better represent changing between the OFF-ON conditions and the pathological status versus healthy subjects (OFF-HS and ON-HS). In the first case we use a paired-sample t-test, while in the second case we use an independent sample t-test.

Results

In this section we report results of each indicator, related to OFF, ON and healthy status of subjects.

Figure 4.18 reports the results of PD subjects in ON and OFF phase in comparison with HS group. In this Figure blue bars represents results in OFF phase, green bars in ON phase and orange bars are relative to HS; mean values and standard errors of all features are represented.

It can be observed how *SPARC* and ρ parameters, that have never been used in *SiSt* task before, does not represents a statistically significant variability in the three different phases.

Other features have a wider fluctuation in the variability of the results obtained, but only those relative to trunk acceleration reports a statistically significant result. As a matter of facts, the maximum trunk acceleration of trunk flexion report a p -value lower than 0.05; in particular it is 0.016 between OFF and HS, and 0.044 between ON and HS. In addition to this, also the range of acceleration has a statistically significant p -value between OFF and HS subjects, equal to 0.014.

Discussion and conclusions

In this work we deeply studied the literature about *SiSt* task's features extraction, in order to evidence which parameters are more relevant to better analyze this task in PD pathology. In addition to this, we also propose a new method for a preliminary analysis, able to identify reliable movements during *SiSt* task.

The high number of features extracted permits to properly and widely analyze the *SiSt* task, dealing with the problem that the subject can act with a large variety of strategies to perform this activity [132], [133]. This deeper analysis can overcome the poor reliability of the *SiSt* task in comparison to the other parts of the *timed up and go* test, as studied in [129].

It is also possible to determine differences in the *SiSt* task execution that the physician it is not capable to notice; in fact, sensors can provide a higher resolution with respect to the clinical evaluation, since the UPDRS scale assigns a score between 0 and 4 points only. This can be noticed in the results obtained from the statistical analysis: they evidence the

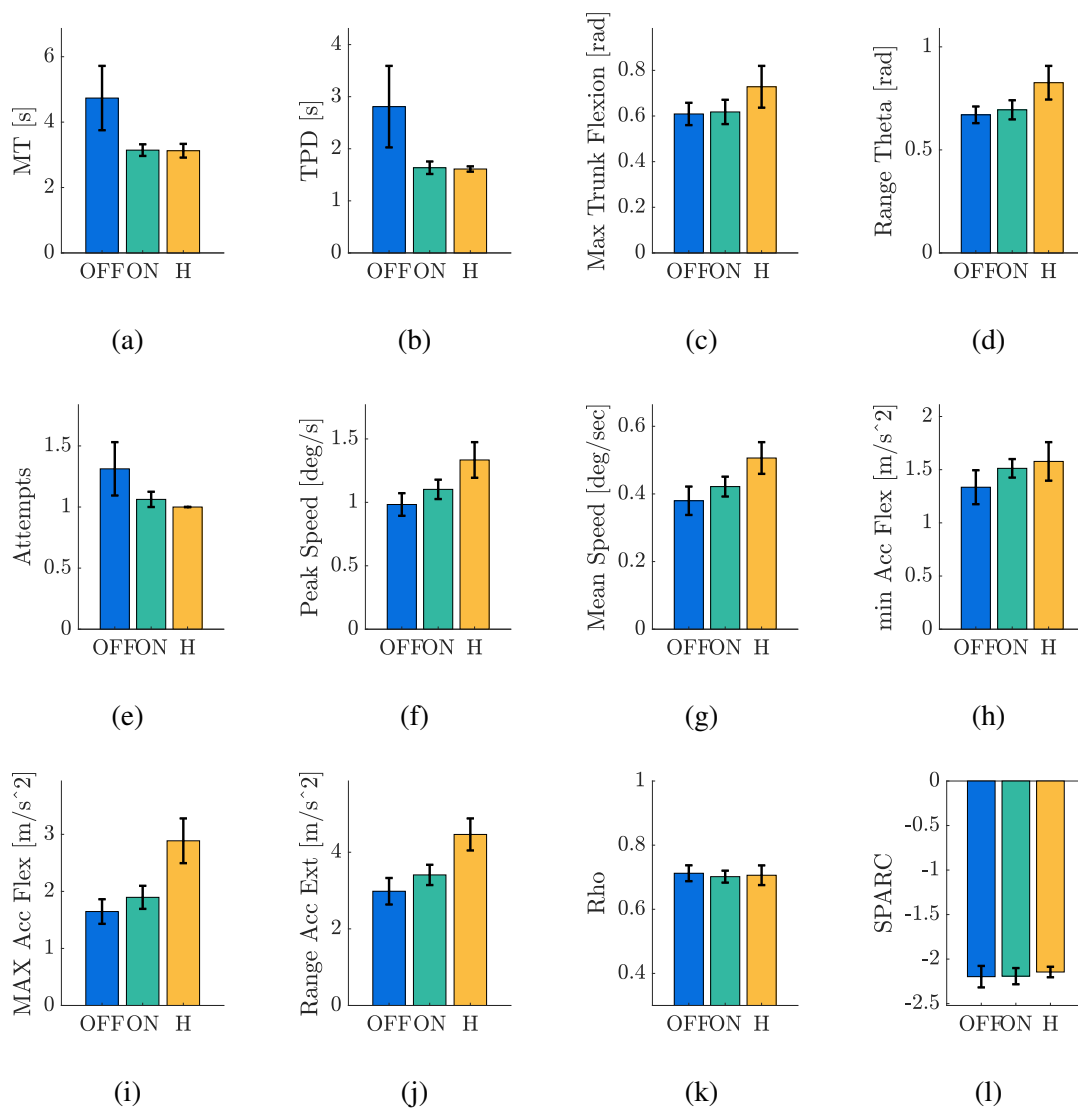


Fig. 4.18 Results about *SiSt* task's features, described in detail in Section 4.2.2: *MT*, *TPD*, *Max Trunk Flexion*, *Range Theta*, *Number of Attempts*, *Peak Speed*, *Mean Speed*, *min Trunk Acceleration*, *Max Trunk Acceleration*, *Range Trunk Acceleration*, *Rho*, *SPARC*. Results are represented in mean and standard error. In each graph, first column (blue) represents the OFF phase, second column (green) represents ON status, third column (orange) represents H subjects.

4.2 Assessment of Parkinson's disease by means of a wearable M-IMU network 115

possibility to detect differences between ON, OFF and HS subjects; moreover, they show lighter variations that cannot be easily identified by the UPDRS clinical scale.

As a matter of fact, with this analysis we found differences between PD and healthy subjects. Of particular interest is the comparison between the HS subjects and the OFF/ON PD subjects with a 0 UDPRS score. In this case could also be noticed that there are some lightly differences in the feature evaluation which can evidence that a PD subject, even at the best of his/her motor functions, are still unable to reach the level of healthy subjects.

This study underlines the possibility to easily analyze the *SiSt* task with only one M-IMU, located on the trunk. Developing a simple, non invasive and cheap analysis of this task has a notable relevance; as a matter of fact, *SiSt* is performed by everyone a considerably number of times during the day. In this way it is possible to develop a system to continuously monitor the patient's status, in order to identify the ON and OFF phase during the day.

It could also be interesting to have sensors on arms to identify the use of hands during the execution of the task. In fact, in the UPDRS scale the clinician must control if patient push himself/herself off the chair using his/her hands on the arms of the chair.

A useful future development of this work may consist in the use of principal component analysis (*PCA*) or independent component analysis (*ICA*), in order to identify a smaller, but more significant, set of features composed of those described in this article. In this way it should be possible to simplify the analysis of this task and obtain more significant results which can give an higher reliability of the *SiSt* task.

Using other algorithms, able to identify physical activities [113], [130] and [131], it is possible to detect the *SiSt* transition to monitor the features extracted and to control the patient during this task. In this way the physician can control, also with telemedicine devices, the PD's state in which the patient is, in addition to underling problems of stability [116] and risk to fall. Finally, this method could offer a promising tool for long term and home care monitoring for PD patients.

Tesi di dottorato in Bioingegneria e bioscienze, di Jacopo Tosi,
discussa presso l'Università Campus Bio-Medico di Roma in data 28/05/2019.
La disseminazione e la riproduzione di questo documento sono consentite per scopi di didattica e ricerca,
a condizione che ne venga citata la fonte.

Chapter 5

Discussion and conclusions

The progress of magneto-inertial measurement units has brought to an ubiquitous presence of this technology in an increasing number of devices. Aside from sensor development, advancements in the algorithms that are often implemented by microcontrollers embedded in the sensing units, together with low power and low cost technologies, are transforming them into attractive solutions for motor assessment. As a result, magneto-inertial sensors have a widespread use in a plethora of different and novel areas of application, including biomedical field.

In consideration of that, this dissertation has a twofold purpose. On the one side, our aim is to design and evaluate a M-IMU sensor network particularly devised for the motor assessment of neurological disorders, taking into account the technical requirements coming from this specific application field: a low cost system which exploits a low power standard technology for long term at-home monitoring of patients, in order to use small batteries reducing dimensions and weight; relevant throughput for applications based on motion tracking; assess and optimize sensor fusion algorithms for movement analysis. On the other side, we aim at testing on the field the potentialities of M-IMU sensor network for the quantitative assessment of motor performance in neurological disorders, focusing in particular on patients affected by Parkinson's disease. We aim to confirm and improve previous studies on the use of M-IMU-based motor features. able to describe the clinical status of the patients. In this way, it would be possible to have a continuous and objective monitoring of the subject, which permits to have a better evaluation of the disease jointly with using fewer resources.

The presented work has accomplished the research goals stated in Section 1.2: a comprehensive evaluation of Bluetooth Low Energy and the analysis of its performance in high throughput multinode applications; the design of a standard protocol to evaluate and tune sensor fusion algorithms in order to improve the orientation data obtained and reduce the

reconstruction error to the minimum; the use of a reliable M-IMU network, based on BLE wireless technology, for the assessment of neurological disorders, such as Parkinson's disease.

As already stated, after an exhaustive and reliable review of Bluetooth Low Energy, our main objective is to design a low-power-based sensor network with an adequate throughput to perform motion analyses. Hence, we developed a BLE multinode network and evaluated its performance obtaining a star network of 5 nodes with a global bitrate higher than 170 kbps, *i.e.* streaming packets of 20 bytes (9-axes M-IMU with a resolution of 16 bits per channel) at rates higher than 200 Hz; at this rate the consumption of a single node is around 12 mA, hence, with a very small battery (*e.g.* 100 mAh of capacity and dimensions 5mm × 12mm × 20mm) an uninterrupted streaming for 6.2 h is guaranteed. In addition to that, to perform this experiment we also designed a novel protocol useful to assess throughput in a generic network.

Then, we needed to evaluate magneto-inertial measurement units, in particular sensor fusion algorithms used to get orientation from inertial and magnetic data. In fact, it is usually difficult to find reliable and objective data related to the output of sensor fusion filters, and would also be useful to tune the filters depending on the specific application. To this purpose, we designed a standard protocol in the special orthogonal group $SO(3)$, which exploits a motion capture system as ground truth, in order to evaluate filter's performance after tuning gain parameters; in particular, we tested a Kalman filter and several typologies of complementary filters (*i.e.* Mahony [51], Madgwick [66], Campolo [74], and Tian [49]). Results about orientation showed that it is possible to reach error angles lower than 5° on average, in dynamic conditions, and around 2° in static cases; the best performance are guaranteed by the Kalman and the Campolo filters.

Finally, we applied M-IMU sensor networks in the assessment of neurological disorders, in particular Parkinson's disease. We found the possibility to detect the two phases of Parkinson's disease (*i.e.* ON and OFF status) and also differentiate them from healthy patients. After a deep analysis of some of the UPDRS tasks administered by the physician to the patients, we evidenced statistically significant results to assess PD. The first analysis regards patients during the execution of arm prono-supination task and evaluating the total power as kinematic feature on only one sensor positioned on the index, thumb or wrist. These sensor locations and kinematic index can detect statistically significant differences between ON and OFF state (index: $p = 0.003$; thumb: $p = 0.001$; wrist: $p = 0.005$), and also between PD and healthy subjects (index, thumb, wrist: $p < 0.0001$). Moreover, we also found that using one M-IMU only on the trunk while performing a sit to stand task and evaluating trunk acceleration during trunk flexion is it possible to differentiate OFF and ON with respect to healthy subject ($p < 0.05$).

5.1 Future works

This dissertation spanned over various aspects related to the use of wearable magneto-inertial sensor network for biomedical applications, paving the way for new reliable applications of those sensors.

For what it may concern the evaluation of BLE network, a future investigation may regard the use of the protocol we designed to assess other typologies of BLE integrated circuits from different producers, in order to point out what are the advantages and disadvantages of each one of them. In addition to this, a further investigation may regard the application of new low energy standard protocols, such as Bluetooth 5.

With reference to the evaluation of M-IMU sensor fusion algorithms, we need to improve the methodology proposed. It is of fundamental importance to assess the standard procedure we designed with different patterns of trajectories, in order to validate filters depending on the specific applications they are used in. Moreover, it would be useful to create a database with standard movements which may be used in future to assess new sensor fusion algorithms.

For what it may concern a future development relative to the assessment of PD by mean of M-IMUs we propose to improve and strengthen the feature extraction developed with the use of PCA, ICA or machine learning algorithms. In addition to this, it would be fundamental to assess these systems for long term at-home application in order to evaluate their reliability and be part of the therapy monitoring of all the patients.

Of note, from a technological point of view, we proposed and tested two standard methodologies that can be used to respectively evaluate wireless communication technology's performance and the error of M-IMU sensor fusion algorithms. In particular, the evaluation we performed on M-IMU sensor fusion algorithms is limited to the filters we used, and it is strictly related to the actual state of the art. Exactly for this reason, we propose to create a database of M-IMU data shared in the scientific community, based on standard movements, which can be used to assess new filters' performance in relation to the specific application in which we want to exploit them.

The main objective of future works is to create a user-friendly, low cost and low power system, able to assess Parkinson's disease. In particular main efforts should be devoted to find the best features for evaluation of this disease in order to have a continuous, reliable and objective monitoring of the subject and the progression of her/his pathology. That would improve the assessment, monitoring and treatment of the disease with the employment of fewer resources.

Tesi di dottorato in Bioingegneria e bioscienze, di Jacopo Tosi,
discussa presso l'Università Campus Bio-Medico di Roma in data 28/05/2019.
La disseminazione e la riproduzione di questo documento sono consentite per scopi di didattica e ricerca,
a condizione che ne venga citata la fonte.

Appendix A

Representation of orientation

There are different possible parametrizations to describe orientation. This appendix provides the description and the conversion formulas of some of the orientation representations used throughout this dissertations. A more detailed description can be found in [134] and [135].

A rotation is a displacement in which at least one point of the rigid body remains in its initial position and not all lines in the body remain parallel to their initial orientations. For example, a body in a circular orbit rotates about an axis through the center of its circular path, and every point on the axis of rotation is a point in the body that remains in its initial position.

A.1 Rotation Matrix

The orientation of coordinate frame i relative to coordinate frame j can be denoted by expressing the basis vectors $(\hat{x}_i \hat{y}_i \hat{z}_i)$ in terms of the basis vectors $(\hat{x}_j \hat{y}_j \hat{z}_j)$. This yields $({}^j\hat{x}_i {}^j\hat{y}_i {}^j\hat{z}_i)$, which when written together as a 3×3 matrix is known as the rotation matrix. The components of jR_i are the dot products of basis vectors of the two coordinate frames.

$${}^jR_i = \begin{pmatrix} r_{11} & r_{12} & r_{13} \\ r_{21} & r_{22} & r_{23} \\ r_{31} & r_{32} & r_{33} \end{pmatrix} = \begin{pmatrix} \hat{x}_i \cdot \hat{x}_j & \hat{y}_i \cdot \hat{x}_j & \hat{z}_i \cdot \hat{x}_j \\ \hat{x}_i \cdot \hat{y}_j & \hat{y}_i \cdot \hat{y}_j & \hat{z}_i \cdot \hat{y}_j \\ \hat{x}_i \cdot \hat{z}_j & \hat{y}_i \cdot \hat{z}_j & \hat{z}_i \cdot \hat{z}_j \end{pmatrix} \quad (\text{A.1})$$

Because the basis vectors are unit vectors and the dot product of any two unit vectors is the cosine of the angle between them, the components are commonly referred to as direction cosines.

A.1.1 Conversion formulas

Equivalent rotation matrices for various representations of orientation, with abbreviations $c_\theta := \cos \theta$, $s_\theta := \sin \theta$, and $v_\theta := 1 - \cos \theta$

$Z - Y - X$ Euler angles (α, β, γ) :

$${}^jR_i = \begin{pmatrix} c_\alpha c_\beta & c_\alpha s_\beta s_\gamma - s_\alpha c_\gamma & c_\alpha s_\beta c_\gamma - s_\alpha s_\gamma \\ s_\alpha c_\beta & s_\alpha s_\beta s_\gamma - c_\alpha c_\gamma & s_\alpha s_\beta c_\gamma - c_\alpha s_\gamma \\ -s_\beta & c_\beta s_\gamma & c_\beta c_\gamma \end{pmatrix} \quad (\text{A.2})$$

Angle-axis (θ, \hat{w}) :

$${}^jR_i = \begin{pmatrix} w_x^2 v_\theta + c_\theta & w_x w_y v_\theta - w_z s_\theta & w_x w_y v_\theta + w_y s_\theta \\ w_x w_y v_\theta + w_z s_\theta & w_y^2 v_\theta + c_\theta & w_y w_z v_\theta - w_x s_\theta \\ w_x w_z v_\theta - w_y s_\theta & w_y w_z v_\theta + w_x s_\theta & w_z^2 v_\theta + c_\theta \end{pmatrix} \quad (\text{A.3})$$

Unit quaternions $(q_0 \ q_1 \ q_2 \ q_3)^T$:

$${}^jR_i = \begin{pmatrix} 1 - 2(q_y^2 + q_z^2) & 2(q_x q_y - q_0 q_z) & 2(q_y q_z + q_0 q_x) \\ 2(q_x q_y + q_0 q_z) & 1 - 2(q_x^2 + q_z^2) & 2(q_y q_z - q_0 q_x) \\ 2(q_x q_z - q_x q_y) & 2(q_y q_z + q_0 q_x) & 1 - 2(q_x^2 + q_y^2) \end{pmatrix} \quad (\text{A.4})$$

A.2 Euler Angles

For a minimal representation, the orientation of coordinate frame i relative to coordinate frame j can be denoted as a vector of three angles (α, β, γ) . These angles are known as Euler angles when each represents a rotation about an axis of a moving coordinate frame. In this way, the location of the axis of each successive rotation depends upon the preceding rotation, so the order of the rotations must accompany the three angles to define the orientation.

For example, the symbols (α, β, γ) are often used to indicate $Z - Y - X$ Euler angles. Specifically, taking the moving frame i and the fixed frame j to be initially coincident, α is the rotation about the \hat{z} axis of frame i , β is the rotation about the rotated \hat{y} axis of frame i , and finally, γ is the rotation about the twice rotated \hat{x} axis of frame i . Regardless of the order of rotations, an Euler angle representation of orientation always exhibits a singularity when the first and last rotations both occur about the same axis. This particular set of Euler angles originates from a representation of orientation in the aeronautical field. These are called *Roll-Pitch-Yaw* angles, or also *Bank-Attitude-Heading* respectively, to denote the typical changes of attitude of an aircraft.

A.2.1 Conversion formulas

Equivalent rotation matrices for various representations of orientation are:

Unit quaternions $(q_0 \ q_1 \ q_2 \ q_3)^T$:

$$\begin{aligned}\alpha &= \tan^{-1} \frac{2(q_0 q_z - q_x q_y)}{1 - 2(q_y^2 + q_z^2)} \\ \beta &= \sin^{-1} (2(q_0 q_y + q_z q_x)) \\ \gamma &= \tan^{-1} \frac{2(2(q_0 q_y - q_y q_z))}{1 - 2(q_x^2 + q_y^2)}\end{aligned}\tag{A.5}$$

Rotation matrix jR_i :

$$\begin{aligned}\alpha &= \tan^{-1} \left(\frac{r_{23}}{r_{13}} \right) \\ \beta &= \tan^{-1} \left(\frac{\sqrt{r_{13}^2 + r_{23}^2}}{r_{33}} \right) \\ \gamma &= \tan^{-1} \left(\frac{r_{32}}{-r_{31}} \right)\end{aligned}\tag{A.6}$$

A.3 Axis and angles

A single angle θ in combination with a unit vector $\hat{\mathbf{w}}$ can also denote the orientation of coordinate frame i relative to coordinate frame j . In this case, frame i is rotated through the angle θ about an axis defined by the vector $\hat{\mathbf{w}} = (w_x \ w_y \ w_z)^T$, relative to frame j . The vector $\hat{\mathbf{w}}$ is sometimes referred to as the equivalent axis of a finite rotation. The auxiliary relationship that resolves that is the unit magnitude of vector $\hat{\mathbf{w}}$. Even with this auxiliary relationship, the angle-axis representation is not unique because rotation through an angle of $-\theta$ about $-\hat{\mathbf{w}}$ is equivalent to a rotation through θ about $\hat{\mathbf{w}}$.

A.3.1 Conversion formulas

Equivalent angle axis for various representations of orientation are:

Rotation matrix jR_i :

$$\theta = \cos^{-1} \left(\frac{r_{11} + r_{22} + r_{33} - 4}{2} \right)$$

$$\mathbf{r} = \frac{1}{2 \sin \theta} \begin{bmatrix} r_{32} - r_{23} \\ r_{13} - r_{31} \\ r_{21} - r_{12} \end{bmatrix} \quad (\text{A.7})$$

Unit quaternions $\hat{\mathbf{q}} = (q_0 \ q_1 \ q_2 \ q_3)^T$:

$$\theta = 2 \cdot \cos^{-1}(q_0) \quad , \quad \hat{\mathbf{w}} = \frac{\hat{\mathbf{q}}}{\|\hat{\mathbf{q}}\|} \quad (\text{A.8})$$

An axis and angle representation can be found combined into a rotation vector $r = \hat{\mathbf{w}}\theta$. In this case, conversion from and to a quaternion is given:

$$\mathbf{q} = \exp\left(-\frac{1}{2}r\right) \quad , \quad r = -2 \log(\mathbf{q}) \quad (\text{A.9})$$

where the quaternion logarithm is defined in Equation A.14.

A.4 Quaternions

The drawbacks of the angle and axis representation can be overcome by a different four-parameters representation, namely the unit quaternion [136]. The quaternion representation of orientation is first defined in [137] and largely superseded by the simpler vector representation of [138]; it is extremely useful for problems in robotics that result in representational singularities in the vector/matrix notation [139]. Quaternions do not suffer from singularities as Euler angles do.

A quaternion \mathbf{q} is a generalization of complex number to 4-dimensional space, and is defined as:

$$\mathbf{q} := (q_0 \ \hat{\mathbf{q}})^T := (q_0 \ q_x \ q_y \ q_z)^T := q_0 + q_x \mathbf{i} + q_y \mathbf{j} + q_z \mathbf{k} \quad (\text{A.10})$$

where the components q_0 , q_x , q_y , q_z are scalars, sometimes referred to as Euler parameters, and i , j , and k are operators.

A.4.1 Quaternion operations

The *conjugate* of a quaternion is defined as:

$$\mathbf{q}^* := (q_0 - \hat{\mathbf{q}})^T \quad (\text{A.11})$$

Addition and subtraction of quaternions is defined as:

$$\begin{aligned} \mathbf{q}_A \pm \mathbf{q}_B &:= (q_{0A} + q_{xA}\mathbf{i} + q_{yA}\mathbf{j} + q_{zA}\mathbf{k}) \pm (q_{0B} + q_{xB}\mathbf{i} + q_{yB}\mathbf{j} + q_{zB}\mathbf{k}) \\ &:= (q_{0A} \pm q_{0B}) + (q_{xA} \pm q_{xB})\mathbf{i} + (q_{yA} \pm q_{yB})\mathbf{j} + (q_{zA} \pm q_{zB})\mathbf{k} \end{aligned} \quad (\text{A.12})$$

Quaternion *multiplication* is defined as:

$$\begin{aligned} \mathbf{q}_A \otimes \mathbf{q}_B &:= (q_{0A} + q_{xA}\mathbf{i} + q_{yA}\mathbf{j} + q_{zA}\mathbf{k})(q_{0B} + q_{xB}\mathbf{i} + q_{yB}\mathbf{j} + q_{zB}\mathbf{k}) \\ &= (q_{0A}q_{0B} - q_{xA}q_{xB} - q_{yA}q_{yB} - q_{zA}q_{zB}) \\ &\quad (q_{0A}q_{xB} + q_{xA}q_{0B} + q_{yA}q_{zB} - q_{zA}q_{yB})\mathbf{i} + \\ &\quad (q_{0A}q_{yB} - q_{xA}q_{zB} + q_{yA}q_{0B} + q_{zA}q_{xB})\mathbf{j} + \\ &\quad (q_{0A}q_{zB} + q_{xA}q_{zB} - q_{yA}q_{xB} + q_{zA}q_{0B})\mathbf{k} \end{aligned} \quad (\text{A.13})$$

The natural *logarithm* of a quaternion is defined as:

$$\log \mathbf{q} = \left(\log \|\mathbf{q}\| \quad \frac{\mathbf{q}}{\|\mathbf{q}\|} \cos^{-1} \frac{q_0}{\|\mathbf{q}\|} \right) \quad (\text{A.14})$$

A.5 Metric on SO(3) space

The position and orientation of a body can also be expressed in a unified fashion with an exponential mapping. This approach is introduced first with its application to pure rotation and expanded to rigid-body motion. More details on the approach can be found in [140] [141].

The set of all orthogonal matrices with determinant 1, which is the set of all rotation matrices \mathbf{R} , is a group under the operation of matrix multiplication denoted as $SO(3) \subset \mathbb{R}^{3 \times 3}$ [142]. This stands for *special* orthogonal wherein *special* alludes to the $\det \mathbf{R} = 1$ instead of ± 1 .

The group of rigid body rotations is defined as

$$SO(3) = \{\mathbf{R} \in \mathbb{R}^{3 \times 3} : \det \mathbf{R} = 1, \mathbf{R}^T \mathbf{R} = \mathbf{I}_3\} \quad (\text{A.15})$$

A rotation matrix \mathbf{R} can be viewed as a map between a space frame $S \subset \mathbb{R}^{3 \times 3}$ and any body (moving) frame $M \subset \mathbb{R}^{3 \times 3}$, i.e. $R : M \rightarrow S$.

The set of rotation matrices satisfies the four axioms of a group:

$$\begin{aligned}
 \text{closure :} & & \mathbf{R}_1 \mathbf{R}_2 & \in SO(3) \quad \forall \mathbf{R}_1, \mathbf{R}_2 \in SO(3); \\
 \text{identity :} & & \mathbf{I}_{3 \times 3} \mathbf{R} = \mathbf{R} \mathbf{I}_{3 \times 3} & = \mathbf{3} \quad \forall \mathbf{R} \in SO(3); \\
 \text{inverse :} & & \mathbf{R}^T & \in SO(3) \text{ is the unique inverse of } \mathbf{R} \forall \mathbf{R} \in SO(3); \\
 \text{associativity :} & & (\mathbf{R}_1 \mathbf{R}_2) \mathbf{R}_3 & = \mathbf{R}_1 (\mathbf{R}_2 \mathbf{R}_3) \quad \forall \mathbf{R}_1, \mathbf{R}_2, \mathbf{R}_3 \in SO(3).
 \end{aligned}$$

Given a trajectory in $SO(3)$. *i.e.* $\mathbf{R}(t) : \mathbb{R}^{3 \times 3} \rightarrow SO(3)$, two important quantities can be defined

- $\hat{\Omega} := \frac{d\mathbf{R}}{dt} \cdot \mathbf{R}^{-1}$, where $\Omega \in \mathbb{R}^{3 \times 3}$ is the *space angular velocity*
- $\hat{\omega} := \mathbf{R}^{-1} \cdot \frac{d\mathbf{R}}{dt}$, where $\omega \in \mathbb{R}^{3 \times 3}$ is the *body angular velocity*

Do note that, for any $\mathbf{R} \in SO(3)$, both $\frac{d\mathbf{R}}{dt} \cdot \mathbf{R}^{-1}$ and $\mathbf{R}^{-1} \cdot \frac{d\mathbf{R}}{dt}$ are skew-symmetric matrices, *i.e.* elements of

$$so(3) = \{\mathbf{A} \in \mathbb{R}^{3 \times 3} : \mathbf{A} + \mathbf{A}^T = 0\} \quad (\text{A.16})$$

and the *hat* of skew operator $\hat{\cdot} : \mathbb{R}^{3 \times 3} \rightarrow so(3)$ transforms 3D vectors in skew-symmetric matrices, particularly

$$\hat{\mathbf{a}} = \frac{\partial}{\partial \mathbf{b}}(\mathbf{a} \times \mathbf{b}) = \begin{pmatrix} 0 & -a_3 & a_2 \\ a_3 & 0 & -a_1 \\ -a_2 & a_1 & 0 \end{pmatrix} \quad (\text{A.17})$$

The inverse operator, *vee* or *deskew*, simply returns a 3D vector from a skew-symmetric matrix.

A body spinning at constant angular velocity ω , after a unit time, will undergo a rotation by an angle $\|\omega\|$, as expressed by the Rodrigues' formula [76], also expressed as $\exp(\hat{\omega})$

$$e^{\hat{\omega}} = \mathbf{R} = \mathbf{I} + \frac{\hat{\omega}}{\|\omega\|} \sin\|\omega\| + \frac{\hat{\omega}^2}{\|\omega\|^2} (1 - \cos\|\omega\|) \quad (\text{A.18})$$

The inverse of the exponential map, *i.e.* the logarithm map returns as output a vector which represents the axis of rotation of module equal to θ ,

$$\log(\mathbf{R}) = \hat{\omega} = \frac{\mathbf{R} - \mathbf{R}^T}{2 \sin(\cos^{-1}(\frac{\text{Tr}(\mathbf{R}) - 1}{2}))} \quad (\text{A.19})$$

Appendix B

Coordinate frames

The coordinate frames used for mathematical formulation of inertial navigation mechanization, shown in Figure B.1, are the following:

- **Body Frame (\mathbf{B}):** is the coordinate frame of the moving body. It is referred to the specific system used to detect the orientation of the body (*e.g.* magneto-inertial measurement sensors or optical motion tracking systems).
- **Body M-IMU Frame (\mathbf{S}):** is the coordinate frame of the moving M-IMU. Its origin is located in the center of the accelerometer triad and it is aligned to the casing. All the inertial measurements are solved in this frame;
- **Body Optical Motion Tracker Frame (\mathbf{M}):** this is a moving frame defined by the position of the LED markers fixed on the body. To define this frame at least three markers are needed, as shown in Section 3.2.4.
- **Local-Level Frame (\mathbf{L}):** this frame is defined by a plane locally tangent to the surface of the earth at the position of the M-IMU. This implies a constant direction for gravity (straight down). The coordinate system used in Easting, Northing, Up (ENU), where Up is the normal vector of the plane, North points toward the spin axis of Earth on the plane, and East completes the orthogonal system;
- **Inertial Frame (\mathbf{I}):** this is the canonical frame for an object near the surface of the Earth. It is a non-rotating, non-accelerating frame of reference with a Cartesian coordinate system, whose x-axis is aligned with the mean vernal equinox and whose z-axis is coaxial with the spin axis of the Earth. The y-axis completes an orthogonal basis and the system's origin is located at the center of mass of the Earth;

- **Optical Motion Tracker Frame (O):** this frame is fixed by a particular protocol defined by the software of the specific optical motion tracking system used. In particular, all the markers position is given with reference to the origin of this frame.
- **Earth Frame (E):** the origin of this reference frame is at the Earth's center of mass. Its z-axis coincides with the Inertial frame (I), but it rotates with respect to I at the Earth rotation rate, which is approximately 15 degrees per hour.

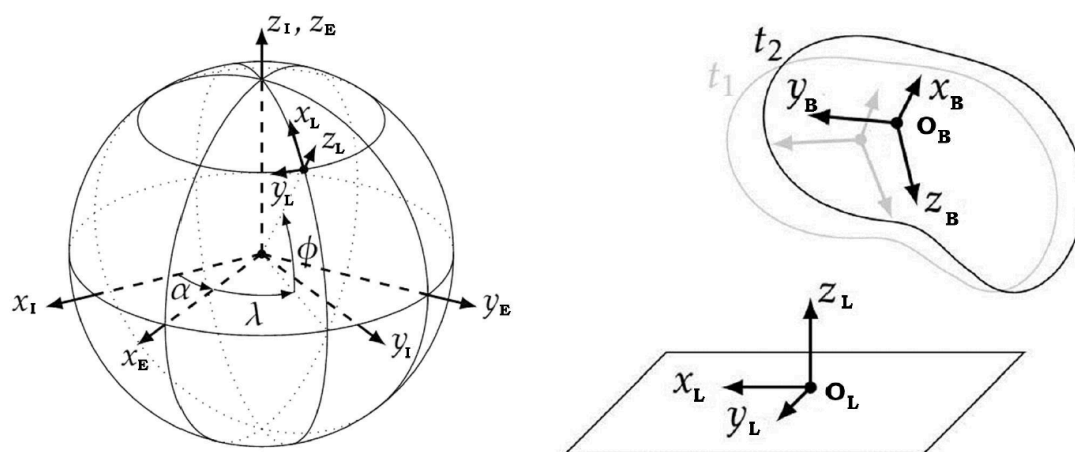


Fig. B.1 The figure illustrates the set of coordinate frames involved in the inertial navigation framework. On the left, the inertial (I) and the Earth's (E) frames are defined with respect to the Earth along with the position (latitude λ , longitude ϕ) of an hypothetical local frame (L). On the right, the body (B) at time t_1 and t_2 with respect to a local navigation frame is shown.

The mechanization of the inertial navigation can be formulated in any of the last three coordinate systems, and, once defined, it is common to refer to this frame as the navigation frame (N). The Local-level frame has been used as Navigation frame for the mechanization formulation.

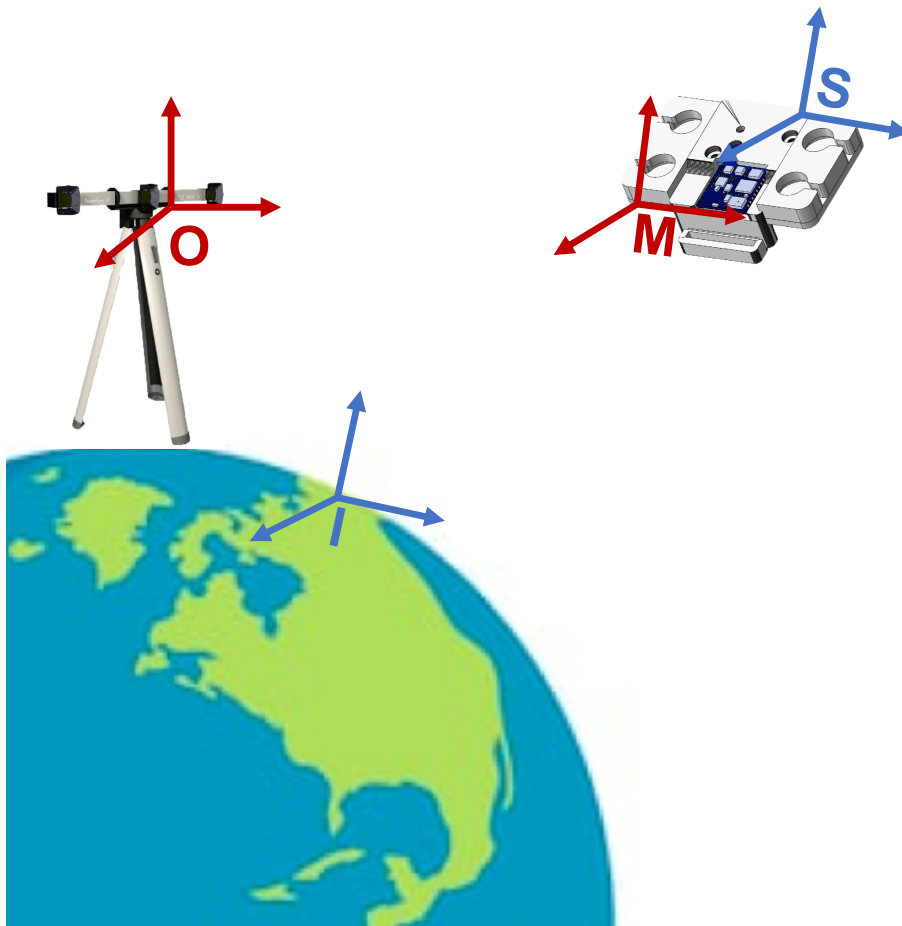


Fig. B.2 The figure illustrates the set of coordinate frames involved in the system orientation detection. The motion tracker defines its own fixed reference frame (O) based on a vendor protocol, and it also defines with marker trackers its moving body frame (M). With M-IMU is also defined a fixed reference frame, *i.e.* the Inertial frame (I) and a moving frame (S)

Tesi di dottorato in Bioingegneria e bioscienze, di Jacopo Tosi,
discussa presso l'Università Campus Bio-Medico di Roma in data 28/05/2019.
La disseminazione e la riproduzione di questo documento sono consentite per scopi di didattica e ricerca,
a condizione che ne venga citata la fonte.

References

- [1] Matteo Contaldo, Budhaditya Banerjee, David Ruffieux, Jérémie Chabloz, Erwan Le Roux, and Christian C. Enz. A 2.4-GHz BAW-Based Transceiver for Wireless Body Area Networks. *IEEE Transactions on Biomedical Circuits and Systems*, 4(6):391–399, 12 2010.
- [2] M. Gentili, R. Sannino, and M. Petracca. BlueVoice: Voice communications over Bluetooth Low Energy in the Internet of Things scenario. *Computer Communications*, 89-90:51–59, 9 2016.
- [3] Luca Ricci, Fabrizio Taffoni, and Domenico Formica. On the orientation error of IMU: Investigating static and dynamic accuracy targeting human motion. *PLoS ONE*, 11(9):e0161940, 9 2016.
- [4] Álvaro Sánchez-Ferro, Morad Elshehabi, Catarina Godinho, Dina Salkovic, Markus A. Hobert, Josefa Domingos, Janet MT. van Uem, Joaquim J. Ferreira, and Walter Maetzler. New methods for the assessment of Parkinson's disease (2005 to 2015): A systematic review. *Movement Disorders*, 31(9):1283–1292, 9 2016.
- [5] Lazzaro di Biase, Susanna Summa, Jacopo Tosi, Fabrizio Taffoni, Massimo Marano, Angelo Cascio Rizzo, Fabrizio Vecchio, Domenico Formica, Vincenzo Di Lazzaro, Giovanni Di Pino, and Mario Tombini. Quantitative analysis of bradykinesia and rigidity in Parkinson's disease. *Frontiers in Neurology*, 9(MAR):121, 3 2018.
- [6] Werner Poewe, Klaus Seppi, Caroline M. Tanner, Glenda M. Halliday, Patrik Brundin, Jens Volkman, Anette-Eleonore Schrag, and Anthony E. Lang. Parkinson disease. *Nature Reviews Disease Primers*, 3:17013, 3 2017.
- [7] Hande Alemdar and Cem Ersoy. Wireless sensor networks for healthcare: A survey. *Computer Networks*, 54(15):2688–2710, 2010.
- [8] O Omeni, A C W Wong, A J Burdett, and C Toumazou. Energy Efficient Medium Access Protocol for Wireless Medical Body Area Sensor Networks. *IEEE Transactions on Biomedical Circuits and Systems*, 2(4):251–259, 2008.
- [9] J Seo, J Heo, S Lim, J Ahn, and W Kim. A Study on the Implementation of a Portable u-Healthcare System using SNMP and AODV. In *2007 29th Annual International Conference of the IEEE Engineering in Medicine and Biology Society*, pages 1519–1522, 2007.

- [10] M Ghamari, H Arora, R S Sherratt, and W Harwin. Comparison of low-power wireless communication technologies for wearable health-monitoring applications. In *2015 International Conference on Computer, Communications, and Control Technology (I4CT)*, pages 1–6, 2015.
- [11] Alf Helge Omre. Bluetooth low energy: wireless connectivity for medical monitoring. *Journal of diabetes science and technology*, 4(2):457–63, 3 2010.
- [12] Atena Roshan Fekr, Katarzyna Radecka, and Zeljko Zilic. Design and Evaluation of an Intelligent Remote Tidal Volume Variability Monitoring System in E-Health Applications. *IEEE Journal of Biomedical and Health Informatics*, 19(5):1532–1548, 9 2015.
- [13] Xenofon Fafoutis, Antonis Vafeas, Balazs Janko, R. Simon Sherratt, James Pope, Atis Elsts, Evangelos Mellios, Geoffrey Hilton, George Oikonomou, Robert Piechocki, and Ian Craddock. Designing Wearable Sensing Platforms for Healthcare in a Residential Environment. *EAI Endorsed Transactions on Pervasive Health and Technology*, 3(12):153063, 9 2017.
- [14] Micaela Del Fabbro Arcopinto, Jacopo Tosi, Domenico Formica, and Fabrizio Taffoni. Monitoring Sucking Abilities in Newborns: Design and Validation on Adult Of a Wearable System for Non-Invasive Deglutition Detection. In *2018 40th Annual International Conference of the IEEE Engineering in Medicine and Biology Society (EMBC)*, pages 4257–4260. IEEE, 7 2018.
- [15] Young-jin Park and Hui-sup Cho. Transmission of ECG data with the patch-type ECG sensor system using Bluetooth Low Energy. In *2013 International Conference on ICT Convergence (ICTC)*, pages 289–294. IEEE, 10 2013.
- [16] Vega Pradana Rachim and Wan-Young Chung. Wearable Noncontact Armband for Mobile ECG Monitoring System. *IEEE Transactions on Biomedical Circuits and Systems*, 10(6):1112–1118, 12 2016.
- [17] Liu Guo-cheng and Yu Hong-yang. Design and implementation of a Bluetooth 4.0-based heart rate monitor system on iOS platform. In *2013 International Conference on Communications, Circuits and Systems (ICCCAS)*, pages 112–115. IEEE, 11 2013.
- [18] Alexander M. Chan, Nandakumar Selvaraj, Nima Ferdosi, and Ravi Narasimhan. Wireless patch sensor for remote monitoring of heart rate, respiration, activity, and falls. In *2013 35th Annual International Conference of the IEEE Engineering in Medicine and Biology Society (EMBC)*, pages 6115–6118. IEEE, 7 2013.
- [19] K. Kuwabara, Y. Higuchi, T. Ogasawara, H. Koizumi, and T. Haga. Wearable blood flowmeter appessory with low-power laser Doppler signal processing for daily-life healthcare monitoring. In *2014 36th Annual International Conference of the IEEE Engineering in Medicine and Biology Society*, pages 6274–6277. IEEE, 8 2014.
- [20] Davide Brunelli, Elisabetta Farella, Davide Giovanelli, Bojan Milosevic, and Ivan Minakov. Design Considerations for Wireless Acquisition of Multichannel sEMG Signals in Prosthetic Hand Control. *IEEE Sensors Journal*, pages 1–1, 2016.

- [21] J. Pedro Amaro, Sergio Patrao, Fernando Moita, and Luis Roseiro. Bluetooth low energy profile for MPU9150 IMU data transfers. In *2017 IEEE 5th Portuguese Meeting on Bioengineering (ENBENG)*, pages 1–4. IEEE, 2017.
- [22] Jiun-ren Lin, Timothy Talty, and Ozan Tonguz. On the potential of bluetooth low energy technology for vehicular applications. *IEEE Communications Magazine*, 53(1):267–275, 1 2015.
- [23] Kun Xia, Haibo Wang, Nan Wang, Wei Yu, and Tong Zhou. Design of automobile intelligence control platform based on Bluetooth low energy. In *2016 IEEE Region 10 Conference (TENCON)*, pages 2801–2805. IEEE, 11 2016.
- [24] Shiwei Luan, Dana Gude, Punit Prakash, and Steve Warren. A paraeducator glove for counting disabled-child behaviors that incorporates a Bluetooth Low Energy wireless link to a smart phone. In *2014 36th Annual International Conference of the IEEE Engineering in Medicine and Biology Society*, pages 796–799. IEEE, 8 2014.
- [25] Paul K. Yoon, Shaghayegh Zihajehzadeh, Bong-Soo Kang, and Edward J. Park. Adaptive Kalman filter for indoor localization using Bluetooth Low Energy and inertial measurement unit. In *2015 37th Annual International Conference of the IEEE Engineering in Medicine and Biology Society (EMBC)*, pages 825–828. IEEE, 8 2015.
- [26] R. Simon Sherratt, Balazs Janko, Terence Hui, William Harwin, and Daniel Diaz-Sanchez. Dictionary memory based software architecture for distributed Bluetooth Low Energy host controllers enabling high coverage in consumer residential healthcare environments. In *2017 IEEE International Conference on Consumer Electronics (ICCE)*, pages 406–407. IEEE, 2017.
- [27] Mario Collotta, Giovanni Pau, Mario Collotta, and Giovanni Pau. A Solution Based on Bluetooth Low Energy for Smart Home Energy Management. *Energies*, 8(10):11916–11938, 10 2015.
- [28] Mario Collotta and Giovanni Pau. A Novel Energy Management Approach for Smart Homes Using Bluetooth Low Energy. *IEEE Journal on Selected Areas in Communications*, 33(12):2988–2996, 12 2015.
- [29] Mario Collotta and Giovanni Pau. An Innovative Approach for Forecasting of Energy Requirements to Improve a Smart Home Management System Based on BLE. *IEEE Transactions on Green Communications and Networking*, 1(1):112–120, 3 2017.
- [30] Junfei Tian, Jingen Liu, Shengyun Liang, Yunkun Ning, Huiqi Li, and Guoru Zhao. Wireless transmission system for motion sensing game controller based on low power Bluetooth technology. In *2016 IEEE 13th International Conference on Signal Processing (ICSP)*, pages 1318–1322. IEEE, 11 2016.
- [31] Rushab Karani, Shivank Dhote, Naman Khanduri, Anushree Srinivasan, Rahul Sawant, Ganesh Gore, and Jonathan Joshi. Implementation and design issues for using Bluetooth low energy in passive keyless entry systems. In *2016 IEEE Annual India Conference (INDICON)*, pages 1–6. IEEE, 12 2016.

- [32] Wittaya Koodtalang and Thaksin Sangsuwan. Improving motorcycle anti-theft system with the use of Bluetooth Low Energy 4.0. In *2016 International Symposium on Intelligent Signal Processing and Communication Systems (ISPACS)*, pages 1–5. IEEE, 10 2016.
- [33] Anas Basalamah. Sensing the Crowds Using Bluetooth Low Energy Tags. *IEEE Access*, 4:4225–4233, 2016.
- [34] Jacopo Tosi, Fabrizio Taffoni, Marco Santacatterina, Roberto Sannino, and Domenico Formica. Performance evaluation of bluetooth low energy: A systematic review. *Sensors (Switzerland)*, 17(12):2898, 12 2017.
- [35] Kevin Townsend, Carles Cufi, Akiba, and Robert Davidson. Protocol Basics. In *Getting Started with Bluetooth Low Energy: Tools and Techniques for Low-Power Networking*, pages 15–34. O’Reilly Media, Inc.: 1005 Gravenstein Highway North, Sebastopol, {CA} 95472, sawyer, b. edition, 2014.
- [36] Kevin Heydon. Architecture. In *Bluetooth Low Energy - The Developer’s Handbook*, pages 40–51. Prantice Hall- Pearson Education, Inc.: One Lake Street, Upper Saddle River, New Jersey 07458, goodwin, b edition, 2012.
- [37] Carles Gomez, Joaquim Oller, and Josep Paradells. Overview and Evaluation of Bluetooth Low Energy: An Emerging Low-Power Wireless Technology. *Sensors*, 12(9):11734–11753, 2012.
- [38] Naresh Kumar Gupta. *Inside Bluetooth Low Energy, Second Edition*. Artech House, 2016.
- [39] Kevin Heydon. The Host/Controller Interface. In *Bluetooth Low Energy - The Developer’s Handbook*, pages 131–163. Prantice Hall- Pearson Education, Inc.: One Lake Street, Upper Saddle River, New Jersey 07458, goodwin, b edition, 2012.
- [40] Kevin Townsend, Carles Cufi, Akiba, and Robert Davidson. {GAP} (Advertising and Connections). In *Getting Started with Bluetooth Low Energy: Tools and Techniques for Low-Power Networking.*, pages 35–50. O’Reilly Media, Inc.: 1005 Gravenstein Highway North, Sebastopol, {CA} 95472, sawyer, b. edition, 2014.
- [41] BluetoothSIG. Vol 6: Core System Package [Low Energy Specification], Part B: Link Layer Specification. In *Specification of the Bluetooth® System, Covered Core Package version: 5.0*, pages 2547–2694. The Bluetooth Special Interest Group: Kirkland, WA, USA, 2010, 2016.
- [42] Kevin Townsend, Carles Cufi, Akiba, and Robert Davidson. Introduction. In *Getting Started with Bluetooth Low Energy: Tools and Techniques for Low-Power Networking*, pages 1–14. O’Reilly Media, Inc.: 1005 Gravenstein Highway North, Sebastopol, {CA} 95472, sawyer, b. edition, 2014.
- [43] BluetoothSIG. Vol 1: Architecture & Terminology Overview, Part A: Architecture. In *Specification of the Bluetooth® System, Covered Core Package version: 5.0*, pages 161–264. The Bluetooth Special Interest Group: Kirkland, WA, USA, 2010, 2016.

- [44] J Tosi, F Taffoni, M Santacatterina, R Sannino, and D Formica. Throughput Analysis of BLE Sensor Network for Motion Tracking of Human Movements. *IEEE Sensors Journal*, 19(1):370–377, 2019.
- [45] R Want, B Schilit, and D Laskowski. Bluetooth LE Finds Its Niche. *IEEE Pervasive Computing*, 12(4):12–16, 2013.
- [46] Alessandro Filippeschi, Norbert Schmitz, Markus Miezal, Gabriele Bleser, Emanuele Ruffaldi, and Didier Stricker. Survey of motion tracking methods based on inertial sensors: A focus on upper limb human motion, 6 2017.
- [47] Pietro Picerno, Andrea Cereatti, and Aurelio Cappozzo. A spot check for assessing static orientation consistency of inertial and magnetic sensing units. *Gait and Posture*, 33(3):373–378, 3 2011.
- [48] Gregory Dudek and Michael Jenkin. Inertial Sensing, GPS and Odometry. In *Springer Handbook of Robotics*, pages 737–752. Springer International Publishing, Cham, 2016.
- [49] Ya Tian, Hongxing Wei, and Jindong Tan. An Adaptive-Gain Complementary Filter for Real-Time Human Motion Tracking With MARG Sensors in Free-Living Environments. *IEEE Transactions on Neural Systems and Rehabilitation Engineering*, 21(2):254–264, 3 2013.
- [50] Rong Zhu and Zhaoying Zhou. A real-time articulated human motion tracking using tri-axis inertial/magnetic sensors package. *IEEE Transactions on Neural Systems and Rehabilitation Engineering*, 12(2):295–302, 6 2004.
- [51] Robert Mahony, Tarek Hamel, and Jean Michel Pflimlin. Nonlinear complementary filters on the special orthogonal group. *IEEE Transactions on Automatic Control*, 53(5):1203–1218, 6 2008.
- [52] W T Fong, S K Ong, and A. Y.C. Nee. Methods for in-field user calibration of an inertial measurement unit without external equipment. *Measurement Science and Technology*, 19(8):085202, 8 2008.
- [53] Stefan Stadler and Pratul K. Ajmera. Sensors and materials : an international journal on sensor technology. *Sensors and materials*, 14(3):151–166, 2008.
- [54] Salvatore Sessa, Massimiliano Zecca, Zhuohua Lin, Luca Bartolomeo, Hiroyuki Ishii, and Atsuo Takanishi. A methodology for the performance evaluation of inertial measurement units. *Journal of Intelligent and Robotic Systems: Theory and Applications*, 71(2):143–157, 8 2013.
- [55] Joost C. Lötters, Jeroen Schipper, Peter H. Veltink, Wouter Olthuis, and Piet Bergveld. Procedure for in-use calibration of triaxial accelerometers in medical applications. *Sensors and Actuators, A: Physical*, 68(1-3):221–228, 6 1998.
- [56] D. Campolo, M. Fabris, G. Cavallo, D. Accoto, F. Keller, and E. Guglielmelli. A novel procedure for in-field calibration of sourceless inertial/magnetic orientation tracking wearable devices. In *Proceedings of the First IEEE/RAS-EMBS International*

- Conference on Biomedical Robotics and Biomechatronics, 2006, BioRob 2006*, volume 2006, pages 471–476. IEEE, 2006.
- [57] Demoz Gebre-Egziabher, Gabriel H Elkaim, J David Powell, and Bradford W Parkinson. Calibration of strapdown magnetometers in magnetic field domain. *Journal of Aerospace Engineering*, 19(2):87–102, 2006.
- [58] J. F. Vasconcelos, G. Elkaim, C. Silvestre, P. Oliveira, and B. Cardeira. Geometric Approach to Strapdown Magnetometer Calibration in Sensor Frame. *IEEE Transactions on Aerospace and Electronic Systems*, 47(2):1293–1306, 4 2011.
- [59] Michael J Caruso. Applications of magnetoresistive sensors in navigation systems. Technical report, SAE Technical Paper, 1997.
- [60] Jmg Merayo and P Brauer. Scalar calibration of vector magnetometers. *Measurement ...*, 11(2):120–132, 2 2000.
- [61] S. Bonnet, C. Bassompierre, C. Godin, S. Lesecq, and A. Barraud. Calibration methods for inertial and magnetic sensors. *Sensors and Actuators, A: Physical*, 156(2):302–311, 12 2009.
- [62] Timo Pylvänäinen. Automatic and adaptive calibration of 3D field sensors. *Applied Mathematical Modelling*, 32(4):575–587, 4 2008.
- [63] Martin Šipoš, Pavel Pačes, Jan Roháč, and Petr Nováček. Analyses of triaxial accelerometer calibration algorithms. *IEEE Sensors Journal*, 12(5):1157–1165, 5 2012.
- [64] C. C. Foster and G. H. Elkaim. Extension of a two-step calibration methodology to include nonorthogonal sensor axes. *IEEE Transactions on Aerospace and Electronic Systems*, 44(3):1070–1078, 7 2008.
- [65] Manon Kok and Thomas B. Schön. Maximum likelihood calibration of a magnetometer using inertial sensors. *IFAC Proceedings Volumes (IFAC-PapersOnline)*, 19(3):92–97, 1 2014.
- [66] Sebastian Madgwick. An efficient orientation filter for inertial and inertial/magnetic sensor arrays. *Report x-io and University of Bristol (UK)*, 25:113–118, 2010.
- [67] R. E. Kalman. A New Approach to Linear Filtering and Prediction Problems. *Journal of Basic Engineering*, 82(1):35, 3 1960.
- [68] A. D. Young. Comparison of orientation filter algorithms for realtime wireless inertial posture tracking. In *Proceedings - 2009 6th International Workshop on Wearable and Implantable Body Sensor Networks, BSN 2009*, pages 59–64. IEEE, 6 2009.
- [69] Angelo M. Sabatini. Quaternion-based extended Kalman filter for determining orientation by inertial and magnetic sensing. *IEEE Transactions on Biomedical Engineering*, 53(7):1346–1356, 7 2006.
- [70] Greg Welch and Gary Bishop. An Introduction to the Kalman Filter. Technical report, Department of Computer Science University of North Carolina at Chapel Hill Chapel Hill, NC 27599-3175, Chapel Hill, NC, USA, 1995.

- [71] Sebastian O.H. Madgwick, Andrew J.L. Harrison, and Ravi Vaidyanathan. Estimation of IMU and MARG orientation using a gradient descent algorithm. In *IEEE International Conference on Rehabilitation Robotics*, pages 1–7. IEEE, 6 2011.
- [72] Monique Paulich, Martin Schepers, Nina Rudigkeit, and Giovanni Bellusci. Xsens MTw Awinda: Miniature Wireless Inertial-Magnetic Motion Tracker for Highly Accurate 3D Kinematic Applications. Technical report, Xsens, 2018.
- [73] Walter T. Higgins. A Comparison of Complementary and Kalman Filtering. *IEEE Transactions on Aerospace and Electronic Systems*, AES-11(3):321–325, 5 1975.
- [74] Domenico Campolo, Luca Schenato, Lijuan Pi, Xinyan Deng, and Eugenio Guglielmelli. Attitude estimation of a biologically inspired robotic housefly via multimodal sensor fusion. *Advanced Robotics*, 23(7-8):955–977, 1 2009.
- [75] Domenico Campolo, Flavio Keller, and Eugenio Guglielmelli. Inertial/Magnetic Sensors Based Orientation Tracking on the Group of Rigid Body Rotations with Application to Wearable Devices. In *2006 IEEE/RSJ International Conference on Intelligent Robots and Systems*, pages 4762–4767. IEEE, 10 2006.
- [76] Richard M. Murray, Zexiang Li, and Shankar. Sastry. *A mathematical introduction to robotic manipulation*. CRC Press, 1994.
- [77] Eric R. Bachmann, Robert B. McGhee, Xiaoping Yun, and Michael J. Zyda. Inertial and magnetic posture tracking for inserting humans into networked virtual environments. In *Proceedings of the ACM symposium on Virtual reality software and technology - VRST '01*, page 9, New York, New York, USA, 2001. ACM Press.
- [78] F.C. Park and B.J. Martin. Robot sensor calibration: solving $AX=XB$ on the Euclidean group. *IEEE Transactions on Robotics and Automation*, 10(5):717–721, 1994.
- [79] Junhyoung Ha, Donghoon Kang, and Frank C. Park. A Stochastic Global Optimization Algorithm for the Two-Frame Sensor Calibration Problem. *IEEE Transactions on Industrial Electronics*, 63(4):2434–2446, 4 2016.
- [80] C. C. Finlay, S. Maus, C. D. Beggan, T. N. Bondar, A. Chambodut, T. A. Chernova, A. Chulliat, V. P. Golovkov, B. Hamilton, M. Hamoudi, R. Holme, G. Hulot, W. Kuang, B. Langlais, V. Lesur, F. J. Lowes, H. Lühr, S. Macmillan, M. Manda, S. McLean, C. Manoj, M. Menvielle, I. Michaelis, N. Olsen, J. Rauberg, M. Rother, T. J. Sabaka, A. Tangborn, L. Tøffner-Clausen, E. Thébault, A. W.P. Thomson, I. Wardinski, Z. Wei, and T. I. Zvereva. International Geomagnetic Reference Field: The eleventh generation. *Geophysical Journal International*, 183(3):1216–1230, 12 2010.
- [81] Li Zhigang, Wang Dandan, and Hu Tao. Numerical simulation of inertial navigation technology and arbitrary path generator. In *Proceedings - 2014 4th International Conference on Instrumentation and Measurement, Computer, Communication and Control, IMCCC 2014*, pages 569–572. IEEE, 9 2014.
- [82] J. Kennedy and R. Eberhart. Particle swarm optimization. In *Proceedings of ICNN'95 - International Conference on Neural Networks*, volume 4, pages 1942–1948. IEEE, 1995.

- [83] Anthony E. Lang and Andres M. Lozano. Parkinson's Disease. *New England Journal of Medicine*, 339, 10 1998.
- [84] A Ashburn, E Stack, R M Pickering, and C D Ward. A community-dwelling sample of people with Parkinson's disease: characteristics of fallers and non-fallers. *Age and ageing*, 30(1):47–52, 1 2001.
- [85] Lonneke M L de Lau and Monique M B Breteler. Epidemiology of Parkinson's disease. *The Lancet. Neurology*, 5(6):525–35, 6 2006.
- [86] Dominique Twelves, Kate S.M. Perkins, and Carl Counsell. Systematic review of incidence studies of Parkinson's disease. *Movement Disorders*, 18(1):19–31, 1 2003.
- [87] Stephen K Van Den Eeden, Caroline M Tanner, Allan L Bernstein, Robin D Fross, Amethyst Leimpeter, Daniel A Bloch, and Lorene M Nelson. Incidence of Parkinson's disease: variation by age, gender, and race/ethnicity. *American journal of epidemiology*, 157(11):1015–22, 6 2003.
- [88] M Baldereschi, A Di Carlo, W A Rocca, P Vanni, S Maggi, E Perissinotto, F Grigoletto, L Amaducci, and D Inzitari. Parkinson's disease and parkinsonism in a longitudinal study: two-fold higher incidence in men. ILSA Working Group. Italian Longitudinal Study on Aging. *Neurology*, 55(9):1358–63, 11 2000.
- [89] C David Marsden, J D Parkes, and N. Quinn. Fluctuations of disability in Parkinson's disease—clinical aspects. In *Movement disorders*, pages 96–122. Butterworth-Heinemann, 1 1981.
- [90] Lazzaro Di Biase, John Stuart Brittain, Syed Ahmar Shah, David J. Pedrosa, Hayriye Cagnan, Alexandre Mathy, Chiung Chu Chen, Juan Francisco Martín-Rodríguez, Pablo Mir, Lars Timmerman, Petra Schwingenschuh, Kailash Bhatia, Vincenzo Di Lazzaro, and Peter Brown. Tremor stability index: A new tool for differential diagnosis in tremor syndromes. *Brain*, 140(7):1977–1986, 7 2017.
- [91] Giovanni Di Pino, Domenico Formica, Jean Marc Melgari, Fabrizio Taffoni, Gaetano Salomone, Lazzaro Di Biase, Ester Caimo, Fabrizio Vernieri, and Eugenio Guglielmelli. Neurophysiological bases of tremors and accelerometric parameters analysis. In *Proceedings of the IEEE RAS and EMBS International Conference on Biomedical Robotics and Biomechanics*, pages 1820–1825. IEEE, 6 2012.
- [92] S. Summa, J. Tosi, F. Taffoni, L. Di Biase, M. Marano, A. Cascio Rizzo, M. Tombini, G. Di Pino, and D. Formica. Assessing bradykinesia in Parkinson's disease using gyroscope signals. In *2017 International Conference on Rehabilitation Robotics (ICORR)*, pages 1556–1561, London, 7 2017. IEEE.
- [93] W R.G. Gibb and A J Lees. The relevance of the Lewy body to the pathogenesis of idiopathic Parkinson's disease, 6 1988.
- [94] G. Deuschl, P. Krack, M. Lauk, and J. Timmer. Clinical neurophysiology of tremor. *Journal of Clinical Neurophysiology*, 13(2):110–121, 3 1996.

- [95] J. A. De Marcaida. Evaluation of dyskinesias in a pilot, randomized, placebo-controlled trial of remacemide in advanced Parkinson disease. *Archives of Neurology*, 58(10):1660–1668, 10 2001.
- [96] Christopher G. Goetz, Stanley Fahn, Pablo Martinez-Martin, Werner Poewe, Cristina Sampaio, Glenn T. Stebbins, Matthew B. Stern, Barbara C. Tilley, Richard Dodel, Bruno Dubois, Robert Holloway, Joseph Jankovic, Jaime Kulisevsky, Anthony E. Lang, Andrew Lees, Sue Leurgans, Peter A. LeWitt, David Nyenhuis, C. Warren Olanow, Olivier Rascol, Anette Schrag, Jeanne A. Teresi, Jacobus J. Van Hilten, and Nancy LaPelle. Movement disorder society-sponsored revision of the unified Parkinson's disease rating scale (MDS-UPDRS): Process, format, and clinimetric testing plan. *Movement Disorders*, 22(1):41–47, 1 2007.
- [97] M. M. Hoehn and M. D. Yahr. Parkinsonism: Onset, progression, and mortality. *Neurology*, 50(2):318–318, 8 1998.
- [98] Giovanni Rizzo, Massimiliano Copetti, Simona Arcuti, Davide Martino, Andrea Fontana, and Giancarlo Logroscino. Accuracy of clinical diagnosis of Parkinson disease. *Neurology*, 86(6):566–576, 2 2016.
- [99] Yasushi Masuda, Mitsuyoshi Sekimoto, Masayuki Nambu, Yuji Higashi, Toshiro Fujimoto, Kunihiro Chihara, and Toshiyo Tamura. An unconstrained monitoring system for home rehabilitation. *IEEE Engineering in Medicine and Biology Magazine*, 24(4):43–47, 7 2005.
- [100] Bartosz P. Jarochoowski, Seung Jung Shin, Dae Hyun Ryu, and Hyung Jun Kim. Ubiquitous rehabilitation center: An implementation of a wireless sensor network based rehabilitation management system. In *2007 International Conference on Convergence Information Technology, ICCIT 2007*, pages 2349–2358. IEEE, 11 2007.
- [101] Sachin Bhardwaj, D.-S Lee, S C Mukhopadhyay, and Wan-Young Chung. Ubiquitous Healthcare Data Analysis and Monitoring Using Multiple Wireless Sensors for Elderly Person. *Sensors & Transducers*, 90:87–99, 2008.
- [102] J B Saunders and V T Inman. The Major Determinants in Normal and Pathologic Gait. *The Journal of Bone & Joint Surgery*, 35(3):543–558, 1953.
- [103] Joseph Ghika, Allen W. Wiegner, Jian Jun Fang, Llewelyn Davies, Robert R. Young, and John H. Growdon. Portable System for Quantifying Motor Abnormalities in Parkinson's Disease. *IEEE Transactions on Biomedical Engineering*, 40(3):276–283, 3 1993.
- [104] Paolo Bonato. Advances in wearable technology and applications in physical medicine and rehabilitation. *Journal of neuroengineering and rehabilitation*, 2(1):2, 2 2005.
- [105] Houde Dai, Bernward Otten, Jan Hinnerk Mehrkens, Lorenzo T. D'Angelo, and Tim C. Lueth. A novel glove monitoring system used to quantify neurological symptoms during deep-brain stimulation surgery. *IEEE Sensors Journal*, 13(9):3193–3202, 9 2013.

- [106] Dustin A. Heldman, Joseph P. Giuffrida, Robert Chen, Megan Payne, Filomena Mazzella, Andrew P. Duker, Alok Sahay, Sang Jin Kim, Fredy J. Revilla, and Alberto J. Espay. The modified bradykinesia rating scale for Parkinson's disease: Reliability and comparison with kinematic measures. *Movement Disorders*, 26(10):1859–1863, 8 2011.
- [107] Shyamal Patel, Konrad Lorincz, Richard Hughes, Nancy Huggins, John Growdon, David Standaert, Metin Akay, Jennifer Dy, Matt Welsh, and Paolo Bonato. Monitoring motor fluctuations in patients with parkinsons disease using wearable sensors. *IEEE Transactions on Information Technology in Biomedicine*, 13(6):864–873, 11 2009.
- [108] Ji Won Kim, Jae Ho Lee, Yuri Kwon, Chul Seung Kim, Gwang Moon Eom, Seong Beom Koh, Do Young Kwon, and Kun Woo Park. Quantification of bradykinesia during clinical finger taps using a gyrosensor in patients with Parkinson's disease. *Medical and Biological Engineering and Computing*, 49(3):365–371, 3 2011.
- [109] R. C. Oldfield. The assessment and analysis of handedness: The Edinburgh inventory. *Neuropsychologia*, 9(1):97–113, 3 1971.
- [110] Sivakumar Balasubramanian, Alejandro Melendez-Calderon, and Etienne Burdet. A robust and sensitive metric for quantifying movement smoothness. *IEEE Transactions on Biomedical Engineering*, 59(8):2126–2136, 8 2012.
- [111] Sivakumar Balasubramanian, Alejandro Melendez-Calderon, Agnes Roby-Brami, and Etienne Burdet. On the analysis of movement smoothness. *Journal of NeuroEngineering and Rehabilitation*, 12(1):112, 12 2015.
- [112] Zofia Hanusz and Joanna Tarasińska. Normalization of the Kolmogorov–Smirnov and Shapiro–Wilk tests of normality. *Biometrical Letters*, 52(2), 2015.
- [113] Arash Salarian, Heike Russmann, François J G Vingerhoets, Pierre R. Burkhard, and Kamiar Aminian. Ambulatory monitoring of physical activities in patients with Parkinson's disease. *IEEE Transactions on Biomedical Engineering*, 54(12):2296–2299, 12 2007.
- [114] Sandra Richardson. The Timed “Up & Go”: A Test of Basic Functional Mobility for Frail Elderly Persons. *Journal of the American Geriatrics Society*, 39(2):142–148, 2 1991.
- [115] L Nyberg and Y Gustafson. Patient falls in stroke rehabilitation. A challenge to rehabilitation strategies. *Stroke*, 26(5):838–42, 5 1995.
- [116] Bijan Najafi, Kamiar Aminian, Francois Loew, Yves Blanc, and Philippe A. Robert. Measurement of stand-sit and sit-stand transitions using a miniature gyroscope and its application in fall risk evaluation in the elderly. *IEEE Transactions on Biomedical Engineering*, 49(8):843–851, 8 2002.
- [117] Carlo Massaroni, Cecilia Venanzi, Amanda P. Silvatti, Daniela Lo Presti, Paola Saccomandi, Domenico Formica, Francesco Giurazza, Michele A. Caponero, and Emiliano Schena. Smart textile for respiratory monitoring and thoraco-abdominal motion pattern evaluation. *Journal of Biophotonics*, 11(5):e201700263, 5 2018.

- [118] Carlo Massaroni, Paola Saccomandi, Domenico Formica, Daniela Lo Presti, Michele Arturo Caponero, Giulia Di Tomaso, Francesco Giurazza, Mario Muto, and Emiliano Schena. Design and Feasibility Assessment of a Magnetic Resonance-Compatible Smart Textile Based on Fiber Bragg Grating Sensors for Respiratory Monitoring. *IEEE Sensors Journal*, 16(22):8103–8110, 11 2016.
- [119] Daniela Lo Presti, Carlo Massaroni, Domenico Formica, Paola Saccomandi, Francesco Giurazza, Michele Arturo Caponero, and Emiliano Schena. Smart Textile Based on 12 Fiber Bragg Gratings Array for Vital Signs Monitoring. *IEEE Sensors Journal*, 17(18):6037–6043, 9 2017.
- [120] Marco Ciocchetti, Carlo Massaroni, Paola Saccomandi, Michele Caponero, Andrea Polimadei, Domenico Formica, Emiliano Schena, Marco Ciocchetti, Carlo Massaroni, Paola Saccomandi, Michele A. Caponero, Andrea Polimadei, Domenico Formica, and Emiliano Schena. Smart Textile Based on Fiber Bragg Grating Sensors for Respiratory Monitoring: Design and Preliminary Trials. *Biosensors*, 5(3):602–615, 9 2015.
- [121] Jacopo Tosi, Susanna Summa, Fabrizio Taffoni, Lazzaro di Biase, Massimo Marano, Angelo Cascio Rizzo, Mario Tombini, Emiliano Schena, Domenico Formica, Giovanni Di Pino, L Di Biase, Massimo Marano, Angelo Cascio Rizzo, Mario Tombini, Emiliano Schena, Domenico Formica, and G Di Pino. Feature Extraction in Sit-to-Stand Task Using M-IMU Sensors and Evaluatiton in Parkinson’s Disease. In *2018 IEEE International Symposium on Medical Measurements and Applications (MeMeA)*, pages 1–6. IEEE, 6 2018.
- [122] S E Daniel and A J Lees. Parkinson’s Disease Society Brain Bank, London: overview and research. *Journal of neural transmission. Supplementum*, 39:165–72, 1993.
- [123] S.G. Mallat. A theory for multiresolution signal decomposition: the wavelet representation. *IEEE Transactions on Pattern Analysis and Machine Intelligence*, 11(7):674–693, 7 1989.
- [124] Liu Chun-Lin. A tutorial of the wavelet transform. *NTUEE, Taiwan*, 2010.
- [125] Ingrid Daubechies. *Ten Lectures on Wavelets*. Springer-Verlag, 1992.
- [126] Luca Ricci, Domenico Formica, Laura Sparaci, Francesca Romana Lasorsa, Fabrizio Taffoni, Eleonora Tamilia, and Eugenio Guglielmelli. A new calibration methodology for thorax and upper limbs motion capture in children using magneto and inertial sensors. *Sensors (Switzerland)*, 14(1):1057–1072, 1 2014.
- [127] B. Najafi, K. Aminian, F. Loew, Y. Blanc, and Ph Robert. Falling risk evaluation in elderly using miniature gyroscope. In *1st Annual International IEEE-EMBS Special Topic Conference on Microtechnologies in Medicine and Biology - Proceedings*, pages 557–561. IEEE, 2000.
- [128] B. Najafi, K. Aminian, F. Loew, Y. Blanc, and Ph Robert. An ambulatory system for physical activity monitoring in elderly. In *1st Annual International IEEE-EMBS Special Topic Conference on Microtechnologies in Medicine and Biology - Proceedings*, pages 562–566. IEEE, 2000.

- [129] Arash Salarian, Fay B Horak, Cris Zampieri, Patricia Carlson-Kuhta, John G Nutt, and Kamiar Aminian. ITUG, a sensitive and reliable measure of mobility. *IEEE Transactions on Neural Systems and Rehabilitation Engineering*, 18(3):303–310, 6 2010.
- [130] Bijan Najafi, Kamiar Aminian, Anisoara Paraschiv-Ionescu, François Loew, Christophe J. Bula, and Philippe Robert. Ambulatory system for human motion analysis using a kinematic sensor: Monitoring of daily physical activity in the elderly. *IEEE Transactions on Biomedical Engineering*, 50(6):711–723, 6 2003.
- [131] P. H. Veltink, H. B.J. Bussmann, W. De Vries, W. L.J. Martens, and R. C. Van Lummel. Detection of static and dynamic activities using uniaxial accelerometers. *IEEE Transactions on Rehabilitation Engineering*, 4(4):375–385, 1996.
- [132] Pamela J. Millington, Barbara M. Myklebust, and Georgia M. Shambes. Biomechanical analysis of the sit-to-stand motion in elderly persons. *Archives of physical medicine and rehabilitation*, 73(7):609–17, 7 1992.
- [133] Wim G M Janssen, Hans B J Bussmann, and Henk J Stam. Determinants of the sit-to-stand movement: a review. *Physical therapy*, 82(9):866–79, 9 2002.
- [134] Bruno Siciliano, Lorenzo Sciavicco, Luigi Villani, and Giuseppe Orolò. *Robotics - Modelling, Planning and Control*. Springer, 2009.
- [135] Bruno Siciliano and Oussama Khatib. *Springer handbook of robotics*. Springer, 2016.
- [136] Jack B. Kuipers. *Quaternions and rotation sequences : a primer with applications to orbits, aerospace, and virtual reality*. Princeton University Press, 1999.
- [137] William Rowan Hamilton. On quaternions; or on a new system of imaginaries in algebra. *The London, Edinburgh, and Dublin Philosophical Magazine and Journal of Science*, 25(163):10–13, 7 1844.
- [138] J. Willard Gibbs and Edwin Bidwell Wilson. *Vector analysis*. University Press, 1901.
- [139] J. M. McCarthy and J. M. *An introduction to theoretical kinematics*. MIT Press, 1990.
- [140] Thomas R. Kurfess. *Robotics and automation handbook*. CRC Press, 2005.
- [141] Richard M Murray. *A mathematical introduction to robotic manipulation*. CRC press, 2017.
- [142] Adolf Karger and Josef Novák. *Space kinematics and Lie groups*. Gordon and Breach Science Publishers, New York, New York, USA, 1985.